

UNIVERSIDADE FEDERAL DE SÃO CARLOS

Centro de Ciências Exatas e de Tecnologia

Programa de pós-graduação em Física

**Electronic and Optical Properties of Quasi-2D  
Nanostructures and Exfoliated Systems**

Diana Mercedes Meneses Gustin

---

Thesis presented to the Academic Faculty at Universidade Federal de São Carlos in partial fulfillment of the requirements for the Doctoral Degree in the Graduation Physics Course

---

Advisor: Prof. Dr. Victor Lopez Richard

São Carlos

30 de Outubro de 2017



Meneses Gustin, Diana Mercedes

Electronic and Optical Properties of Quasi-2D Nanostructures and Exfoliated Systems / Diana Mercedes Meneses Gustin. -- 2017.  
127 f. : 30 cm.

Tese (doutorado)-Universidade Federal de São Carlos, campus São Carlos,  
São Carlos

Orientador: Victor Lopez Richard

Banca examinadora: Guo-Qiang Hai, Marcos Roberto da Silva Tavares,  
Marcio Peron Franco de Godoy, Gilmar Eugeio Marques

Bibliografia

1. Método k.p em Sistemas Bidimensionais . 2. Interação Elétron-Fonon.  
3. Espalhamento em Duas Dimensões. I. Orientador. II. Universidade Federal  
de São Carlos. III. Título.

Ficha catalográfica elaborada pelo Programa de Geração Automática da Secretaria Geral de Informática (SIn).

DADOS FORNECIDOS PELO(A) AUTOR(A)







UNIVERSIDADE FEDERAL DE SÃO CARLOS


Centro de Ciências Exatas e de Tecnologia  
Programa de Pós-Graduação em Física

---

Folha de Aprovação

---

Assinaturas dos membros da comissão examinadora que avaliou e aprovou a Defesa de Tese de Doutorado da candidata Diana Mercedes Meneses Gustin, realizada em 30/10/2017:




---

Prof. Dr. Victor Lopez Richard  
UFSCar



---

Prof. Dr. Guo-Qiang Hai  
USP



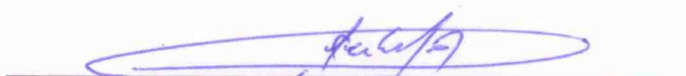
---

Prof. Dr. Marcos Roberto da Silva Tavarés  
UFABC



---

Prof. Dr. Marcio Peron Franco de Godoy  
UFSCar



---

Prof. Dr. Gilmar Eugenio Marques  
UFSCar



*To my mom*



# Acknowledgments

The PhD Thesis presented here is the result of four years of learning in many fields, and certainly it would be different without the contribution and support of many people, friends and relatives. My sincere thanks to all of them who contributed to the success of this work.

First of all, I would like to thank Professor Dr. Victor López Richard for his supervision and for always providing me assistance, guidance and carefully balancing every step of this research. From him I have learned not only about condensed matter physics and nanoscale systems, but also the enthusiasm and curiosity that define someone who really enjoys the work. With him I shaped my notion of ideal scientific work.

This thesis also rely on the valuable contribution of professor Dr. Sergio Ulloa who has been patient in guiding me during my stay at Ohio University. His teachings have profoundly marked my academic vision. I also thank all the students in Professor Sergio's research group at OU for welcoming me with great cordiality and making the work environment a comfortable space. With special thanks to Nancy Sandler.

I would like to thank my committee members Professor Dr. Marcos Tavares, Hai Guoqiang, Marcio Peron de Godoy and Gilmar Marques for their interest in my work, your dedication is greatly appreciated.

Among many people I had the pleasure of meeting at UFSCar, I thank to all members (old and new) of the Semiconductor Nanostructures group for the lessons and knowledge transmitted through healthy debates. Special thanks to my friend Luís A. Cabral, our coffee breaks were not only to pause the work, but necessary to restart the calculations with reloaded strengths.

In particular, I thank my UFABC and UFSCar friends for their unconditional support. Andrés, Indira, Carlos, Julián, Melissa and Marcela always encourage me to do my best

throughout this journey in Brazil. Each one of them in their own unique way is my example. I admire them greatly and I am going to have eternal gratitude and love for them. With all of them my stay, in these unknown lands, has been the most fabulous possible since 2011. Their friendship is more worth than I can express on paper and definitely the world seems better with all of you guys being part of my family.

I thank the solid team for many moments of fun, relax, reflections and hugs. Andrea and Gina have always been here as my close friends. Their companionship maintains my good humor and their encouragement words in countless times have always made me stronger and more confident, with you *solidas* I am in continuous growth. The *jaula* has been part of my history, according to each one of your visions, and I am going to be forever grateful for having you girls.

I also would like to thank my roommate Aurenice, because her life history, faith in the future and convictions have inspired me along this time here, we definitely make a good team.

I am extremely fortunate to count on Max Pinheiro Júnior, who brightened up my days. Tough times become easier with his jokes and his positive outlook when things are not in favor. But words will never do justice for all he gives me in these times, his exceptional dedication has been my constant reminder that I could do better than I think I would; and his charming coherence is always an invitation for sharing a good coffee, a good beer, or a good wine.

With my family I am deeply indebted for their unconditional support at any time and level. Without them this work would be impossible. A big thank to my mother for not just believing, but knowing that I could do this! You are the one who let me finish this cycle, this thesis is for you mom.

Last but not least, I thank the São Paulo Research Foundation, FAPESP, for financial support through the 2013/24253-5 and 2016/02065-0 projects.

Diana Mercedes Meneses Gustin

# Resumo

Esta Tese visa estudar, segundo uma abordagem teórica, as propriedades eletrônicas e ópticas de sistemas quânticos semicondutores quasi-2D. Usando como base o modelo  $\mathbf{k} \cdot \mathbf{p}$  obtivemos um conjunto satisfatório de resultados que explicam certos processos ópticos, descritos a seguir, de sistemas confinados em nanoescala tais como poços quânticos ou monocamadas de átomos. A necessidade e a implementação sistemática de novos e mais elevados níveis de aproximação aos modelos de estrutura eletrônica originais também são temas amplamente descritos.

Uma das primeiras contribuições deste estudo foi a verificação da necessidade de uma nova abordagem para descrever as interações de portador-fonon em poços quânticos baseados em GaAs além da teoria de potencial de deformação. Assim, a interação de Fröhlich foi considerada em nosso modelo, revelando a existência de acoplamentos assistidos por fônons entre diferentes estados na banda de valência e de condução, o que por sua vez resultou em mudanças significativas na estrutura eletrônica. Os resultados desta abordagem, assim como as simulações e previsões de resultados, permitiram explicar dois efeitos intrigantes: (i) a potencial observação de magneto-polarons de buracos pesados-leves, (ii) a relevância dos estados 2D como intermediários nos processos de relaxação, auxiliado por fônons, a partir de uma estrutura 3D para uma 0D.

Outro sistema estudado foi o dissulfeto de molibdênio ( $MoS_2$ ) bidimensional, no qual o espalhamento de elétrons dependia de perturbações induzidas localmente no material. Uma versão do Hamiltoniano de Dirac para partículas com massa foi usado. Os processos de espalhamento foram descritos em termos do *phase shift* e das correspondentes seções transversais. Comparando os resultados deste modelo com aqueles obtidos usando uma relação de dispersão parabólica com uma apropriada massa efetiva foi possível obter informações interessantes com respeito à condutividade de ambas

formulações eletrônicas. Os regimes assintóticos de cada um dos modelos foi também estudado, sendo que para baixas energias, onde ambas dispersões coincidem em bandas parabólicas, o processo de espalhamento é dominado por canais com baixo momento angular e ainda resultam em amplitudes de dispersão quase comparáveis. Por outro lado, a seção transversal diferencial para o caso de altas energias possui a clara assinatura das duas relações de dispersão. A compreensão da dinâmica eletrônica nestes sistemas é promissora para um design racional de estruturas com funcionalidades desejadas, como exemplificamos apresentando seções transversais diferenciais para diferentes tipos de centros de espalhamento.



# Abstract

This thesis is aiming to study, according to various theoretical approaches, the electronic and optical properties of quasi-2D semiconductor quantum systems. Using the  $\mathbf{k} \cdot \mathbf{p}$  model as a basis, we obtained a satisfactory set of results that explain certain optical processes, described below, of nanoscale confined systems, such as quantum wells or monolayers of atoms. The need and the systematic implementation of new and higher levels of approximation from the original electronic structure models also are themes broadly described here.

One of the first contributions of this study was the verification of the necessity of a new approach to describe the phonon-carrier interactions in GaAs-based quantum wells, beyond the deformation potential theory. Thus, the Fröhlich interaction was considered in our model, revealing the existence of phonon assisted couplings between different states in the valence and conduction band, which resulted in significant changes in the electronic structure. The results of this approach, as well as the simulations and new predictions allowed us to explain two intriguing effects: (i) the potential observation of magneto-polarons of light-heavy holes, (ii) the relevance of 2D states as intermediaries in relaxation processes, assisted by phonons, from a 3D structure to a 0D.

Another system studied was the two-dimensional molybdenum disulphide ( $\text{MoS}_2$ ), in which the carrier scattering depends on a perturbation locally induced in the material. One version of the Dirac Hamiltonian for massive particles was used. The scattering processes have been described in terms of the phase shift and the corresponding cross sections. By comparing the results of this model with those obtained using a parabolic dispersion relation with an appropriate effective mass, it was possible to obtain interesting information regarding the conductivity of both electronic models. The asymptotic regimes of each of the models were also studied, and for low energies, where

both dispersions coincide as parabolic bands, the scattering process is dominated by channels with low angular momentum and still results in almost comparable dispersion amplitudes. On the other hand, the differential cross section in the high energy regime has the clear signature of the two scattering relations. The understanding of the electronic dynamics in these systems is promising for the design of structures with desired functionalities, as exemplified by presenting the differential cross sections for different types of scattering centers.

# Contents

<b>1</b>	<b>Introduction</b>	<b>17</b>
<b>2</b>	<b>Electronic Structure and Phonons Effects in Quantum Wells</b>	<b>23</b>
2.1	<b><math>\mathbf{k} \cdot \mathbf{p}</math> Model</b> . . . . .	24
2.2	Electronic Structure of Quantum Wells . . . . .	27
2.2.1	Quantum Well Conduction and Valence Band Calculations . . . . .	31
2.3	Carrier-Phonon Interaction . . . . .	33
<b>3</b>	<b>Spin-Resolved Photo-Generation Filtering Induced by Phonon</b>	<b>47</b>
3.1	Theoretical Simulation . . . . .	53
3.2	Magneto Absorption . . . . .	55
3.3	Spin Decoherence . . . . .	63
<b>4</b>	<b>Electron Dynamics in 2D Semiconductors Layers</b>	<b>67</b>
4.1	Scattering Theory in Two Dimensions . . . . .	69
4.2	Scattering Phase Shift . . . . .	72
4.2.1	Dirac Case . . . . .	72
4.2.2	Parabolic Approximation: Schrödinger Case . . . . .	76
4.3	Probability Density and Differential Cross Section . . . . .	80
4.4	Asymptotic Analysis . . . . .	86
4.4.1	Dirac Formulation . . . . .	86
4.4.2	Schrödinger Formulation . . . . .	89
<b>5</b>	<b>Conclusions and Final Considerations</b>	<b>93</b>

## Appendices

<b>A</b>	<b>Matrix Representation of the Luttinger Hamiltonian</b>	<b>99</b>
<b>B</b>	<b>Rotation of Luttinger Hamiltonian for Zincblende Crystal</b>	<b>103</b>
<b>C</b>	<b>Scattering Systems</b>	<b>105</b>
C.1	Dirac Dynamic . . . . .	105
C.1.1	Schrödinger Dynamics . . . . .	108
C.2	Asymptotic Analysis . . . . .	111
C.2.1	Dirac Formulation . . . . .	111
C.2.2	Schrödinger Formulation . . . . .	115

# Chapter 1

## Introduction

The attractiveness of the nanoscaled physical systems comes from the ability to increase the functionality and performance of the next generation of devices, substituting in this way the classical microelectronics. Due to the fact that the dimensions of these nanostructures are comparable to the de Broglie wavelength of the electron, their electrical, optical and mechanical properties are described by quantum mechanics. Here, we will take advantage of some quantum phenomena in order to describe and tune the carriers behavior in two dimensional systems.

Among a variety of materials used for growing nanostructures, special attention has been directed to the heterostructures formed by semiconductor compounds, even over metal or dielectric substrates. This remains as an important topic for technology and industry, specially due to the switching capability of diodes, photovoltaic cells, transistors, detectors and thermistors. Typical semiconductor structures are composed of alloys of the IV group elements and/or III-V and II-VI compounds. A prolific use have the GaAs and InAs based structures, particularly during the last few decades [1–4], in part due to the relatively easy fabrication and the capacity to confine electrons and holes when they are combined with other semiconductors, yielding to the emergence of nanostructures such as GaAlAs/GaAs or InGaAs/GaAs.

There are several fabrication techniques employed to obtain semiconductor nanostructures of high quality such as molecular beam epitaxy (MBE), chemical beam epitaxy (CBE) and metal-organic chemical vapor deposition (MOCVD) [5, 6]. The choice for the crystal growth as well as its design is related with the number of directions along

which the carriers could be confined [7]. Structures where carriers are confined in the three spacial directions are called quantum dots [8]. In turn, in quantum wires, the electrons and holes are confined in two spatial directions [9, 10]. While, in quantum wells the charge carriers are confined just in one direction whereas their movement is free along the other two [11, 12].

Another way developed to exploit the quantum phenomena from the size quantization is inspired in the conventional exfoliation techniques similar to the ones used for graphene synthesis [13]. By scaling down the transition metal dichalcogenide bulk until a monolayer, carriers are restricted to move into a two dimensional lattice. This exfoliation is possible due to the weak bonds between the staked layers. As well as the graphite case, the transition metal dichalcogenides have their layers weakly bound by van der Waals forces allowing to a repetitive cleavage of the bulk until the single-layer form.

This thesis presents a sequence of novel results derived from a systematic investigation of the hybridization states and scattering effects, evidenced on the optical response as well as in the transport and electronic properties of quasi-bi-dimensional (2D) semiconductor systems such as quantum wells and monolayer systems. The study was developed in collaboration with experimental groups of growth and spectroscopy (GNS-UFSCar; Micro-electronics Institute of Madrid - Spain and in the Center for Nanotechnology and Nanomaterials, Technical University Munich - Germany) that enrich the research scope and promote the potential unfolding of the theoretical challenges.

Three basic lines of work will be covered here: (i) the theoretical analysis of hybrid states in the electronic structure of quantum wells modulated by the concentration of In under magnetic fields and the simulation of the electron and hole-phonon coupling effects; (ii) the analysis of the phonon-assisted spin relaxation from 3D towards quantum dots through 2D wetting layers; and (iii) the study of electron scattering process occurring in a single-layer of molybdenum disulphide ( $\text{MoS}_2$ ) modulated by local perturbations. The proposed problems paved a way based on the  $\mathbf{k} \cdot \mathbf{p}$  method for a systematic application of theoretical tools for characterizing the electronic structure of different materials beyond those studied here. Also, all these topics have allowed us tackling and using theoretical tools which are fundamental for the development of studies in several areas related to the condensed matter physics and their link with the

simulation and prediction of experimental results of the collaborations in progress. Experimental evidences provided by our collaborators pointed to unexpected features of the optical properties in 2D semiconductor nanostructures obtained through epitaxial growth techniques that attracted our attention due to the possibility of energy spectrum modulation by a carrier-phonon dynamics. Therefore, we devote special attention to the lattice vibration phenomena. The quantum of lattice oscillations, called phonons, are related to the coupling of electrons, or holes, with the electric polarization or electronic potential deformation produced by them in a given structure. Those phonons are elementary excitations that can be classified according to their polarization and their energy dispersion. We shall focus on the longitudinal-optical (LO) phonons only, and we show that carrier-phonon interaction can strongly influence the optical, transport, and energy relaxation properties of most heterostructures.

In all these cases, we assume that the structures are built on combinations of semiconductor compounds: GaAs/Al<sub>x</sub>Ga<sub>1-x</sub>As and Ga<sub>x</sub>In<sub>1-x</sub>As. In this kind of polar semiconductor systems, a charge carrier moving slowly in the crystal may cause a distortion of the lattice. The distortion creates a polarization field which acts back on the electron or hole and can be reflected, for instance, as an enhancement of its effective mass [14]. This effect is interpreted as a polarization cloud that accompanies the charge through the lattice. The carrier together with the polarization cloud is called polaron and under resonant conditions, when the energy difference between two neighboring states is about one LO-phonon energy, the polaron effects are enhanced and can be tuned with magnetic fields [15].

While the electron-phonon coupling effects, i. e. polaron effects, in the conduction band have been deeply studied [16,17], they have usually been neglected in the valence band [18]. In this thesis, we characterize the polaron induced hybridization, which is tunable by means of external magnetic field and geometrical parameters such as the growth direction. Concomitantly, we contrasted various perturbative techniques to elucidate the carrier-phonon coupling effects including also the full diagonalization in the  $\mathbf{k} \cdot \mathbf{p}$  model. The relevance of polaron and phonon emission effects will be also discussed on the basis of available experimental data proved experimentally. Two main problems were addressed concerning to the phonon interaction: (i) the possible existence of quasi-particle states in the valence band arising from the coupling between

the phonons and the 2D heavy-light hole Landau levels and (ii) the demonstration of resonant phonon intermediation occurring in the carrier relaxation process from a 3D system towards quantum dots via a 2D confined states.

Regarding exfoliated systems, special interest has been directed to transition metal dichalcogenides, TMDs. These materials can be scaled down until 2D monolayers, where drastic changes in the band structure are found [19]. For example, the band structure of TMDs in the bulk phase usually has an indirect energy gap, whereas in the monolayer structure a direct gap appears. The mechanical, optical and electronic properties of the group of TMDs such as flexibility, semiconductivity, and charge density waves have been attracting the interest for the development of new materials for decades, as well as in the field of solar cells and photocatalysis more recently [20–22]. These materials are arranged in an X-M-X structure, where  $M$  is a transition metal as  $Mo, W, etc$ , and  $X = S, Se, Te$ . While atoms of the same layer are tightly bonded, the interlayer interactions take place through van der Waals forces which allow detaching each layer by means of exfoliation techniques as those used for obtaining graphene sheets [13]. In addition to the glimpsed technological applications, the study of  $MoS_2$  reveals itself as an inexhaustible source of interesting and fundamental physical problems whose solutions enrich the knowledge of new quantum properties of condensed matter.

In these 2D crystals, the creation of local perturbations opens a way to modify not only their electronic structure but also to control the transport response for instance by external means [23]. Here, in order to describe the effect of this kind of interactions, we solve the scattering problem using a massive Dirac formulation and describe the transport as well as its modulation by the differential scattering cross sections. Moreover, we compare these results with the appropriated parabolic relation dispersion at low energies regime. From these results we clearly identify two signatures, each one with a distinct anisotropic behavior and energy dependence in the Dirac or Schrödinger formulation.

This thesis is organized as follows. In chapter 2, a brief description of  $\mathbf{k} \cdot \mathbf{p}$  model is presented in conjunction with the results obtained from this formalism for InGaAs-based quantum wells. The results obtained for the phonon-carrier interactions and the theoretical model used for these calculations is also present in chapter 2. The subse-



quent chapter is devoted to the discussion of spin resolved photo-generation filtering through wetting layers. In the following chapter 4, the scattering theory is discussed in conjunction with the phase shift method used to find the differential cross section in two dimensions. A comparison between the massive Dirac and Schrödinger relation dispersion is performed using also the differential cross section theory.



## Chapter 2

# Backgrounds for Electronic Structure and Phonons Effects in Quantum Wells

Quantum wells are the kind of nanostructures with reduced dimension in which the carrier motion is quantized through subbands. It is well known that either bands and subbands can be tuned by external means such as strain, electric or magnetic fields. With the application of a magnetic field, for instance, an additional quantum confinement arises and consequently a new quantum number. Another way to manipulate their response is by changing the internal parameters such as the effective mass that depends on the system geometry [24]. While several studies have analyzed the effects of the magnetic field on the conduction band for different quantum wells systems [25–29], only a few ones have attempted to develop a systematic investigation of the behavior of valence subbands when phonon interaction is taken into account [30–32].

In figure Figure 2.1 a schematic representation of a quantum well is shown, the growth direction is taken as  $z$ , along which the carriers can only occupy the quantized states  $m$  whereas in  $(x, y)$  plane the carriers are free to move. However, when a magnetic field  $\mathbf{B}$  is applied along  $z$ , the carriers should occupy states with discrete energy values in the  $(x, y)$  plane, called Landau levels and labeled by  $N$  in Figure 2.1. When a magnetic field is applied to an optical experiment, additional information of the electronic structure can be assessed once  $\mathbf{B}$  affects mainly the electrons and holes rather than the lattice [33].

Moreover, in 2D systems, the consequences of the charge carrier interaction with the oscillations of the host lattice are relevant and, as presented in this thesis, it can be tuned by electronic confinement and growth direction.

Thus, in order to theoretically emulate these properties we should first introduce the basic theoretical grounds and concepts on which the models were built. One of them is the Born - Oppenheimer approximation that allows to assume that the nuclear and electronic motions in the crystal lattice can be treated separately. Hence, the electronic problem can be solved first within an ideal lattice, and then the interaction with nuclei oscillations is considered afterward as a perturbation. Thus, the first step is the characterization of the energy spectrum in a single electron model.

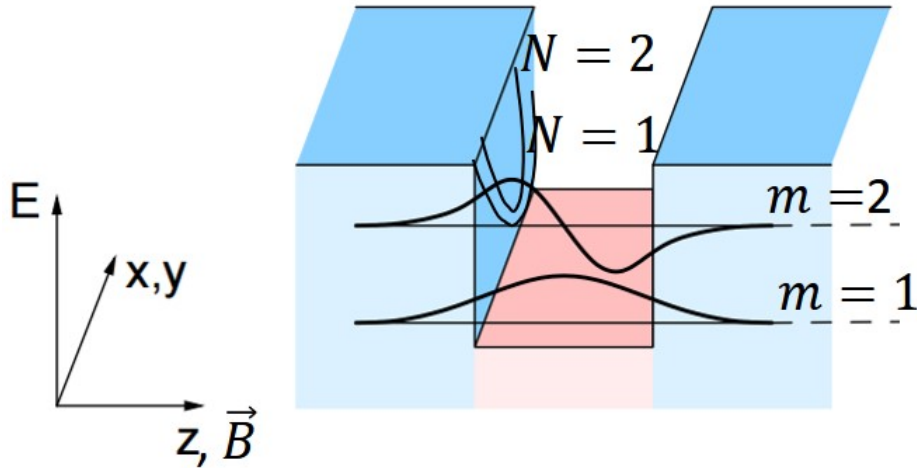


**Figure 2.1:** Schematic representation of a quantum well. The quantized states due to spatial confinement and magnetic field are labeled by  $m$  and  $N$  respectively. Both  $m$  and  $N$  goes from 1 until  $\infty$ .

## 2.1 $\mathbf{k} \cdot \mathbf{p}$ Model

The main idea behind  $\mathbf{k} \cdot \mathbf{p}$  method is to include the effects of the interaction between the charge carrier and the periodic potential of the crystal lattice in the carrier mass. This approximation is known as effective mass [34]. The method is a powerful and flexible approach for the investigation of the band structure near symmetry points of the Brillouin zone of many semiconductors [35]. Also, it is used to determine analytically

the eigenvalues and eigenfunctions by obtaining expressions for the dispersion relation. Another advantage of this method is the relative ease for the incorporation of strain effects on the band structure and external electric and magnetic fields. Special interest is directed to the reciprocal lattice center of semiconductors with zinc-blende type symmetry, which is called  $\Gamma$ -point [36] which is usually well described by the  $\mathbf{k} \cdot \mathbf{p}$  model. States responsible for the optical recombination process are located close to this point ( $\mathbf{k} = 0$ ) in a considerable amount of direct band-gap semiconductors [24]. By modelling a charge carrier subjected to the periodic potential of a crystal lattice as a free particle with a specific mass  $m_e$ , we enormously simplify the band structure calculation, since  $m_e$  influences measurable properties of a crystal. However, the value of  $m_e$  depends on some factors, which are essentially isotropic and anisotropic parameters. Here we discuss both cases: the parabolic approximation, which describes very well the conduction band, and the Luttinger model, used to describe the valence band. At first, the fundamentals of  $\mathbf{k} \cdot \mathbf{p}$  model are presented followed by the derivation of the effective mass. Briefly, the spin-orbit interactions will be described; then we will include the effects of the spatial confinement and the parabolic relation dispersion for the conduction band will be obtained. The effects of applying a magnetic field are discussed and included into the Hamiltonian matrix for the valence band.

Firstly, we transform a crystal Hamiltonian to the  $\mathbf{k} \cdot \mathbf{p}$  representation starting from the following Schrödinger Hamiltonian

$$H\Psi = \left( \frac{p^2}{2m_0} + V(r) \right) \Psi = E\Psi. \quad (2.1)$$

Due to the crystal potential periodicity, the Bloch theorem can be used. Then, a particular state  $\Psi$  occupying an energy band  $n$  with a wave vector  $k$  is represented by

$$\Psi_{nk} = e^{i\mathbf{k} \cdot \mathbf{r}} u_{nk}(r), \quad (2.2)$$

using this, the equation (2.1) becomes

$$\left( \frac{-\hbar^2}{2m_0} + V \right) u_{nk} + \frac{\hbar^2 k^2}{2m_0} u_{nk} + \frac{\hbar}{m_0} \mathbf{k} \cdot \mathbf{p} u_{nk} = E_{nk} u_{nk}. \quad (2.3)$$

We choose a complete orthonormal basis  $\{u_{n'k_0}\}$  such that

$$H u_{n'k_0} = \left( \frac{-\hbar^2}{2m_0} + V \right) u_{n'k_0} + \frac{\hbar^2 k_0^2}{2m_0} u_{n'k_0} + \frac{\hbar}{m_0} \mathbf{k}_0 \cdot \mathbf{p} u_{n'k_0} \quad (2.4)$$

$$= E_{n'k_0} u_{n'k_0}, \quad (2.5)$$

and the state  $u_{nk}$  could be expanded by

$$u_{n,k} = \sum_{n'} C_{n,n'} u_{n'k_0}. \quad (2.6)$$

Inserting expression (2.6) into (2.3) and multiplying by the complex conjugate  $u_{n'k_0}^*$  we have

$$\sum_{n'} \left( \left( E_{nk_0} - E_{nk} + \frac{\hbar^2}{2m_0} (k^2 - k_0^2) \right) \delta_{nn'} + \frac{\hbar}{m} \langle u_{n'k_0} | (\mathbf{k} - \mathbf{k}_0) \cdot \mathbf{p} | u_{n,k_0} \rangle \right) C_{nn'} = 0, \quad (2.7)$$

or, isolating  $E_{nk}$

$$E_{nk} = \left( E_{nk_0} + \frac{\hbar^2}{2m_0} (k^2 - k_0^2) \right) + \sum_{n'} C_{nn'} \left( \frac{\hbar}{m} \langle u_{n'k_0} | (\mathbf{k} - \mathbf{k}_0) \cdot \mathbf{p} | u_{n,k_0} \rangle \right). \quad (2.8)$$

We are interested only in electrons or holes near  $k_0 = 0 \equiv \Gamma$  (which is the high symmetry point), therefore we expand in Taylor series the dispersion relation around zero until second order of  $k$ . Since we are looking for the band edges, the first correction is null, and the energy takes the following form

$$E_{nk} = E_{n,0} + \frac{\hbar^2}{2m_0} k^2 + \sum_{n' \neq n} \frac{\hbar^2}{m_0^2} \frac{|\langle u_{n',0} | \mathbf{k} \cdot \mathbf{p} | u_{n,0} \rangle|^2}{E_{n',0} - E_{n,0}}. \quad (2.9)$$

or

$$E_{nk} = E_{n,0} + \frac{\hbar^2}{2} \sum_{i,j} \frac{k_i k_j}{m_{ij}} \quad (2.10)$$

where  $i, j = x, y, z$  and

$$\frac{1}{m_{ij}} = \frac{\delta_{ij}}{m_0} + \sum_{n' \neq n} \frac{2}{m_0^2} \frac{\langle u_{n',0} | p_i | u_{n,0} \rangle \langle u_{n',0} | p_j | u_{n,0} \rangle}{E_{n',0} - E_{n,0}}. \quad (2.11)$$

The inverse of (2.11),  $m_{ij}$ , is the effective mass tensor. In other words, using the effective mass concept we are inserting the effects of the lattice crystal within the mass and allowing us to treat the charge carriers as free particles.

Until now, just the kinetic and potential terms were taken into account in the formulation presented here. However, the insertion of spin-orbit interaction,  $H_{SO}$  [37], can be easily made by including the following term

$$H_{SO} = -\frac{\hbar}{4m_0^2 c^2} \boldsymbol{\sigma} \cdot \mathbf{p} \times \nabla V(\mathbf{r}), \quad (2.12)$$

where  $c$  is the speed of light,  $\nabla V(\mathbf{r})$ , the gradient of the crystalline potential and,  $\boldsymbol{\sigma}$ , is the vector of Pauli spin matrices.

Thus, after applying the expression (2.2) into (2.12), we have

$$H_{SO}\Psi_{nk} = \frac{\hbar}{4m_0^2c^2}\boldsymbol{\sigma} \times \nabla V(\mathbf{r}) \cdot \mathbf{p}e^{i\mathbf{k}\cdot\mathbf{r}}u_{nk}(r) \quad (2.13)$$

$$= \frac{\hbar}{4m_0^2c^2}\boldsymbol{\sigma} \times \nabla V(\mathbf{r}) \cdot e^{i\mathbf{k}\cdot\mathbf{r}}(-\hbar\mathbf{k} + i\hbar\nabla)u_{nk}(r). \quad (2.14)$$

Including the spin-orbit interactions  $H_{SO}$  besides the kinetic and potential terms, the Hamiltonian has the form

$$H = H_0 + H_1 \quad (2.15)$$

where

$$H_0 = \frac{-\hbar^2}{2m_0} + V - \frac{\hbar}{4m_0^2c^2}\boldsymbol{\sigma} \cdot \nabla V(\mathbf{r}) \quad (2.16)$$

$$H_1 = \frac{\hbar^2k^2}{2m_0} + \frac{\hbar}{m_0}\mathbf{k} \cdot \boldsymbol{\pi} \quad (2.17)$$

and

$$\boldsymbol{\pi} = \mathbf{p} + \frac{\hbar}{4m_0c^2}\nabla V(\mathbf{r}) \times \boldsymbol{\sigma}. \quad (2.18)$$

By following a procedure analogous to the one adopted for deriving equation (2.7), the spin-orbit effects are included into the eigenvalue matrix and therefore into the description of the band structure.

## 2.2 Electronic Structure of Quantum Wells

To use the  $\mathbf{k} \cdot \mathbf{p}$  model in a practical way, some approximations still should be introduced. We are interested only in studying the electronic and optically active states and, in general, just a reduced set of bands is strongly coupled at the  $\Gamma$  point, and therefore the matrix dimension can be reduced.

For the conduction band, we adopted the parabolic approximation with isotropic effective mass near the center of the Brillouin zone ( $\mathbf{k} = 0$ ),

$$E(\mathbf{k}) = E_g + \frac{\hbar^2k^2}{2m_e}, \quad (2.19)$$

where  $E_g$  is the energy gap,  $m_e$  the effective mass and,  $\mathbf{k}$ , the wave vector from the Brillouin zone center. The value of  $m_e$  is found experimentally or by first principles calculations. This assumption is reasonable for semiconductors with large band gap as GaAs, once the distance between electrons and holes bands is large enough to allow neglecting their interaction.

The emulation of the valence band is developed also in the region near  $\mathbf{k} = 0$ . But, due to the anisotropy of the effective mass besides the strong hybridization between light and heavy holes subbands, the decoupled bands assumption and the subsequent parabolic approach is not suitable anymore. This leads to a  $(4 \times 4)$  interaction matrix, known as Luttinger Hamiltonian [38].

The representation  $|J, m_J\rangle$  is used to include spin-orbit interactions,

$$\left|\frac{3}{2}, \frac{3}{2}\right\rangle = -\frac{1}{\sqrt{2}}|(X + iY) \uparrow\rangle = |HH \uparrow\rangle, \quad (2.20)$$

$$\left|\frac{3}{2}, \frac{1}{2}\right\rangle = -\frac{1}{\sqrt{2}}|(X + iY) \downarrow\rangle + \frac{2}{\sqrt{6}}|Z \uparrow\rangle = |LH \uparrow\rangle, \quad (2.21)$$

$$\left|\frac{3}{2}, \frac{-1}{2}\right\rangle = \frac{1}{\sqrt{2}}|(X - iY) \uparrow\rangle + \frac{2}{\sqrt{6}}|Z \downarrow\rangle = |LH \downarrow\rangle, \quad (2.22)$$

$$\left|\frac{3}{2}, \frac{-3}{2}\right\rangle = \frac{1}{\sqrt{2}}|(X - iY) \downarrow\rangle = |HH \downarrow\rangle, \quad (2.23)$$

where  $|HH(LH) \uparrow\rangle$  is the heavy hole (light hole) state with spin up and  $|HH(LH) \downarrow\rangle$  is the heavy hole (light hole) state with spin down. From here, this order will be hold. As a reminder, we need an effective Hamiltonian that describes the band structure of nanoscaled systems. We know that some symmetry aspects are still valid on these scales and whenever we act in the vicinity of  $\mathbf{k} = 0$ , the  $\mathbf{k} \cdot \mathbf{p}$  method is valid. With this, the Hamiltonian describing the heavy and light holes ( $HH$  and  $LH$ ) band structure, has the following form [39]

$$H = \frac{\hbar^2}{2m_e} \left[ \left( \gamma_1 + \frac{5}{2}\gamma_2 \right) k^2 - 2\gamma_2 \left( k_x^2 J_x^2 + k_y^2 J_y^2 + k_z^2 J_z^2 \right) - 4\gamma_3 \left( \{k_x, k_y\} \{J_x, J_y\} + \{k_y, k_z\} \{J_y, J_z\} + \{k_z, k_x\} \{J_z, J_x\} \right) \right], \quad (2.24)$$

where  $k$  is the kinetic operator,  $\gamma_i$  are the Luttinger parameters, and  $J_i$  are the angular momentum matrices for angular momentum  $j = 3/2$ .



In order to include an additional confinement in the system, we add a magnetic field in the  $z$  direction. We choose to use the symmetric gauge  $\mathbf{A} = (-y, x, 0)$  and the momentum operator takes the form  $\mathbf{\Pi} = \mathbf{p} + \frac{e}{c}\mathbf{A}$ , where  $e$  is the carrier charge,  $c$  the speed of light, and  $\mathbf{A}$  the potential vector. Furthermore, we consider the Zeeman effect of the carriers, since the degeneracy between spin up and down states is broken due to the applied magnetic field [40]. The Zeeman term is

$$H_Z = -2\mu_B (\kappa \mathbf{J} \cdot \mathbf{B} + q \mathbf{J}^3 \cdot \mathbf{B}) \quad (2.25)$$

where  $\mu_B$  is the Bohr magneton, and  $\kappa$  and  $q$  are Luttinger parameters.

By choosing  $\mathbf{B} = (0, 0, B)$ , the carrier experiences a confinement in the  $xy$ -plane in addition to the well confinement in  $z$  direction. The introduction of the magnetic field can be modeled as a quantum-oscillator like-problem by introducing  $\Pi_{\pm} = \Pi_x \pm i\Pi_y$ , and invoking both annihilation and creation operators,  $a$  and  $a^\dagger$ , as follows

$$\Pi_x = \frac{1}{\lambda_c} (\mathbf{a} + \mathbf{a}^\dagger), \quad (2.26)$$

$$\Pi_y = i \frac{1}{\lambda_c} (\mathbf{a} - \mathbf{a}^\dagger), \quad (2.27)$$

where  $\lambda_c = \sqrt{\frac{\hbar}{eB}}$ , it is possible to decrease or increase the Landau level index,  $N$  [41]. After including the magnetic field effects into  $H$ , equation (2.24), and add the  $H_Z$  term, equation (2.25), the total Hamiltonian  $H_L = H + H_Z$  for the system grown along [001] direction assumes the following matrix form

$$H_L = -\frac{\hbar^2}{2m_0} \begin{pmatrix} |HH \uparrow\rangle & |LH \uparrow\rangle & |LH \downarrow\rangle & |HH \downarrow\rangle \\ \hline P_1^\uparrow & R & Q & 0 & |HH \uparrow\rangle \\ R^* & P_2^\uparrow & 0 & -Q & |LH \uparrow\rangle \\ Q^* & 0 & P_2^\downarrow & 0 & |LH \downarrow\rangle \\ 0 & -Q^* & R^* & P_1^\downarrow & |HH \downarrow\rangle \end{pmatrix}, \quad (2.28)$$

where

$$P_1^{\uparrow(\downarrow)} = \frac{\gamma_1 - 2\gamma_2}{2} \partial_z^2 + \frac{\gamma_1 + \gamma_2}{2} \{\Pi_+, \Pi_-\} + (-) \frac{2}{\lambda_c^2} \frac{3}{2} \left( \kappa + \frac{9}{4}q \right), \quad (2.29)$$

$$P_2^{\uparrow(\downarrow)} = \frac{\gamma_1 + 2\gamma_2}{2} \partial_z^2 + \frac{\gamma_1 - \gamma_2}{2} \{\Pi_+, \Pi_-\} + (-) \frac{2}{\lambda_c^2} \frac{1}{2} \left( \kappa + \frac{1}{4}q \right), \quad (2.30)$$

$$R = i\sqrt{3}\gamma_3\Pi_-\partial_z, \quad (2.31)$$

$$Q = \sqrt{3}\frac{\gamma_2 + \gamma_3}{2}\Pi_-^2 + \sqrt{3}\frac{\gamma_2 - \gamma_3}{2}\Pi_+^2. \quad (2.32)$$

Note that  $R$  represents the coupling between light and heavy holes with the same spin and depends on the  $z$  confinement (quantum well confinement), whereas  $Q$  couples the LH and HH states with opposite spin by creation or annihilation of Landau levels.

In order to determine the electronic spectrum of carriers restricted to move in a two dimensional system like the one shown in Figure 2.1, we solve the next eigenvalue problem

$$\begin{aligned} H_L\Psi = & \\ & \frac{-\hbar^2}{2m_0} \begin{pmatrix} P_1^\dagger + V & R & Q & 0 \\ R^* & P_2^\dagger + V & 0 & -Q \\ Q^* & 0 & P_2^\dagger + V & 0 \\ 0 & -Q^* & R^* & P_1^\dagger + V \end{pmatrix} \sum_{n',m'} \begin{pmatrix} C_{1,n',m'} \phi_{n',m'}(x, y, z) \left| \frac{3}{2}, \frac{3}{2} \right\rangle \\ C_{2,n',m'} \phi_{n',m'}(x, y, z) \left| \frac{3}{2}, \frac{1}{2} \right\rangle \\ C_{3,n',m'} \phi_{n',m'}(x, y, z) \left| \frac{3}{2}, -\frac{1}{2} \right\rangle \\ C_{4,n',m'} \phi_{n',m'}(x, y, z) \left| \frac{3}{2}, -\frac{3}{2} \right\rangle \end{pmatrix} \\ & = E \sum_{n',m'} \begin{pmatrix} C_{1,n',m'} \phi_{n',m'}(x, y, z) \left| \frac{3}{2}, \frac{3}{2} \right\rangle \\ C_{2,n',m'} \phi_{n',m'}(x, y, z) \left| \frac{3}{2}, \frac{1}{2} \right\rangle \\ C_{3,n',m'} \phi_{n',m'}(x, y, z) \left| \frac{3}{2}, -\frac{1}{2} \right\rangle \\ C_{4,n',m'} \phi_{n',m'}(x, y, z) \left| \frac{3}{2}, -\frac{3}{2} \right\rangle \end{pmatrix} \\ & = E\Psi, \end{aligned} \quad (2.33)$$

where the term  $V$  emulates the quantum well potential. The walls have been considered as rigid infinite walls, and  $\phi$  is the envelope function which would be slowly varying [42]. This spatial wave function  $\phi$  is determined by solving the usual Schrödinger equation with the kinetic and potential part and has the next form [15]

$$\phi_{N,m}(x, y, z) = \frac{\lambda_c^{-1/2}}{\sqrt{2^N N! \sqrt{\pi}}} e^{-\frac{1}{2}\left(\frac{x-x_0}{\lambda_c}\right)^2} H_N\left(\frac{x-x_0}{\lambda_c}\right) e^{ik_y y} \sqrt{\frac{2}{L}} \sin\left(\frac{m\pi}{L}z\right), \quad (2.34)$$

where  $H_N$  is the Hermite polynomial of degree  $N$ ,  $x_0 = -\frac{\hbar}{eB}k_y$ ,  $m = 1, 2, \dots$  corresponds to the subband quantization along  $z$  direction, and  $\lambda_c = \sqrt{\frac{\hbar}{eB}}$  is the magnetic length.

As the magnetic field is been applied perpendicular to the confining walls ( $z$  direction), the problem can be separated into the longitudinal part, leading to the quantized energy subbands  $m$ , and a lateral confinement (in the  $xy$ -plane) as an oscillator model. Then, applying the operators  $\Pi_x$  and  $\Pi_y$ , defined in equations (2.26) and (2.27) respectively, into (2.33), we find new selection rules for the functions  $\phi$ . Thus, the eigenvalues problem is transformed into

$$\begin{aligned}
 H_L \Psi = & -\frac{\hbar^2}{2m_0} \begin{pmatrix} P_1^\dagger + V & R & Q & 0 \\ R^* & P_2^\dagger + V & 0 & -Q \\ Q^* & 0 & P_2^\dagger + V & 0 \\ 0 & -Q^* & R^* & P_1^\dagger + V \end{pmatrix} \begin{pmatrix} \phi_{N-2,m}(x, y, z) \left| \frac{3}{2}, \frac{3}{2} \right\rangle \\ \phi_{N-1,m}(x, y, z) \left| \frac{3}{2}, \frac{1}{2} \right\rangle \\ \phi_{N,m}(x, y, z) \left| \frac{3}{2}, -\frac{1}{2} \right\rangle \\ \phi_{N+1,m}(x, y, z) \left| \frac{3}{2}, -\frac{3}{2} \right\rangle \end{pmatrix} \\
 = & E \begin{pmatrix} \phi_{N-2,m}(x, y, z) \left| \frac{3}{2}, \frac{3}{2} \right\rangle \\ \phi_{N-1,m}(x, y, z) \left| \frac{3}{2}, \frac{1}{2} \right\rangle \\ \phi_{N,m}(x, y, z) \left| \frac{3}{2}, -\frac{1}{2} \right\rangle \\ \phi_{N+1,m}(x, y, z) \left| \frac{3}{2}, -\frac{3}{2} \right\rangle \end{pmatrix}. \tag{2.35}
 \end{aligned}$$

### 2.2.1 Quantum Well Conduction and Valence Band Calculations

Based on the above results, we proceed to diagonalize the eigenvalues matrix in (2.35) and obtain both conduction and valence band energy levels of a GaAs quantum well under an applied magnetic field. The explicit matrix Hamiltonian used in this study is reported in Appendix A. In table 2.1 [43], the values used for these calculations are displayed.

Given the valence band effective mass anisotropy, we shall also explore the effect of another growth directions beside the [001]. To this end, the results obtained for systems grown on (001) planes will be compared to those calculated for the high index surface (113), that has attracted considerable interest because of its peculiar dopant incorporation [44, 45] and optical response [46].

In order to describe the electronic structure of a system grown on an oriented substrate different from [001] it is necessary to apply the following coordinate transformation in

**Table 2.1:** Band structure parameters taken from ref [43] to apply in the simulations of electronic structure based on the  $\mathbf{k} \cdot \mathbf{p}$  method.

Parameter	value
$\gamma_1$	6.79
$\gamma_2$	1.88
$\gamma_3$	3.05
$m_e$	$0.07m_0$
$\kappa$	1.72
$q$	-0.18

Eq. (2.24) [39]:

$$k_x = \frac{\sin(\theta)}{\sqrt{2}}k_1 - \frac{1}{\sqrt{2}}k_2 + \frac{\cos(\theta)}{\sqrt{2}}k_3, \quad (2.36)$$

$$k_y = \frac{\sin(\theta)}{\sqrt{2}}k_1 + \frac{1}{\sqrt{2}}k_2 + \frac{\cos(\theta)}{\sqrt{2}}k_3, \quad (2.37)$$

$$k_z = -\cos(\theta)k_1 + \sin(\theta)k_3 \quad (2.38)$$

$$J_x = \frac{\sin(\theta)}{\sqrt{2}}J_1 - \frac{1}{\sqrt{2}}J_2 + \frac{\cos(\theta)}{\sqrt{2}}J_3, \quad (2.39)$$

$$J_y = \frac{\sin(\theta)}{\sqrt{2}}J_1 + \frac{1}{\sqrt{2}}J_2 + \frac{\cos(\theta)}{\sqrt{2}}J_3, \quad (2.40)$$

$$J_z = -\cos(\theta)J_1 + \sin(\theta)J_3, \quad (2.41)$$

where three new axes (1, 2, 3) were introduced, the angle between the axis 3, which corresponds to the grow direction, and the  $xy$ -plane is denoted by  $\theta$ , see Appendix B. Thus, for  $\theta$  varying from 0 to  $\pi/2$  the growth surface perpendicular to the 3 axis changes from (110) in succession to (111), (112), (113), until (001). In the case of the (113) plane,  $\sin(\theta) = \frac{3}{\sqrt{11}}$ ,  $\cos(\theta) = \sqrt{\frac{2}{11}}$ .

In Figure 2.2, we show the energy spectrum of a carrier in: (a) conduction and (b) valence band for a quantum well grown along the [001] direction, while in panel (c) we plot the hole energy of a quantum well grown along the [113] one. At the conduction band, Figure 2.2 (a), the levels are pure states, without any coupling between them,

whereas at the valence band a strong hybridization takes place between holes as can be seen in Figure 2.2 (b) and (c). This coupling at the valence band depends not only on the spatial confinement or the magnetic field but also on the growth orientation, as expected [47].

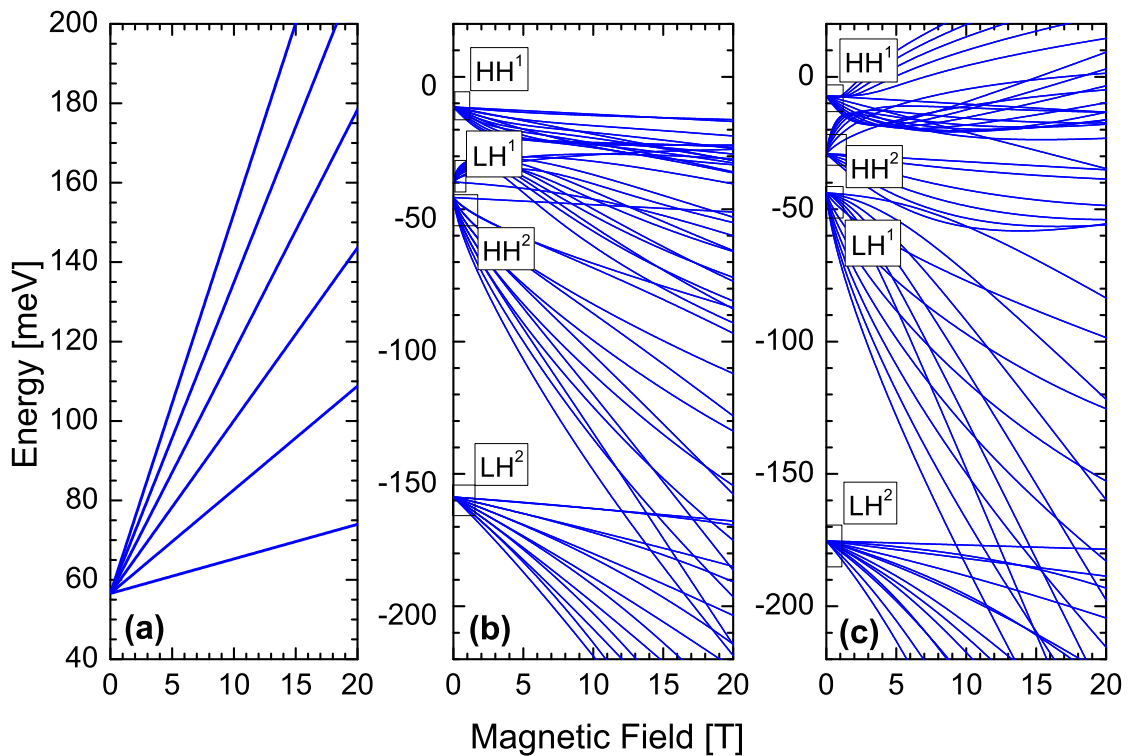


**Figure 2.2:** Energy spectrum of the first six Landau levels in (a) conduction band, (b) valence band of a GaAs quantum well grown in (001) direction and (c) along the (113) direction. The superscript correspond to the subband  $m = 1, 2$ . The predominant character of the carrier is indicated as  $HH$  or  $LH$  for heavy or light holes. It is noticeable the reorganization of hole subbands in (b) and (c) due to the different growth direction of GaAs quantum well.

## 2.3 Carrier-Phonon Interaction

The charge carriers in a polar semiconductor structure are subjected to collective excitations such as lattice vibrations. The vibrational modes of the atoms in the crystal lattice characterize the whole system and their displacements from the equilibrium position are described by the phonon concept. When an electron or hole interacts with

these displacements, a polarized cloud surrounds the carrier during its displacement, and this carrier-phonon interaction is called polaron [48–50].

This quasi-particle can be described in terms of phonon absorption and phonon emission. In polar crystals, the leading effects is triggered by the interaction with longitudinal-optical (LO) phonons <sup>1</sup> [51]. Under resonant conditions, when the energy difference between two neighboring electronic states is about one LO-phonon energy, the polaron effects are enhanced and this can be tuned with magnetic fields.

The modifications expected in the Landau levels can be listed in the followings ways: the levels are shifted; the mass renormalization provokes changes in the levels form; anticrossings emerge between states  $|\Psi\rangle$  and  $|\Psi\rangle + \hbar\omega$ , where  $\hbar\omega$  is the phonon energy. In order to know the effect of the electron-phonon and hole-phonon interaction on the energy levels, three different types of second-order perturbation methods were studied:

- the Rayleigh-Schrödinger perturbation theory [52],
- the Wigner-Brillouin perturbation method [52],
- and full diagonalization for degenerate states.

By including phonons in our electronic structure description, the wave function introduced before in (2.35) must include the number of phonons  $n$ , and takes the form  $|\Psi\rangle = |n\rangle|\phi_{xyz}\rangle|J, m_J\rangle$ . The annihilation and creation operations for phonons are ruled by [16]

$$b_{\mathbf{q}}|n\rangle = \sqrt{n}|n-1\rangle, \quad (2.42)$$

$$b_{\mathbf{q}}^\dagger|n\rangle = \sqrt{n+1}|n+1\rangle, \quad (2.43)$$

respectively, where  $\mathbf{q}$  is the phonon wave vector.

To understand the hole-phonon interaction effects in 2D [53] we start by analyzing two contrasting contributions: the deformation potential theory and the Fröhlich interaction. Let us first briefly discuss the contribution of the carrier-LO-phonons interaction

---

<sup>1</sup>There are two allowed frequencies of displacement know as the optical branch, and the acoustical branch. Considering phonons belonging to the optical branch means considering the movement of two atoms in the unit cell in opposite directions to each other, while in the acoustic mode they move together.

via deformation potentials [33], which is introduced by the Hamiltonian

$$H_{DP} = \sum_{\mathbf{q}} (M_q U(\mathbf{q}) b_{\mathbf{q}} e^{i\mathbf{q}\cdot\mathbf{r}} + h.c.), \quad (2.44)$$

where  $M_q = (\mathbf{q} \cdot \boldsymbol{\epsilon}_q) \left( \frac{\hbar}{2\rho\omega_{LO}A} \right)^{\frac{1}{2}}$ ,  $\boldsymbol{\epsilon}_q$  is the polarization,  $\rho$  and  $A$  are the density and area respectively, and  $U(\mathbf{q})$  is the deformation potential which is a model including scattering by transverse as well as longitudinal acoustic modes [54]. Still, one can prove that, up to second order, this interaction does not couple states in the conduction band, and the valence subbands in 2D can only be affected if the phonon is confined. Thus, this interaction will be dropped from our analysis.

In order to study the properties of charge carriers interacting with LO-phonons in systems with reduced dimensions, we used the Fröhlich interaction that accounts for the carrier coupling with the polarization cloud in the lattice of polar crystals [55]. The effects can be described by treating the interaction as follows [16]

$$H_I = \sum_{\mathbf{q}} (V_q b_{\mathbf{q}} e^{i\mathbf{q}\cdot\mathbf{r}} + h.c.), \quad (2.45)$$

where  $V_q$  is defined, in two dimension, as

$$V_q = -i\hbar\omega_{LO} \left( \frac{\sqrt{2\pi}\alpha}{Aq} \right)^{\frac{1}{2}} \left( \frac{\hbar}{m^*\omega_{LO}} \right)^{\frac{1}{4}}, \quad (2.46)$$

$$\alpha = \frac{e^2}{\hbar} \sqrt{\frac{m^*}{2\hbar\omega_{LO}}} \left( \frac{1}{\varepsilon_{\infty}} - \frac{1}{\varepsilon_0} \right), \quad (2.47)$$

$\alpha$  is called the Fröhlich coupling constant,  $\varepsilon_{\infty}$  and  $\varepsilon_0$  are the electronic and the static dielectric constants, respectively. The second order correction can be obtained by [56]

**Table 2.2:** Phonon interaction parameters taken from ref [25].

Parameter	Value
$\hbar\omega_{LO}$	36.1eV
$\alpha$	0.068

$$\Delta E_{\alpha} = - \sum_{\beta} \sum_{\mathbf{q}} \frac{|\langle \psi_{\beta} | H_I(\mathbf{q}) | \psi_{\alpha} \rangle|^2}{D_{\beta\alpha}}, \quad (2.48)$$

that can be interpreted as the polaron self-energy correction, where  $D_{\alpha\beta}$  is defined as

$$D_{\alpha\beta} = E_\beta - E_\alpha - \hbar\omega_{LO} + \Delta_\alpha. \quad (2.49)$$

The common Rayleigh - Schrödinger (RS) model fixes  $\Delta_\alpha = 0$  and describes well the ground state out of resonance when either  $|E_\beta - E_\alpha| \ll \hbar\omega_{LO}$  or  $|E_\beta - E_\alpha| \gg \hbar\omega_{LO}$ . In turn, in the Wigner - Brillouin (WB) perturbation theory approaches  $\Delta_\alpha = \Delta E_\alpha + i\delta$ , where the inter-dependence of the variables clearly requires a self-consistent solution, and  $\delta$  is a vanishing imaginary part.

To evaluate the matrix element  $\langle \psi_\beta | H_I(\mathbf{q}) | \psi_\alpha \rangle$ , one can separate (2.45) into phonon absorption  $H_I^{abs}$  and emission  $H_I^{emi}$  terms,

$$H_I = H_I^{abs} + H_I^{emi} \quad (2.50)$$

$$= \sum_{\mathbf{q}} V_q b_{\mathbf{q}} e^{i\mathbf{q}\cdot\mathbf{r}} + \sum_{\mathbf{q}} V_q^* b_{\mathbf{q}}^\dagger e^{-i\mathbf{q}\cdot\mathbf{r}}. \quad (2.51)$$

For absorption processes we have

$$\langle \psi_\beta | H_I^{abs} | \psi_\alpha \rangle = V_q \frac{1}{q^{1/2}} \langle n' | b_{\mathbf{q}} | n \rangle \langle J', m'_J | J, m_J \rangle \langle \phi'_{xyz} | e^{i\mathbf{q}\cdot\mathbf{r}} | \phi_{xyz} \rangle, \quad (2.52)$$

where  $\phi_{xyz}$  is the envelope function and has the following form

$$\begin{aligned} \langle \phi'_{xyz} | e^{i\mathbf{q}\cdot\mathbf{r}} | \phi_{xyz} \rangle &= \int_{-\infty}^{\infty} dx \frac{e^{-\frac{1}{2}\left(\frac{x-x_0}{\lambda_c}\right)^2} e^{-\frac{1}{2}\left(\frac{x-x'_0}{\lambda_c}\right)^2}}{\lambda_c \sqrt{2^{N-N'} N! N'! \pi}} e^{ixq_x} \text{H}_N \left( \frac{x-x_0}{\lambda_c} \right) \text{H}_{N'} \left( \frac{x-x'_0}{\lambda_c} \right) * \\ &* \int_{-\infty}^{\infty} dy e^{iyk_y} e^{iyq_y} e^{-iyk'_y} * \\ &* \int_0^L dz \sin \left( \frac{m\pi}{L} z \right) \sin \left( \frac{m'\pi}{L} z \right) e^{izq_z}. \end{aligned} \quad (2.53)$$

The analytical solution for all the integrals in  $\langle \phi'_{xyz} | e^{i\mathbf{q}\cdot\mathbf{r}} | \phi_{xyz} \rangle$  is given by [57]

$$\begin{aligned} \langle \phi'_{xyz} | e^{i\mathbf{q}\cdot\mathbf{r}} | \phi_{xyz} \rangle &= 2^{\frac{|N-N'|}{2}} \min \left( \sqrt{\frac{N!}{N'!}}, \sqrt{\frac{N'!}{N!}} \right) e^{-\frac{\lambda_c^2}{4} \left[ (k_y - k'_y)^2 + 2(k_y - k'_y)iq_x + q_x^2 \right]} * \\ &* L^{\frac{|N-N'|}{2}} \frac{\lambda_c^2}{2} \left[ (k_y - k'_y)^2 + q_x^2 \right] * \end{aligned}$$



$$* \left[ \frac{\lambda_c^2}{2} \left( \text{sgn}(N - N') (k_y - k'_y) + iq_x \right) \right]^{|N-N'|} \delta_{m,m'} \delta_{k_y - k'_y, q_y}, \quad (2.54)$$

where  $L_n^\alpha$  are the associated Laguerre polynomials,  $\lambda_c$  the magnetic length, and  $\text{sgn}$  the signal function.

The probability amplitude for the absorption processes is given by

$$\begin{aligned} \left| \langle \psi_\beta | H_I^{abs} | \psi_\alpha \rangle \right|^2 &= \delta_{n',n-1} |\langle J, m'_J | J, m_J \rangle|^2 \\ &\sum_{\mathbf{q}} V_q^2 \frac{1}{\sqrt{q_x^2 + q_y^2}} 2^{|N-N'|} \min \left( \frac{N!}{N'}, \frac{N'}{N!} \right) \delta_{m,m'} \\ &e^{-\frac{\lambda_c^2}{2} (q_x^2 + q_y^2)} \left[ L_{\min(N,N')}^{|N-N'|} \frac{\lambda_c^2}{2} (q_x^2 + q_y^2) \right]^2 \left[ \frac{\lambda_c^2}{4} (q_x^2 + iq_y^2) \right]^{|N-N'|}. \end{aligned} \quad (2.55)$$

The sum over the phonon wave vector can be converted into integrals as  $\sum_{\mathbf{q}} \rightarrow \frac{A}{(2\pi)^2} \int dq_x dq_y$ . In the case of 2D Landau levels, we were able to obtain analytic solutions for these integrals [57]

$$\begin{aligned} \frac{A}{(2\pi)^2} \int dq_x dq_y \left| \langle \psi_\beta | H_I^{abs} | \psi_\alpha \rangle \right|^2 &= \min \left( \frac{N!}{N'}, \frac{N'}{N!} \right) \delta_{n',n-1} |\langle J, m'_J | J, m_J \rangle|^2 * \\ &\frac{A}{(2\pi)^2} V_q^2 \int_0^\infty \int_0^{2\pi} q_\perp dq_\perp d\theta \frac{1}{q_\perp} e^{-\frac{\lambda_c^2}{2} q_\perp^2} \left[ L_{\min(N,N')}^{|N-N'|} \frac{\lambda_c^2}{2} q_\perp^2 \right]^2 \left[ \frac{\lambda_c^2}{2} q_\perp^2 \right]^{|N-N'|} \delta_{m,m'}. \end{aligned} \quad (2.56)$$

The right side of equation (2.56) has an analytical solution, which leads to

$$\begin{aligned} \sum_{\mathbf{q}} \left| \langle \psi_\beta | H_I^{abs} | \psi_\alpha \rangle \right|^2 &= \delta_{n',n-1} |\langle J, m'_J | J, m_J \rangle|^2 (\hbar\omega_{LO})^2 \alpha \frac{1}{\lambda_c} \sqrt{\frac{\hbar}{4m^*\omega_{LO}}} \\ &\frac{\Gamma \left( \frac{1}{2} + |N - N'| \right) \Gamma(1 + |N - N'| + \min(N, N'))}{\min(N, N')! \min(N, N')! \Gamma(1 + |N - N'|)} \\ &\left\{ \frac{d^{\min(N,N')}}{dh^{\min(N,N')}} \left[ \frac{F \left( \frac{\frac{1}{2} + |N - N'|}{2}, \frac{3}{4} + \frac{|N - N'|}{2}; 1 + |N - N'|; \frac{4h}{(1+h)^2} \right)}{(1+h)^{1+|N-N'|} \left( \frac{1+h}{1-h} \right)^{\frac{1}{2} + |N-N'|}} \right] \right\}_{h=0}, \end{aligned} \quad (2.57)$$

where  $\Gamma(z)$  is the Euler gamma function and  $F(a, b; c; z)$  is the hypergeometric function. These expressions were used for both the conduction and valence band renormalization as summarized in the following.

In Figure 2.3, we show the polaron self-energy correction  $\Delta E_\alpha$  calculated using (2.48), for the fourth electronic state as a function of the magnetic field. The Figure 2.3(a) illustrates the results obtained with the Wigner-Brillouin approximation and Figure 2.3(b) shows the Rayleigh-Schrödinger correction. Note that both WB and RS methods match far from resonance (at  $\sim 7\text{T}$  and  $\sim 10\text{T}$ ). Naturally, in the RS approximation, Figure 2.3(b), divergences appear close to the resonant conditions  $D_{\alpha,\beta} = 0$  (when  $E_\beta - E_\alpha - \hbar\omega_{LO} = 0$ ).

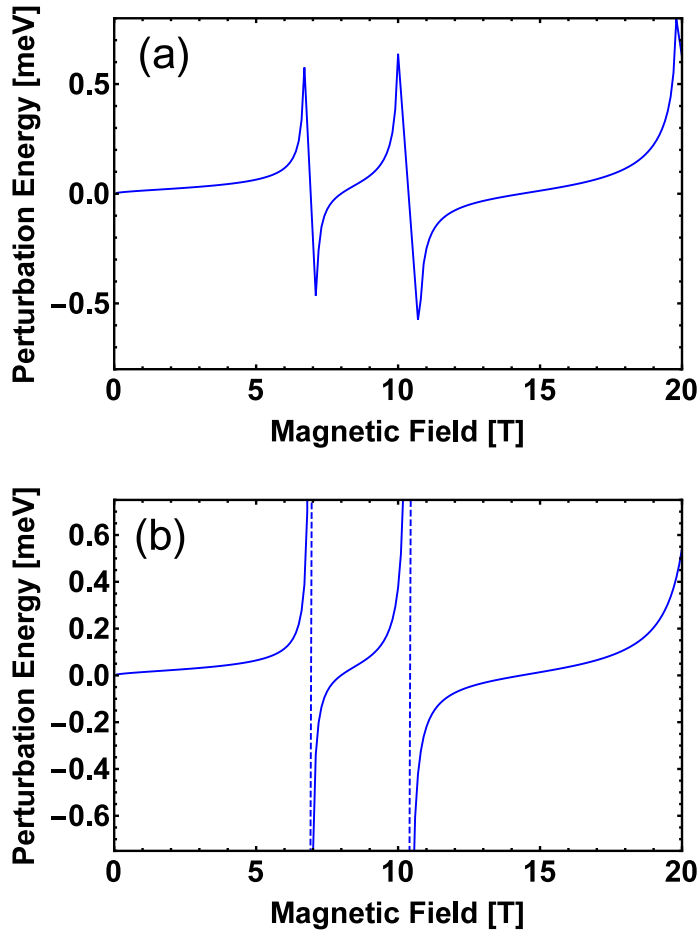


**Figure 2.3:** Energy correction calculated using (2.48) for the third conduction band state using (a) Wigner-Brillouin and (b) Rayleigh-Schrödinger method.

In the WB method  $\Delta_\alpha = \Delta E_\alpha + i\delta$ , this allows us to extract additional information about the interaction. The real part of the self-energy shift, Figure 2.3(a), characterizes the energy correction due to phonon interaction. Besides, the imaginary part of the energy correction, which it is plotted in Figure 2.4, indicates the finite lifetime energy broadening of the excited electron Landau levels due to the polaron renormalization.

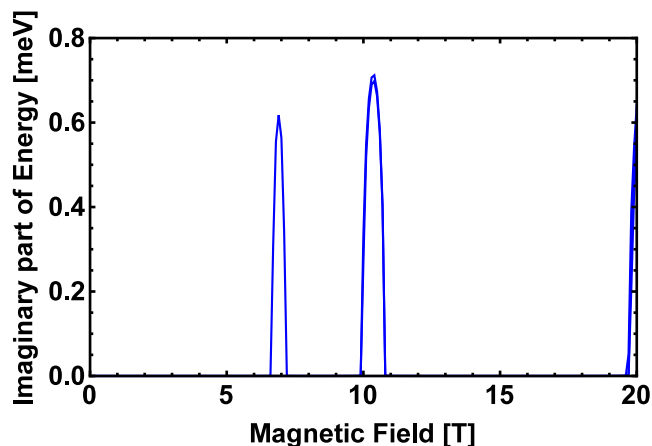


**Figure 2.4:** The imaginary part of the self-energy perturbed arise from the imaginary part of WB.  $\delta = 0.001$  meV.

In resonant conditions, the electronic states capable to absorb one phonon become hybrid, and their lifetimes determine the total energy loss rate of carriers [32]. This has real implications in the carrier dynamics that will be explored in the next chapter. The RS and WB approximations do not give the actual pinning behavior of the electron energies out of resonance. For that reason we introduce the carrier-phonon interaction within the  $\mathbf{k} \cdot \mathbf{p}$  model by using a full diagonalization. The fact that the energy states are fully quantized, supports this approach and we expand the Hamiltonian in (2.35) in the basis of  $|\psi\rangle = |0\rangle|\phi_{xyz}\rangle|J, m_J\rangle$  and  $|\psi\rangle = |1\rangle|\phi_{xyz}\rangle|J, m_J\rangle$  functions. The corresponding energy spectrum is obtained by diagonalizing the Hamiltonian including the electron-phonon interaction terms (2.52). As shown in Figure 2.5 for the conduction band, the anticrossings are produced at critical magnetic fields. These anticrossings correspond to the perfect hybridization of  $|\psi\rangle = |0\rangle|\phi_{xyz}\rangle|J, m_J\rangle$  and  $|\psi\rangle = |1\rangle|\phi_{xyz}\rangle|J, m_J\rangle$  states which becomes a complementary interpretation of the increased life-time broadening of Landau levels discussed before.

We can see that the interaction with phonons modifies the system configuration but preserves the asymptotic behavior. The advantage of this approach is the perfect blending to the matrix format of the  $\mathbf{k} \cdot \mathbf{p}$  and allows direct application to the study of these effects also in the valence subbands.

The full diagonalization calculation allowed the possibility of observing a peculiar effect induced by the LO-phonon interaction: the appearance of heavy-light hole coupling

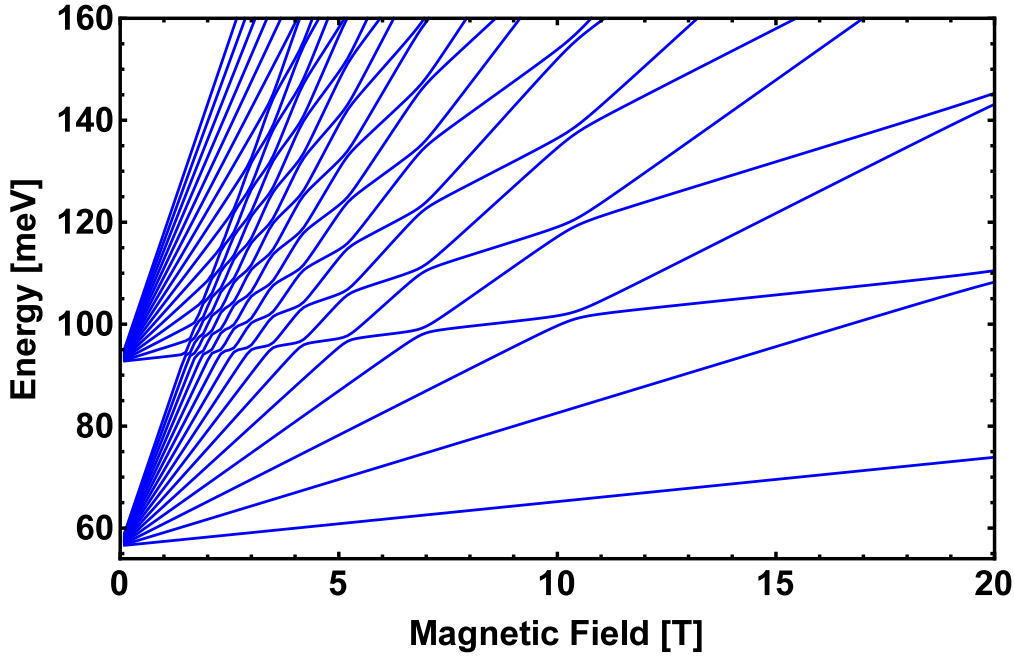


**Figure 2.5:** Conduction band levels corrected by full diagonalization. The upper branch corresponds to states with one phonon energy above  $E = E_{states} + \hbar\omega_{LO}$ . The zero energy is at the top of the valence band.

induced by polaron renormalization as seen from Figure 2.6.

Note that, according to equation (2.52), the Fröhlich interaction allows the direct coupling only between states of the same character. However, because of the strong intraband mixing, the phonon interaction can couple the heavy and light hole levels. Other remarkable fact is the difference in the effective masses for the two growth directions selected in the model, affecting the subbands relative position and subsequently the position of the hole-phonon resonances.

The effect is more vivid by increasing the quantum well width, as displayed in Figs. 2.7 and 2.8, calculated for twice large well ( $L = 100\text{\AA}$ ). We understand that it can be difficult to elucidate details of the electronic structure within the mesh of valence band Landau levels. For that reason the energy spectrum is complemented with the information contained in the expansion coefficients  $C_{Nm}$  of the respective hole states as function of the magnetic field strength. They define the character of each given state and characterize the degree of the hybridization of the valence band energy level.

Some states of the Figure 2.7 and Figure 2.8, labeled in Roman digits, have been

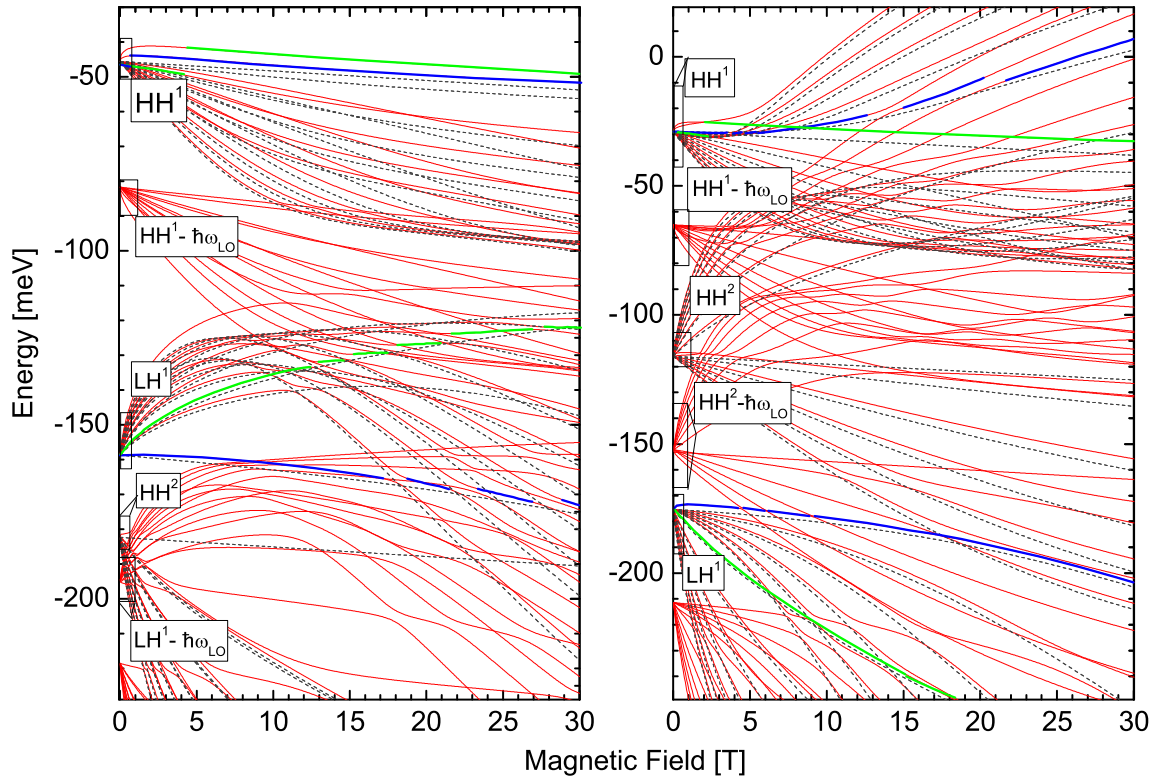


**Figure 2.6:** In red, the valence band energy levels for the [001] (left) and [113] (right) quantum well. The gray dot lines correspond to non phonon interaction case. At very low magnetic fields, the hole states are almost pure, but become hybrid as the external magnetic field,  $B$ , increases. The lowest energy levels with heavy and light hole characters are indicated in green (for spin up) and blue (down spin). The width used is  $L = 50\text{\AA}$  and the super-index denotes the  $m$ th state due to the quantum well confinement.

chosen to prove the main hypothesis that was risen in this part of the Thesis: the contributions of phonons to extra heavy and light-hole mixing. In Figs. 2.9 and 2.10, the weight coefficients of the wave functions are plotted as function of the magnetic field strength for the states highlighted in Figures 2.7 and 2.8, respectively. Solid curves represent the components with no phonon contribution while the dashed ones correspond to those involving one phonon. Note that at the regions of clear energy anticrossings, the phonon components assume a dominant role indicating that resonant hole-phonon coupling can take place between states with predominant heavy and light hole character. These features are also clearly spin-dependent.

Such an effect will imply that under resonant conditions, the carrier life-time and sub-

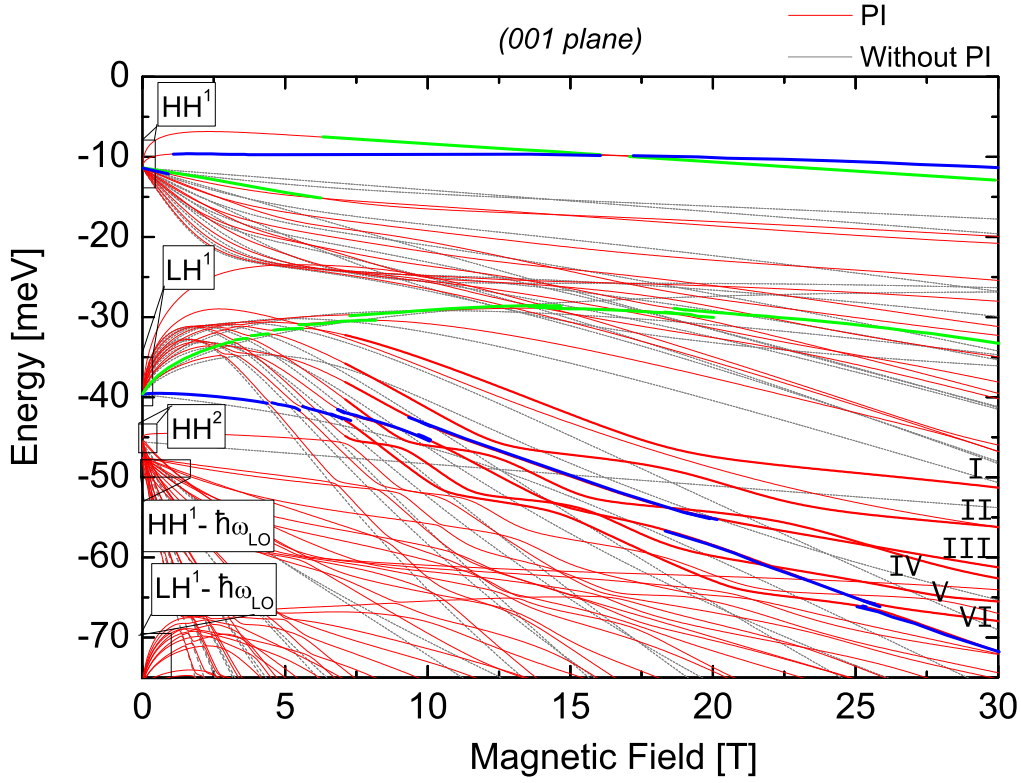


**Figure 2.7:** Energy spectrum obtained by an exact diagonalization of the  $H_L + H_I$  (given by equations (2.35) and (2.45) respectively). The holes are confined in a GaAs quantum well grown on a (001) plane with  $L = 100\text{\AA}$ . The gray dot lines correspond to non phonon interaction case. Green lines (blue lines) correspond to states with a predominant contribution of the ground state of heavy or light holes with spin up (spin down). Highlighted lines are used to visualize phonons effects.

sequently the hole relaxation can be strongly affected and tuned by the magnetic field. In the next chapter, a consequence of these effects will be discussed and certain peculiar behaviors obtained experimentally related to the spin-relaxation will be analyzed.

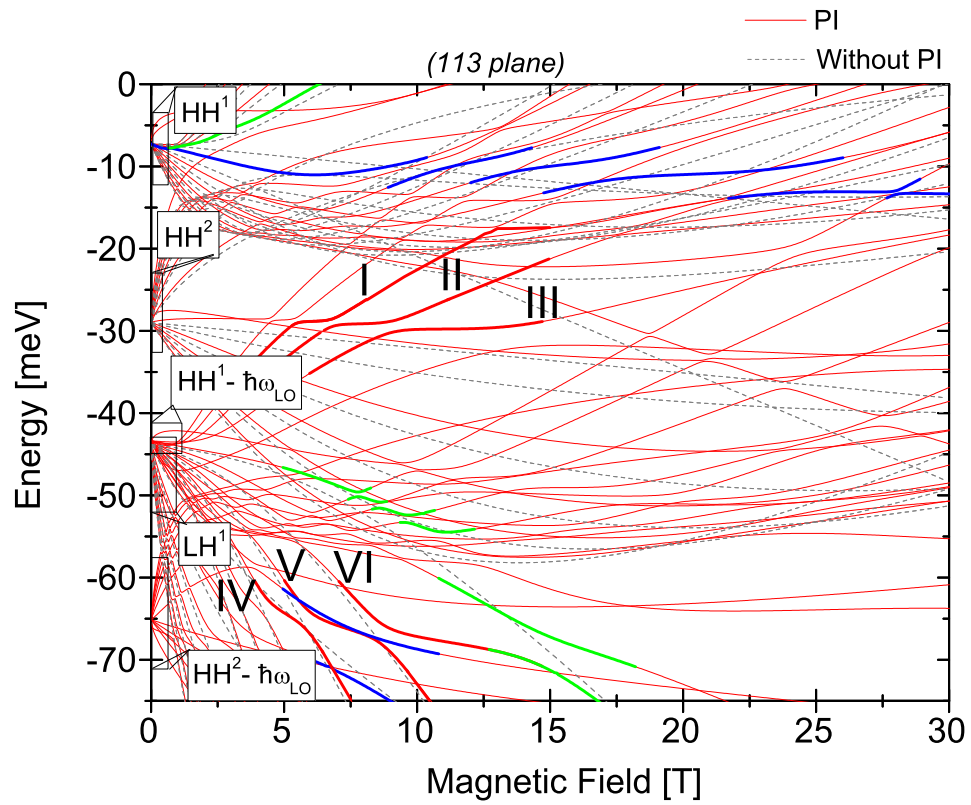


**Figure 2.8:** The same as Figure 2.7 but for confined holes in a GaAs quantum well grown on a (113) plane.

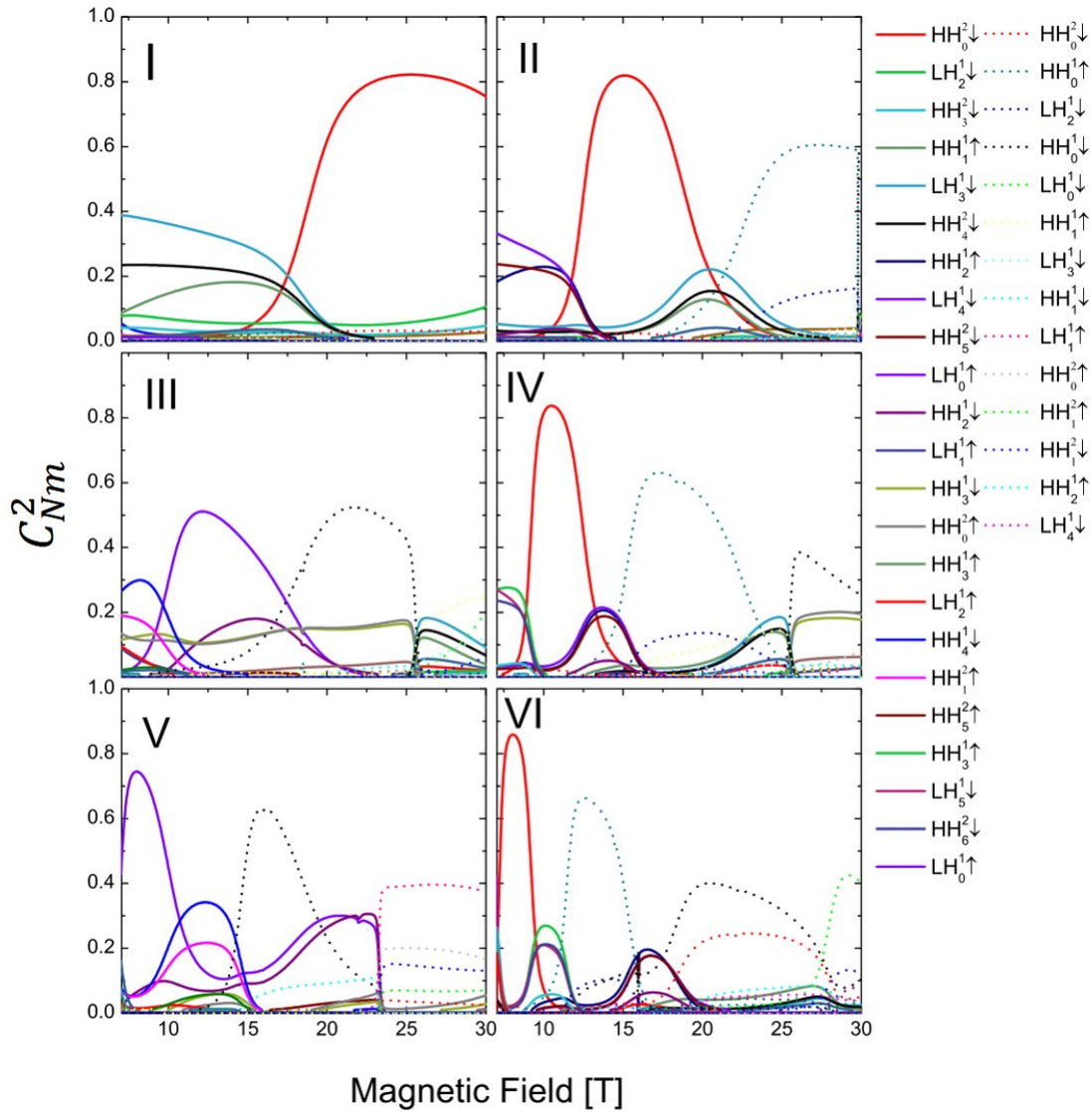


**Figure 2.9:** Contribution of the main basis components  $C_{Nm}$  to the highlighted states of Figure 2.7 for a quantum well grown along [001] direction. Dashed curves correspond to the components involving one phonon.



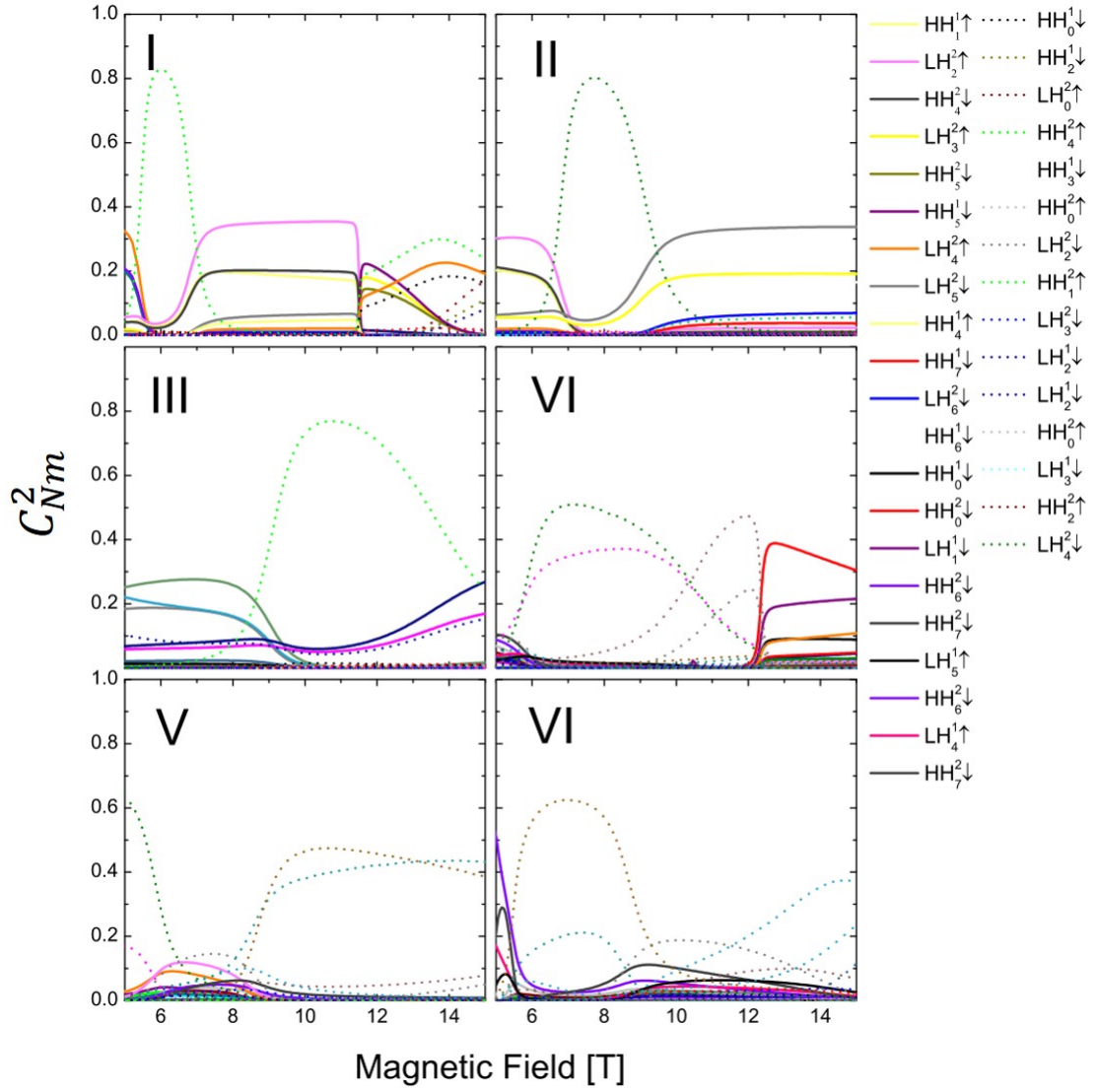


**Figure 2.10:** Contribution of the main basis components  $C_{Nm}$  to the highlighted states of Figure 2.8 for a quantum well grown along [113] direction. Dashed curves correspond to the components involving one phonon.



# Chapter 3

## Spin-Resolved Photo-Generation Filtering Induced by Phonon Emission

The Stranski-Krastanov growth technique appears as a widespread method used to synthesize self-assembled quantum dots [58]. This growth mode, takes advantage of the lattice mismatch between different semiconductor compounds and takes place, in general, after the epitaxial deposition of a thin film referred as the wetting layer. The self-assembled quantum dots will subsequently grow on this surface.

The wetting layers allow controlling the strain fields that lead to the quantum dot formation and have unavoidable effects in their electronic structure and, in turn, affect the optical properties. One of the most intensely investigated quantum dot systems are those built on the basis of InGaAs alloys that have gained increasing importance in recent years due to their application in long-wavelength optoelectronic devices [43, 59]. In such systems, the spontaneous formation of InAs dots takes place after the deposition of a thin InGaAs wetting layer (that can be assumed as a two dimensional confinement layer) [60].

Considerable attention has been paid to the charge (and spin) dynamics that lead to the carrier capture in quantum dots and the role played by the wetting layers [61–66]. It is assumed, for instance, that in InGaAs quantum dots in a GaAs matrix, the carriers can be efficiently trapped in the quantum dots in both ways: (i) directly from

the matrix and (ii) via the wetting layer [67]. In particular, the optical injection of electron and hole spins into a quantum dot system is a fundamental tool for solid state quantum information processing. Like in single atoms, in quantum dots, spin polarization can be created by means of optical pumping with polarized light thanks to well defined optical selection rules. The selection rules determine the exchange of angular momentum between incoming photons and a quantum state comprising one or several electrons and holes. In the most general case, light absorbed by a quantum dot creates a superposition of spin up and spin down states, thus reducing the maximum attainable spin polarization. Yet, there are special situations where the selection rules allow a 100 percent spin polarization using circularly polarized light.

In general, to attain high degree of spin polarization and long term spin coherence, resonant excitation conditions are chosen. Near resonant excitation energy of the relevant spin states, the angular momentum transfer is maximized as well as the coherence between photons and spins. The dynamics of the just created spin is governed in this case by pure spin dephasing mechanisms like anisotropic exchange interaction and hyperfine coupling [68]. Non resonant spin injection mechanisms, on the other hand, involve optical selection rules for the excited states and additional spin relaxation processes. Thus, the non-resonant pathways for optical spin injection have been traditionally disregarded in favor of the resonant ones, however these avoid intermediary mechanisms or states that could be exploited for filtering phenomena such as spin-bottleneck [69, 70]. In this chapter, we investigate an unexplored nonresonant pathway to inject oriented spins from high energy extended bulk states into localized InGaAs/GaAs quantum dot states. The sample studied is represented in the upper diagram of Figure 3.1. The carrier relaxation path was assessed through the sample photoluminescence that allows observing the emission lines from practically all the intermediary steps from the bulk states towards those confined in the quantum dots as shown in the lower panel of Figure 3.1.

The path exploits a magnetophonon resonance channel acting on hot electrons and a spin blocking mechanism acting on intermediate states of the relaxation path. Together, they allow a non-equilibrium high spin polarization in the quantum dot. The effect is reported for both, quantum dot ensembles and single quantum dots and might open new routes for nonresonant optical injection of spins in solid state. The sam-

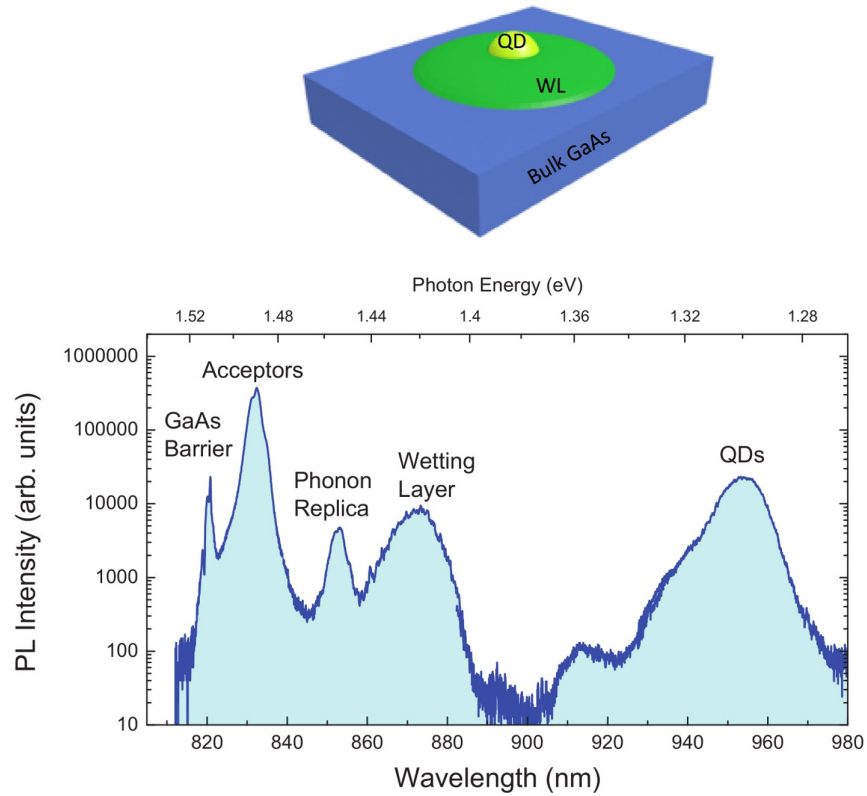


**Figure 3.1:** Upper panel: sketch of the various layers of the structure under study. Lower panel: photo-luminescence spectrum of the sample labeling the various contributions provided by the collaborators at the Micro-electronics Institute of Madrid.

ples used in this study were grown and characterized by our colleagues at the Micro-electronics Institute of Madrid, Spain. Undoped substrates were used and the growth conditions were optimized for low quantum dot density and emission wavelength around 980 nm.

To investigate the spin dynamics the samples were embedded in a cryogen-free cryostat and investigated by magneto-photoluminescence (PL) in back-scattering Faraday configuration at low temperature (4-77 K). For single quantum dot investigation a confocal micro-PL setup was used.

To assess a variety of spin pumping conditions and the different spin relaxation paths, polarization optics were used to change from linear to circular basis both in the excitation and collection. In the following, light helicity refers to a fixed laboratory frame attached to the emission light path. Figure 3.2 (a-c) shows the photoluminescence spectra obtained at 0T and 4.2K for the GaAs band edge, ensemble quantum dot ground state and single quantum dot neutral exciton at their corresponding spectral regions,

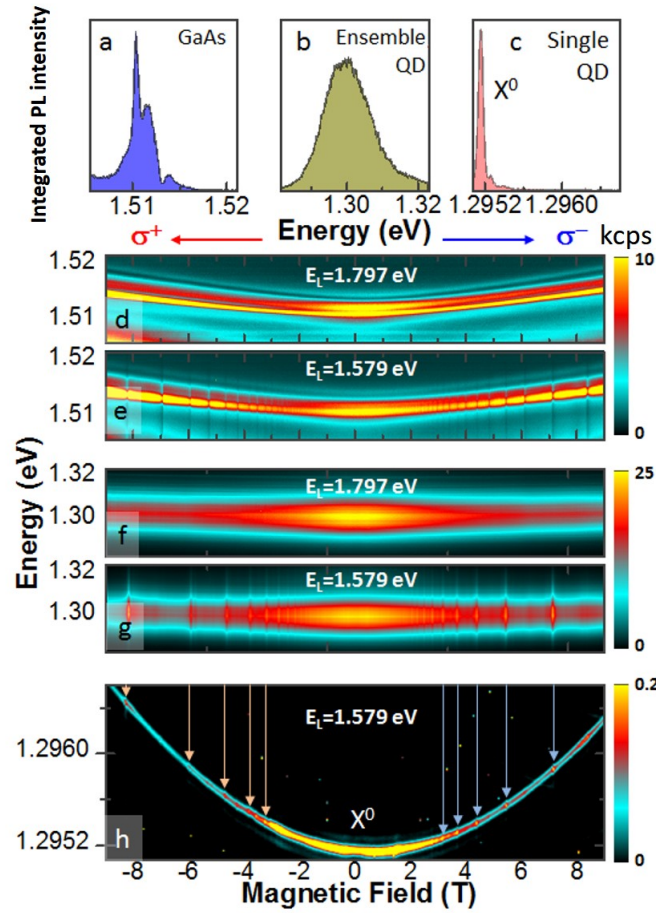


**Figure 3.2:** (a-c) Photoluminescence spectra obtained with no magnetic field applied at  $T=4.2\text{K}$  for the GaAs band edge, ensemble quantum dot ground state and single quantum dot neutral exciton. Contour plots of the emission as function of the magnetic field in each spectral region is showed in the lower panels. Panels (d)(f) stand for experiments done with continuous wave laser excitation of energy  $E_L = 1.797\text{eV}$ , coming from a temperature stabilized laser diode emitting at  $690.0\text{nm}$  with power stability better than 2 %. Correspondingly, panels (e)(g)(h) stand for experiments done with  $E_L = 1.579\text{eV}$ . Courtesy of our collaborators at the Micro-electronics Institute of Madrid.

respectively. They are representative of droplet epitaxy InGaAs/GaAs quantum dots with ensemble and single full width at half maximum (FWHM) of  $17\text{meV}$  and  $69\mu\text{eV}$ , respectively. The GaAs band edge emission show narrow peaks dominated by the exciton bound to neutral acceptor transition, as expected for high quality intrinsic GaAs. The lower panels in Figure 3.2 show contour plots of the emission obtained sweeping the magnetic field from  $-9$  to  $9\text{T}$  in each spectral region. Figure 3.2 (d)(f) stand for

experiments done with continuous wave laser excitation of energy  $EL = 1.797\text{eV}$  coming from a temperature stabilized laser diode emitting at  $690.0\text{nm}$  with power stability better than 2%. Correspondingly, Figure. 3.2 (e)(g)(h) stand for experiments done with a CW laser diode stabilized at  $785.0\text{nm}$  ( $EL = 1.579\text{eV}$ ). Both lasers were linearly polarized and continuously monitored to normalize the emission intensity by the laser power. In both situations, well-known diamagnetic and zeeman (orbital and spin) energy shifts can be identified for each transition which do not depend on the excitation energy. Yet, both excitation energies, being above the GaAs band edge, result in a very different evolution of the integrated PL intensity and degree of circular polarization. For the laser with energy  $EL = 1.579\text{eV}$ , the  $\sigma^+$  and  $\sigma^-$  components of the emitted light show sharp resonances with  $1/B$  periodicity as shown in Fig. 3.2 (e)(g). The oscillations can be mapped down to the single quantum dot level resulting in brighter spots in the parabolic dispersion of the neutral exciton shown in Figure 3.2 (h). Both the optical excitation and detection were performed by controlling the light polarization (either linear or circular), thus spin contributions were optically resolved as a function of B. The period and amplitude of these oscillations can be better analyzed integrating the  $\sigma^+$  and  $\sigma^-$  intensities as a function of B and normalizing to their values at 0T. The panels in Figure 3.3 show the results obtained for the ensemble quantum dot and GaAs band edge. Given the selection rules at play in III-V semiconductors, an imbalance of the  $\sigma^+$  and  $\sigma^-$  emission intensity reflects an unequal population of spin-up and spin-down electrons.

In panels (a) and (b) of Figure 3.3 one may note that the magnetic field resonances disappear (dashed lines) once the incident laser energy is shifted beyond certain resonance threshold. Another interesting feature that can be noticed is the fact that, for the GaAs band edge, all the resonances appear regardless the polarization configuration for excitation and collection. However, for the quantum dots this is no longer the case when a linearly polarized light is used and a clear spin filtering takes place, Figure 3.3(a).

For excitation with circularly polarized light, it is possible to map the transitions emission for both  $\sigma^+$  and  $\sigma^-$  independently of the collection as showed in Figure 3.3(c-f). The highest emissions due to clockwise circularly polarized or anticlockwise circularly polarized light are reached at specific values of magnetic field where resonant condi-

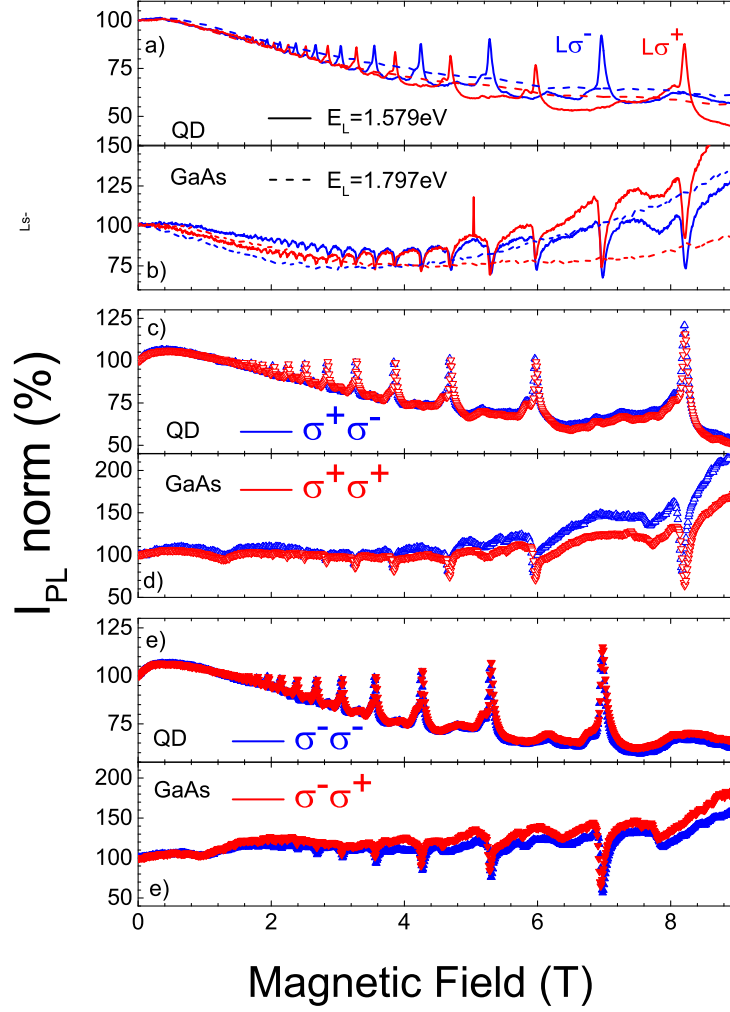


**Figure 3.3:** Integrated bulk and quantum dot photoluminescence intensities as a function of  $B$ . The polarization configuration for excitation and collection is denoted by  $\sigma^\alpha$  and  $L\sigma^\alpha$  where  $L$  stands for linearly polarized excitation. The spectra are normalized to the values at 0T.

tions are satisfied. Besides, one should note that the maxima in Figure 3.3 (c-d) are shifted with respect to those in Figure 3.3 (e-f).

This puzzling effect will be discussed in what follows and, at the end, we will be able to emulate various polarization configurations for both light absorption and emission processes. We shall discuss the effects of phonons in the communication process between bulk, and the 2D states in the wetting layer which leads to the carrier relaxation towards the quantum dots.



### 3.1 Theoretical Simulation

By analyzing the optical response in this kind of connected systems (due to the growth conditions bulk/wetting layer/quantum dot appear in sequence) when a magnetic field is applied, two challenging questions arise: *what is the potential interference of 2D Landau levels in the wetting layer for the relaxation from bulk 3D states towards fully confined states in quantum dots* and *is there a potential phonon assistance?*

Thus, we build the Figure 3.4 to illustrate the carrier dynamics in the structure, where the dashed arrows correspond to the optical excitation and emission, whereas the continuous arrows represent the relaxation processes that ultimately result in the quantum dot emission. Both the optical excitation and detection were performed by controlling the light polarization (either linear or circular), thus spin contributions were optically resolved.

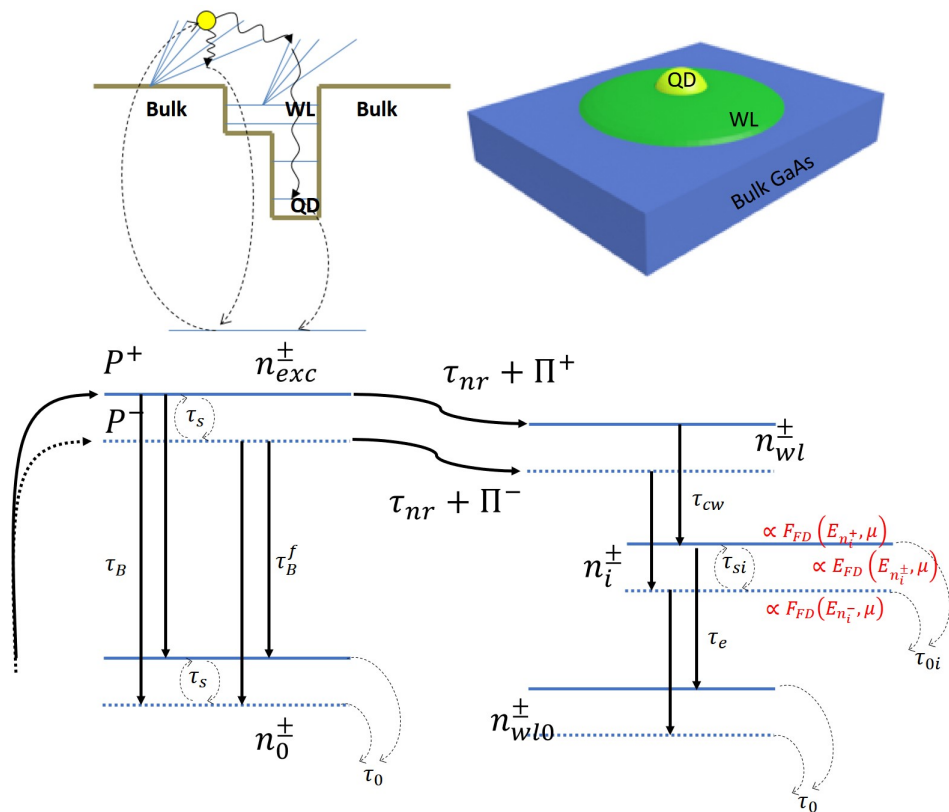


**Figure 3.4:** Upper panel: sketch of the potential profile of a system Bulk/wetting layer (WL)/quantum dot (QD). Lower panel: schematic representation of the spin-resolved dynamics.

A theoretical model based on carrier densities dynamics as shown in Figure 3.4 was

proposed taking into account both spin conserving and spin-flipping channels. The relations are described through the equations

$$\begin{aligned} \frac{dn_{exc}^{\pm}}{dt} = & P^{\pm} - \frac{n_{exc}^{\pm}}{\tau_B} - \frac{n_{exc}^{\pm}}{\tau_B^{flip}} - \left( \Pi^{\pm} + \frac{1}{\tau_{nr}} \right) n_{exc}^{\pm} - \frac{n_{exc}^{\pm}}{\tau_s} f(E_{exc}^{\pm} - E_{exc}^{\mp}) + \\ & + \frac{n_{exc}^{\mp}}{\tau_s} f(E_{exc}^{\mp} - E_{exc}^{\pm}), \end{aligned} \quad (3.1)$$

$$\frac{dn_0^{\pm}}{dt} = \frac{n_{exc}^{\pm}}{\tau_B} + \frac{n_{exc}^{\mp}}{\tau_B^{flip}} - \frac{n_0^{\pm}}{\tau_0} - \frac{n_0^{\pm}}{\tau_s} f(E_0^{\pm} - E_0^{\mp}) + \frac{n_0^{\mp}}{\tau_s} f(E_0^{\mp} - E_0^{\pm}), \quad (3.2)$$

$$\frac{dn_{WL}^{\pm}}{dt} = \left( \Pi^{\pm} + \frac{1}{\tau_{nr}} \right) n_{exc}^{\pm} - \frac{n_{WL}^{\pm}}{\tau_{cw}} f_{FD}(E_{n_i^{\pm}}, \mu), \quad (3.3)$$

$$\begin{aligned} \frac{dn_i^{\pm}}{dt} = & \frac{n_{exc}^{\pm}}{\tau_{ce}} f_{FD}(E_{n_i^{\pm}}, \mu) + \frac{n_{WL}^{\pm}}{\tau_{cw}} f_{FD}(E_{n_i^{\pm}}, \mu) - \frac{n_i^{\pm}}{\tau_e} + \frac{n_i^{\mp}}{\tau_{si}} f_{FD}(E_{n_i^{\pm}}, \mu) - \\ & \frac{n_i^{\pm}}{\tau_{si}} f_{FD}(E_{n_i^{\mp}}, \mu), \end{aligned} \quad (3.4)$$

$$\frac{dn_{WL0}^{\pm}}{dt} = \frac{n_i^{\pm}}{\tau_e} - \frac{n_{WL0}^{\pm}}{\tau_0}, \quad (3.5)$$

where superscripts indicate the spin state, up (+) or down (-), the  $n_{exc}^{\pm}$  and  $n_0^{\pm}$  characterize the carrier density of the excited and bulk ground states, respectively. The carrier density through the wetting layer states is labeled as  $n_{WL}^{\pm}$ , for the excited levels, and  $n_{WL0}^{\pm}$ , for the ground levels. Here  $P^{\pm}$  stands for the carrier photo-generation with a given spin,  $\tau_0$ , is the optical recombination time,  $\tau_B$  characterizes the coherent spin relaxation in the bulk and  $\tau_B^{flip}$  the relaxation with spin-flip. The intralevel spin relaxation processes in the bulk are characterized by the time  $\tau_s$ . Additionally, the resonant and non-resonant carrier transfer assisted by phonons from the bulk states to the wetting layer is driven by the terms proportional to  $\Pi^{\pm}$  and  $1/\tau_{nr}$ , respectively. The impurity levels have been introduced as intermediaries in the relaxation process of confined carriers in the wetting layer with density  $n_i^{\pm}$ , where  $\tau_{cw}$  stands for the coherent spin relaxation from the wetting layer excited levels, while  $\tau_e$  is the relaxation towards the ground state. In this case, the time for intralevel spin relaxation processes is determined by  $\tau_{si}$ .

As described in Ref. [69], the spin relaxation at low temperatures (when phonon absorption is still depressed) is determined by the spin-orbit interaction, boosted by the

spatial anisotropy produced by confinement profiles intertwined with the momentum scattering with impurities. The spin occupation of these excited impurity states can be tuned according to the polarization of the incoming photons. The optical spin pumping in semiconductor nanostructures [71, 72] has proven to be a tool to probe the effects of localization and spin-orbit interaction mechanisms that tune the spin lifetime. In our case, the Fermi distribution,  $f_{FD}(E_{n_i^\pm}, \mu) = \left( \exp\left(\frac{E_{n_i^\pm} - \mu}{k_B T}\right) + 1 \right)^{-1}$ , characterizes the spin occupation in impurity levels ruling the spin-flipping relaxation in these states. This occupation is mainly determined by the initial optical excitation and we assume that it is not subjected to dynamic changes. As we shall see, this process will trigger a spin-bottleneck [73, 74] under certain excitation conditions. We also assume a linear energy dependence with the occupation density  $n_i^\pm$ , namely  $E_i^\pm = \alpha n_i^\pm$ .

In turn, the function

$$f(x) = \begin{cases} \exp\left(-\frac{x}{k_B T}\right); & x \geq 0 \\ 1. & \end{cases} \quad (3.6)$$

rules the intralevel spin-relaxation in the bulk with lifetime,  $\tau_s$ .

By varying the polarization configurations of the excitation photons, a counter-intuitive effect emerges. The spin coherence appears to be potentiated or depressed if the illumination is performed with either linear or circular polarization, respectively. One would assume that by exciting spins with well defined polarization, the coherence would be enhanced, however this is not the case as shown in Figure 3.3. We will be able to reproduce these effects in the sections below by introducing the mediation of dark impurities states in the spin-relaxation as explained below.

## 3.2 Magneto Absorption

Firstly, we approach theoretically the photo-generation and the magneto-phonon relaxation process. The carrier photo-generation,  $P^\pm$ , in the presence of a magnetic field in the bulk, is ruled by the optical interband absorption of photons with energy  $h\omega$  between 3D Landau levels. It can be considered proportional to the magneto-absorption coefficient which shows resonant spikes when the photon energy matches the inter-Landau level energies as seen in Figure 3.5(a) for GaAs. Thus, the photo generation

has the next form

$$P^\pm(\hbar\omega) \propto \frac{|ep_{cv}^\pm|^2 B}{\hbar\omega} \sum_N \frac{\sqrt{\sqrt{F^\pm(N)^2 + \delta^2} + F^\pm(N)}}{\sqrt{F^\pm(N) + \delta^2}}, \quad (3.7)$$

being  $|ep_{cv}^\pm|$  the optical transition matrix element,  $\delta$  a vanishing life-time energy broadening, and  $F^\pm(N) = \hbar\omega - (E_c^\pm(N) - E_v^\pm(N))$ , where,  $E_c^\pm(N) - E_v^\pm(N)$ , is the energy difference between Landau levels,  $N$ , in the conduction and valence band with a given spin.

The spikes in Figure 3.5(a) however are drastically reduced at higher energies, an effect that can be ascribed to the magneto-polaron enhancement of the Landau energy broadening [15]. To illustrate this, in Figure 3.5(b), two values of  $\delta$  were used to show the change in the absorption coefficient as the energy and magnetic field increases. We can see that the carrier time-life controls the shape of  $P^\pm$ , as expected from Figure 3.5(a). The inset shows the contour plot of the absorption coefficient versus magnetic field and incident photon energy. Since our interest is the high energy region, we used the value of  $\delta = 5$  meV.

While in the bulk the photo-generation is given by equation (3.7) the phonon induced relaxation from 3D to the 2D Landau levels is characterized by the next transition rate

$$\Pi_{res}^\pm \propto \sum_N |\langle 2D|H_p|3D \rangle|^2 \delta(E_{exc}^\pm(N) - E_{WL}^\pm(N) - \hbar\omega_{LO}), \quad (3.8)$$

being  $\langle 2D|H_p|3D \rangle$  the phonon interaction matrix element,  $E_{exc}(N) = E_v^\pm(N) + \hbar\omega$ , the energy of the photo-excited carriers, and,  $E_{WL}(N)$ , the energy of the confined Landau levels in the wetting layer.

The electronic structure of the valence band can be obtained by simplifying the Luttinger Hamiltonian as [41, 75, 76]

$$\begin{bmatrix} s \frac{\gamma_1 + \gamma_2}{2} [2(N-2) + 1] & s \sqrt{3} \frac{\gamma_1 + \gamma_3}{2} \sqrt{N(N-1)} \\ + s \frac{3}{2} \left( \kappa + \frac{9}{4} q \right) - E & \\ & s \frac{\gamma_1 - \gamma_2}{2} [2N + 1] \\ & - s \frac{1}{2} \left( \kappa + \frac{1}{4} q \right) - E \end{bmatrix} \begin{bmatrix} \left| \frac{3}{2}, +\frac{3}{2} \right\rangle |N-2\rangle \\ \left| \frac{3}{2}, -\frac{1}{2} \right\rangle |N\rangle \end{bmatrix} = 0 \quad (3.9)$$

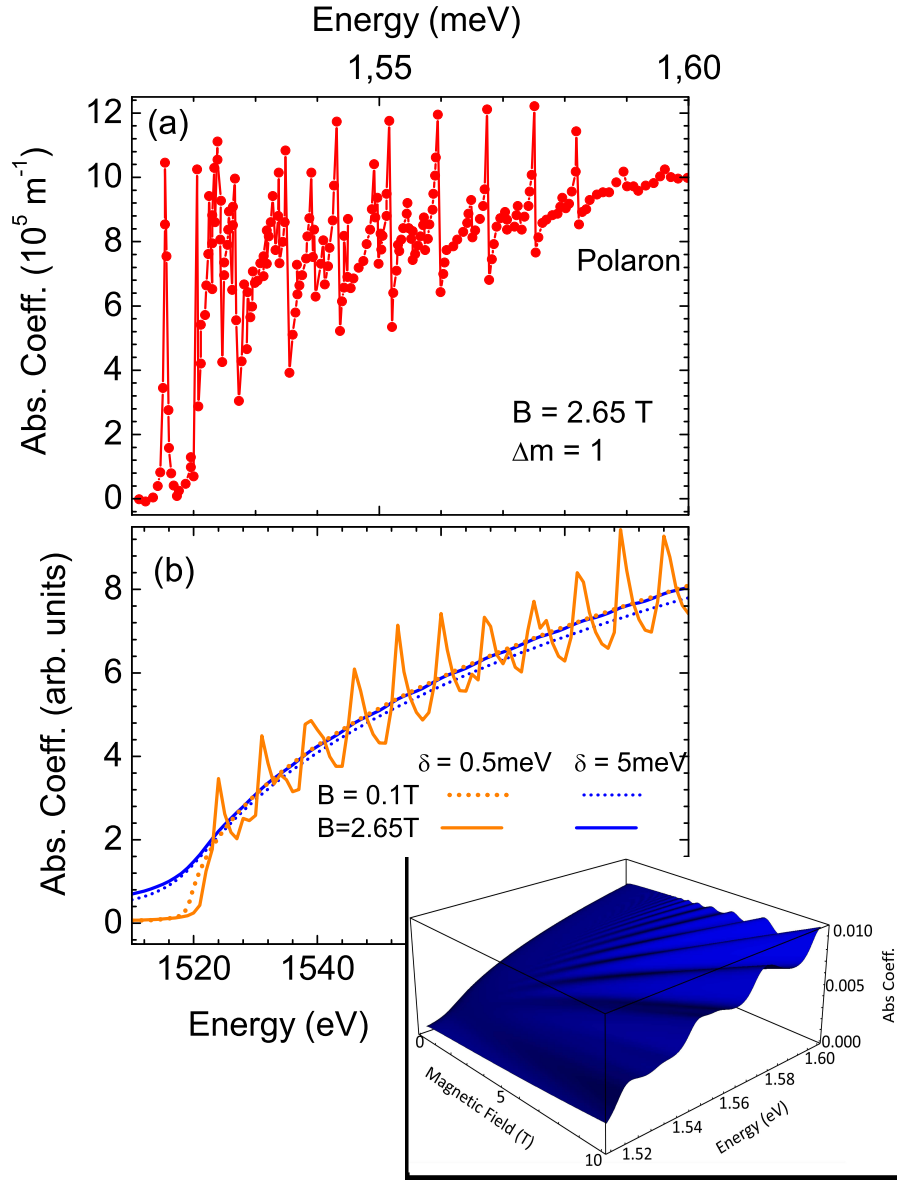


**Figure 3.5:** (a) Experimental absorption coefficient in bulk GaAs as a function of the incident photon energy for  $B = 2.65$  T and circular polarization (Courtesy of experimental collaborators at the Max Planck Institute, Stuttgart). (b) Calculated photo-generation rate according to equation (3.7) in the same conditions as in panel (a). The inset shows a 3D plot of the absorption coefficient vs.  $B$  and incident photon energy.

$$\begin{bmatrix}
 s \frac{\gamma_1 - \gamma_2}{2} [2(N-2) + 1] & s \sqrt{3} \frac{\gamma_1 + \gamma_3}{2} \sqrt{N(N-1)} \\
 + s \frac{1}{2} \left( \kappa + \frac{1}{4}q \right) - E & \\
 & s \frac{\gamma_1 + \gamma_2}{2} [2N + 1] \\
 & - s \frac{3}{2} \left( \kappa + \frac{9}{4}q \right) - E
 \end{bmatrix}
 \begin{bmatrix}
 \left| \frac{3}{2}, +\frac{1}{2} \right\rangle |N-2\rangle \\
 \left| \frac{3}{2}, -\frac{3}{2} \right\rangle |N\rangle
 \end{bmatrix}
 = 0 \quad (3.10)$$

where  $\gamma_1, \gamma_2, \gamma_3, \kappa, q$ , are the Luttinger parameters, and  $s = -\hbar eB/m_0c$ .

In turn, the Landau levels in the conduction band can be simulated within the parabolic approximation as

$$E_c^\pm = E_g^f + \hbar \frac{eB}{m_e c} \left( N + \frac{1}{2} \right) \pm \frac{1}{2} g \mu_B B. \quad (3.11)$$

All the electronic structure parameters depend on the local composition.

Considering for simplicity  $\tau_B^{flip} = \tau_B$  and  $\tau_s \rightarrow \infty$ , the occupation  $\frac{n_0^\pm}{\tau_0}$  is shown in Figure 3.6. Here we used the expression for the photo-generation in equation (3.7) with  $\delta = 5.0$  meV and the phonon assisted transition rate in equation (3.8) has been solved by transforming the Delta function into a Lorentzian with a fixed broadening, 0.03 meV. We are aware that this is a simplification of the actual level broadening that may show a dependence on  $B$  and the Landau level index,  $N$ .

Several excitation conditions can be simulated from our calculations of bulk emission, Figure 3.6, and quantum dot emission, Figure 3.7. In Figure 3.6(a), the results of either  $P^+$  or  $P^-$  incidences, that lead to the spin selective absorption, have been compared. The shifted dips in these two cases correspond to the positions of the resonant phonon assisted electron transfer from the bulk (3D Landau levels) towards the wetting layer which has been considered to be spin-coherent. In turn, for a linearly polarized incidence that can be set as a combination of the two circularly polarized excitations, the result corresponds to the curve displayed in Figure 3.6(b) which is identical for both detections,  $n_0^+$  or  $n_0^-$ .

The corresponding result for the emission from the wetting layer ground state is shown in Figure 3.7. Contrary to the results in Figure 3.6(a) for  $n_0^\pm$ , under circularly polarized excitation, the spectra in Figure 3.7(a) change according to its sign but do not vary with respect to the detection of either  $n_{WL0}^+$  or  $n_{WL0}^-$ . Yet, in the case of linearly polarized absorption, the dynamics of the spin injected to the wetting layer ground state changes since there is interference of spin-bottleneck, that now plays a role. We can see that, under linearly polarized incidence, when both  $P^+ \neq 0$  and  $P^- \neq 0$  simultaneously, the wetting layer emission spectrum becomes then dependent on the way it is detected, be it  $n_{WL0}^+$  or  $n_{WL0}^-$ , as unveiled in Figure 3.7 (b).

However, the occupation of the ground state Landau levels affects the carrier relaxation. This would correspond to the assumption of the existence of a quasi-Fermi level,  $E_F$ ,

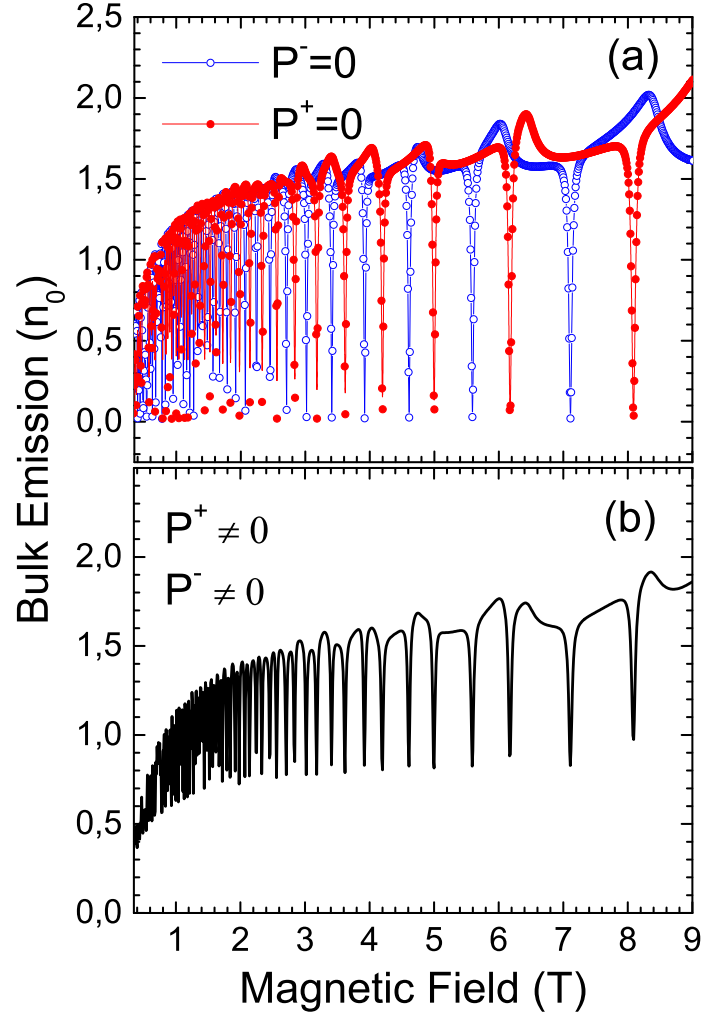


**Figure 3.6:** Calculated values of  $n_0^\pm$  considering  $\tau_B^{flip} = \tau_B$  and  $\tau_s \rightarrow \infty$ : (a) simulation of the circularly polarized excitation (different for either  $n_0^+$  or  $n_0^-$  detection). (b) simulation of the linearly polarized excitation, identical for both detection  $n_0^+$  and  $n_0^-$ .

in the bulk, so that the relaxation rate  $1/\tau_B$  should be replaced by  $[1 - f_{FD}(n_0^\pm)]/\tau_B$  in equations (3.1) and (3.2). In this case, the stationary problem cannot longer be solved analytically.

To determine  $E_F$ , we are going to use as energy reference the value for  $B = 0$  in the conduction band. The relation between the 3D electron density,  $n_{3D}$  and the density of states in the limit  $T \rightarrow 0$  is  $n_{3D} = \int_0^{e_{N,j}} \rho(E) dE$ . In this way, the following implicit equation for  $e_{N,j}$  is obtained [77]

$$\frac{n_{3D}}{\Omega B} = \sum_{i=0}^N \sum_{k=0}^j \left[ e_{N,j} - \hbar\omega_c \left( N + \frac{1}{2} \right) - \frac{2k-1}{2} g\mu_B B \right]^{\frac{1}{2}} \quad (3.12)$$

with  $\Omega = \frac{e}{2\pi^2 ch^2} \sqrt{m}$ ,  $N = 0, 1, \dots$ , and  $j = 0, 1$ . The corresponding Fermi level va-

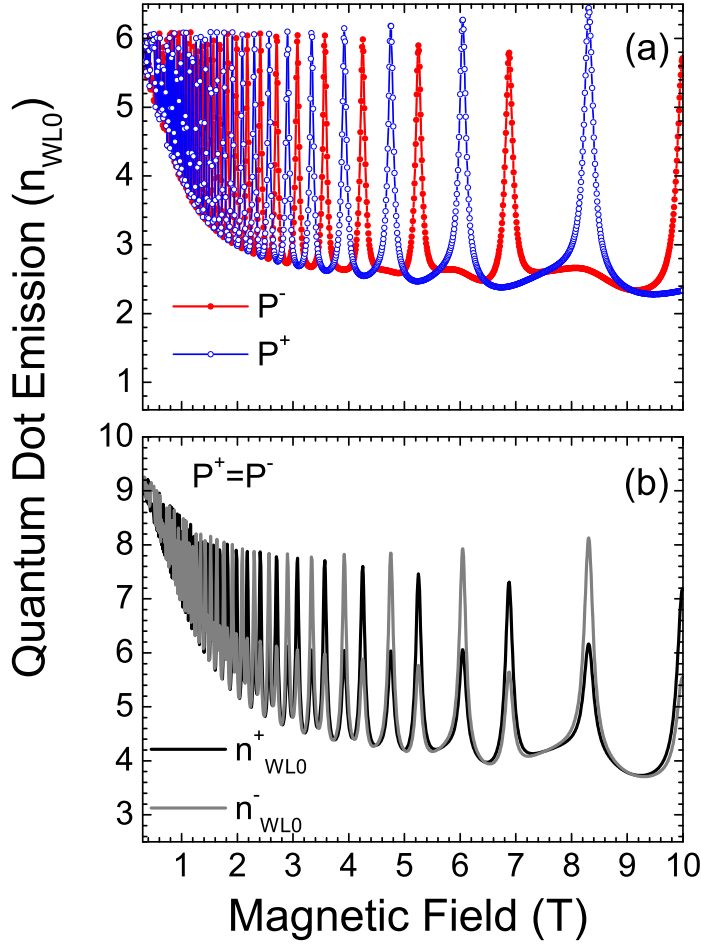


**Figure 3.7:** Calculated values of  $n_{WL0}^{\pm} \tau_B^{flip} = \tau_B$  and  $\tau_s \rightarrow \infty$ : (a) simulation of the circularly polarized excitation. (b) simulation of the linearly polarized excitation, different for either  $n_{WL0}^+$  or  $n_{WL0}^-$  detection in both polarization configurations.

values at certain magnetic field  $B$  for a given  $n_{3D}$  can be expressed as  $E_F(B, n_{3D}) = \perp\{e_{0,0}(B), e_{0,1}(B), \dots, e_{N,j}(B), \dots\}$ , where  $\perp\{\dots\}$  stands for the bottom value of the given sequence.

As the density of states grows with  $B$  (left panel of Figure 3.8), the ground state relative occupation shrinks enhancing the chances for the carrier relaxation. We can consider  $\Pi^{\pm} = 0$  and change  $1/\tau_B$  by  $[1 - f_{FD}(n_0^{\pm})]/\tau_B$  in equations (3.1) to assess the relative effect of this occupation. This is shown in the right panel of Figure 3.8 where the occupations  $n_{exc}$  and  $n_0$  are plotted for  $\hbar\omega = 1579$  meV. We can see that the occupation of the ground state Landau level act as envelop curves for the final relaxation process.

In order to understand the phonon assisted transition effects, we solve the set of equa-



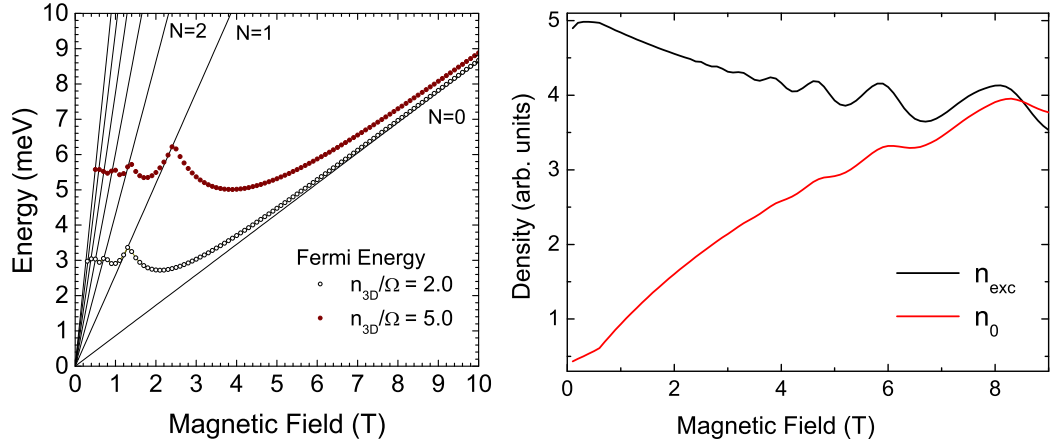


**Figure 3.8:** Left: First conduction band Landau levels in bulk GaAs and Fermi energy as a function of the magnetic field for two values of  $n_{3D}/\Omega B$ . Right: Occupation of  $n_{exc}$  and  $n_0$  considering the modulation of the occupation of the ground state with magnetic field

tions (3.1)-(3.5) including the transition rate (3.8), where delta functions were assumed to be given by Lorentzian with broadening independent of Landau level. The table 3.1 shows the parameters considered in this work.

**Table 3.1:** Fitting parameters used in these simulations

Parameter	Symbol	value
Recombination time	$\tau_0$	1
Relaxation time in bulk	$\tau_B$	0.7
Relaxation flip time in bulk	$\tau_B^{flip}$	0.9
Time for Non resonant process	$\tau_{nr}$	0.5
Relaxation time in wetting layer	$\tau_{cw}$	0.3
Relaxation time in impurity level	$\tau_e$	0.1
Intralevel Relaxation in bulk	$\tau_s$	3
Intralevel Relaxation in impurity level	$\tau_{si}$	0.03
Proportionality constant	$\alpha$	1 meV
Chemical potential in Impurity level	$\mu$	$10^{-2}$ meV
Temperature	$T$	4 K
Broadening energy	$\delta$	5 meV

The corresponding results for bulk and quantum dot emission are plotted in Figure 3.9, for linear polarization, and in Figure 3.10, for circular polarization excitations.

From these results the initial questions about the influence of the 2D confinement

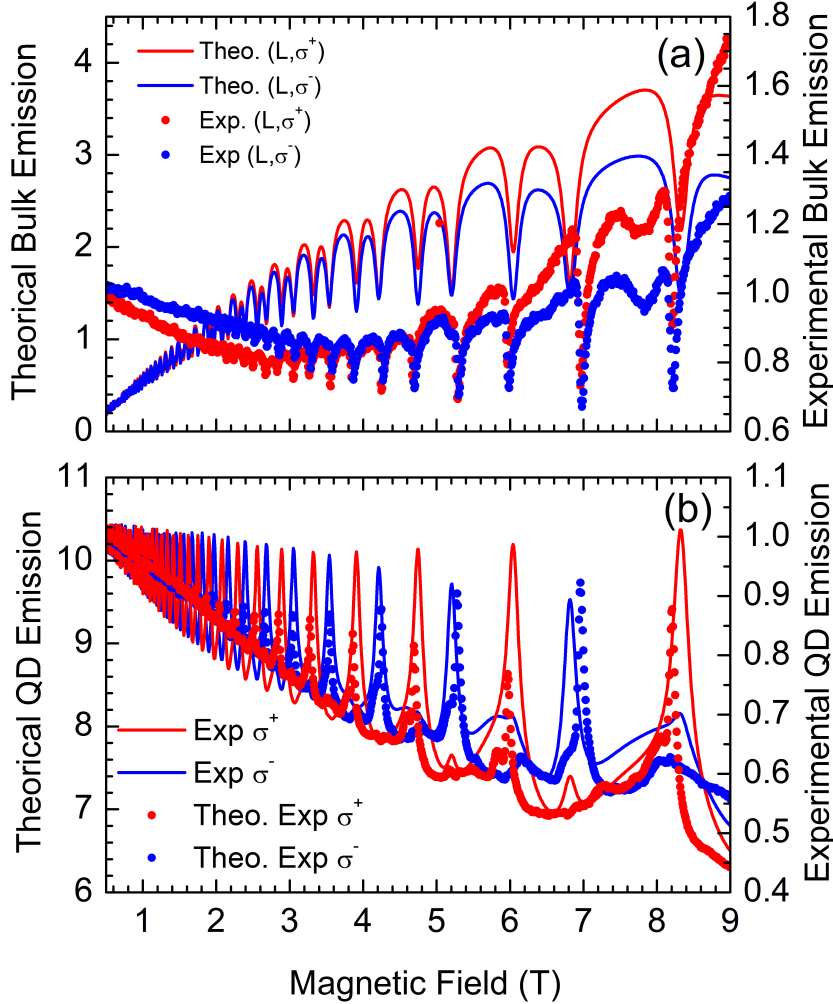


**Figure 3.9:** Comparison between experimental data (points) and theoretical calculations (line) of the emission from (a) bulk and (b) quantum dot. The phonon channel was open and resonant effects can be simulated for  $n_0^-$  and  $n_{WL0}^-$  under linear excitation conditions.

as a communicator between bulk and quantum dot states as well as the assistance of phonons in this communication can be satisfactory answered due to the agreement of theoretical simulations with experimental results. The theoretical assumptions were derived from the consideration of the magneto-resonance triggered by phonons in the 2D landau levels and the occupation present in a wetting layer.

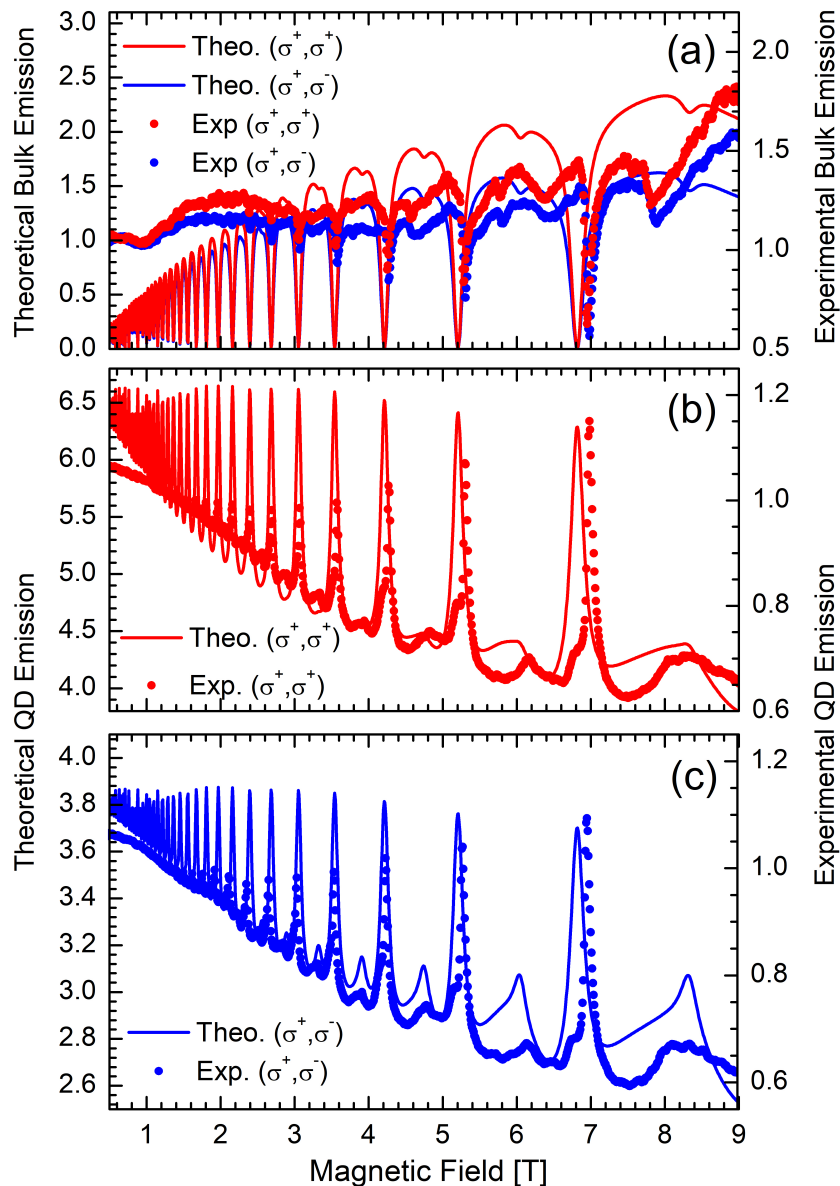


**Figure 3.10:** Comparison between experimental data (points) and theoretical calculations (line) of emission from (a) bulk and (b)-(c) quantum dot. The phonon channel was open and resonant effects can be simulated for both  $\sigma^+$  and  $\sigma^-$  under  $\sigma^+$  excitation.

### 3.3 Spin Decoherence

Another relevant question raised was *how to evaluate quantitatively and qualitatively the effectiveness of the spin-flip blocking in the impurity states?* since the theoretical emissions of quantum dot follows the behaviour in the impurities levels. Thus, to describe the effect of the intermediary donor levels in the spin coherence we can isolate

the equation (3.4) and analyze it under the stationary condition

$$\begin{aligned} 0 &= \frac{n_{WL}^+}{\tau_{cw}} f_{FD}(E_{n_i^+}, \mu) - \frac{n_i^+}{\tau_e} + \frac{n_i^-}{\tau_{si}} f_{FD}(E_{n_i^+}, \mu) - \frac{n_i^+}{\tau_{si}} f_{FD}(E_{n_i^-}, \mu), \\ 0 &= \frac{n_{WL}^-}{\tau_{cw}} f_{FD}(E_{n_i^-}, \mu) - \frac{n_i^-}{\tau_e} + \frac{n_i^+}{\tau_{si}} f_{FD}(E_{n_i^-}, \mu) - \frac{n_i^-}{\tau_{si}} f_{FD}(E_{n_i^+}, \mu), \end{aligned} \quad (3.13)$$

This dynamics is responsible for controlling the spin relaxation and coherence towards the ground state. As highlighted before, the spin coherence of the relaxation dynamics can be controlled by the nature of the polarization of the light used for the excitation. According to the experimental evidence, the spin-flip terms can, in principle be inhibited under the incidence of linearly polarized light, leading to the potentiation of spin coherent channels. In turn, the spin coherence is suppressed under circularly polarized light when, in principle, the spins polarization would be expected to be well defined. We thought that an effective way to do that was to assess the relative difference between the spin densities calculated with and without the activation of spin-flip channel, proportional to  $1/\tau_{si}$ . Thus, we introduced the quantity that we labeled as Relative Decoherence

$$RD^\pm = \frac{n_i^\pm - n_i^\pm (\tau_{si}/\tau_e \rightarrow \infty)}{n_i^\pm (\tau_{si}/\tau_e \rightarrow \infty)}. \quad (3.14)$$

In the limit  $\tau_{si}/\tau_e \rightarrow \infty$ , the effect of the spin-flip channels is nulled and  $RD$  weights their relative influence in the sense that if  $RD \rightarrow 0$  it would mean that the spin-flip channels are not active leading to a totally spin coherent relaxation path.

We can calculate the Relative Decoherence as a function of the in-coming spin polarization from the wetting layer defined as

$$DP^0 = \frac{n_{WL}^+ - n_{WL}^-}{n_{WL}^+ + n_{WL}^-}, \quad (3.15)$$

that will be essentially reproduced by the nature of the polarization of the incident photons. Then, by taking

$$n_{WL}^- = n_{WL}^+ \frac{1 - DP^0}{1 + DP^0}, \quad (3.16)$$

and fixing  $n_{WL}^+ = n_0$  we have calculated the Relative Decoherence as shown in Figure 3.11. In the limit of low densities  $n_0$ , the solution of equation (3.14) provides the maximum absolute values for the decoherence given by

$$RD_{max}^\pm = -\frac{2}{2 + \tau_{si}/\tau_e} \frac{DP^0}{1 + DP^0}, \quad (3.17)$$

and this function has also been plotted in Figure 3.11.

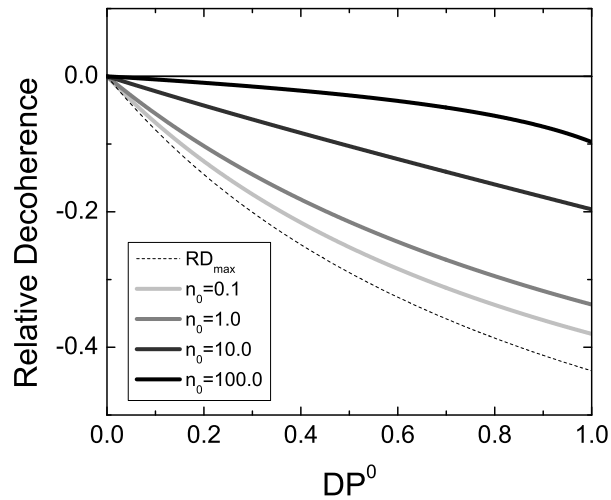


**Figure 3.11:** Calculated Relative Decoherence as a function of the incoming spin polarization (or degree of circular polarization of the incoming photons).

Note that for higher densities, the relative decoherence starts to vanish, thus depressing the spin-flip channels. Also, within the whole range of densities,  $RD \rightarrow 0$  for lower  $DP^0$  and this is the case of linear polarized incidence, when both spins polarizations are equally excited. As the degree of polarization enhances, the absolute values of the relative decoherence grows indicating the activation of the spin-flips. This explains the peculiar spin filtering effect that was highlighted in Figure 3.3 and completes the picture that characterizes the peculiar experimental observations described previously.



# Chapter 4

## Electron Dynamics in 2D Semiconductors Layers

In this chapter, we are interested in relating the theoretical results of scattering theory in two dimensions with a quantity easily measured in experiments of electro-optical transport of quasi two dimensional devices. We propose to use the phase shift method in order to characterize the conductivity through a bi-dimensional system locally perturbed which is tuned by external light. It is the way we can see how the scattering theory, besides of being a fundamental part in quantum mechanics, helps us to obtain information on the microscopic structure of quantum systems and acts as a bridge to allow us to do an association between objects and the quantum laws in order to form a mental picture of the interaction scheme.

We will focus on thin two dimensional crystals of transition metal dichalcogenides (TMDs). These films are especially attractive for optoelectronic devices due to the high mobility at room temperature, flexibility, and high material quality, convenient features for the realization of new generation of 2D storage devices, emitters, light detectors and solar cells [78–82]. The composition of the transition metal dichalcogenides crystals is  $MX_2$ , where  $M$  designates the transition metal atom and  $X$  the chalcogen species (see Figure 4.1 adapted from [83]). The interlayer bonding takes place through weak van der Waals forces which allows scaling down each layer by means of several techniques until the monolayer form. A way to tune the carrier response in this kind of systems is by applying local stress or local electrostatic potentials (gates) in order to induce

carrier confinement. The use of these TMDs as thin film switches has clear advantages, moreover, if compared to analogous bulk semiconductor devices which are rigid, heavy in weight and demanding high cost technology to process, the thin crystals such as  $MoS_2$  and  $WSe_2$  have become very attractive alternatives holding the promise to open possibilities of new optoelectronics architectures [82, 84, 85].

				13 IIIA 3A	14 IVA 4A	15 VA 5A	16 VIA 6A
				5 B Boron 10.811	6 C Carbon 12.011	7 N Nitrogen 14.00674	8 O Oxygen 15.9994
				13 Al Aluminum 26.981539	14 Si Silicon 28.0855	15 P Phosphorus 30.973762	16 S Sulfur 32.066
4 IVB 4B	5 VB 5B	6 VIB 6B	7 VIIB 7B	31 Ga Gallium 69.732	32 Ge Germanium 72.64	33 As Arsenic 74.92159	34 Se Selenium 78.96
22 Ti Titanium 47.88	23 V Vanadium 50.9415	24 Cr Chromium 51.9961	25 Mn Manganese 54.938	49 In Indium 114.818	50 Sn Tin 118.71	51 Sb Antimony 121.760	52 Te Tellurium 127.6
40 Zr Zirconium 91.224	41 Nb Niobium 92.90638	42 Mo Molybdenum 95.94	43 Tc Technetium 98.9072				
72 Hf Hafnium 178.49	73 Ta Tantalum 180.9479	74 W Tungsten 183.85	75 Re Rhenium 186.207				

TMD

**Figure 4.1:** Transition Metal Dichalcogenide, TMD, has chemical composition  $MX_2$  (where  $M$  is a transition metal and  $X = S, Se$  or  $Te$ ). Analogous to the graphene structure, TMD's monolayers have hexagonal lattice structures, but a direct band gap, unlike graphene, at  $K$  and  $K'$  points of the hexagonal Brillouin zone)

Of particular interest for us is the molybdenum disulfide,  $MoS_2$ , due to the direct band gap at the monolayer form as well as photoluminescence and electro-luminescence in the visible range up to room temperature [86, 87]. Furthermore, the strong valley polarization and high-in-plane mobility are promising features for the development of valleytronics and integrated circuit technologies [88, 89] as well as flexible and transparent transistor devices, for low-power and high efficiency biological and chemical sensing applications [90].

In these TMDs the electronic properties are affected by the substrate used changing, for instance, the doping level [91, 92]. Here, we are performing the characterization of



transport process on photo-gated  $MoS_2$  thin films with functionalized substrate using photochromic molecules [84]. Although experimentally challenging, this is no longer a future perspective but a plausible realization nowadays [93] and can be achieved by placing the exfoliated crystal on top of photochromic self-assembled azobenzene molecules, thus being able to control the potential profile and its topography by optical means [23].

A brief development of two dimensional scattering theory will be presented in this chapter. After that, we find the solutions for the equation of motion that, later, meet the scattering solution, in such a way that boundary conditions are always satisfied. By using these solutions, we emulate the dynamics of electrons within a monolayer being locally perturbed. The features are characterized in terms of the scattering phase shifts, which will enable the computation of the differential scattering cross section dependence with controllable parameters. Another objective of this chapter is attained applying the scattering theory for both Schrödinger and Dirac equation simultaneously. A discussion about the conditions when it is possible to use a parabolic or linear dispersion relation ends this chapter by contrasting asymptotic limits of momenta.

## 4.1 Scattering Theory in Two Dimensions

A  $MoS_2$  monolayer is almost a two dimensional system. The monolayer deposition over a functionalized substrate will create an electronic cloud deformation which may induce the emergence of attractive or repulsive scattering centers of  $MoS_2$  [23, 94]. Azobenzene molecules (AZO) have the property to switch between trans and cis isomers in a process called photo-isomerization. Both trans and cis configurations are achieved through illumination with UV and the process could be reversed by using white light. Juan Li et al in Ref.93 report photoluminescence measurements performed on  $MoS_2$  monolayers placed over photoswitchable azobenzene molecules as substrate. When the  $MoS_2$  nanosheet is in contact with the AZO-trans configuration it is presumable a n-type doping. The cis configuration lowers the doping, quenching the side band and enhancing the overall photoluminescence efficiency by a factor of 3.

In the following, the  $MoS_2$  topographic structure will be assumed as a two dimensional system, the perturbation caused by the AZO-cis and AZO-trans isomers will by mod-

eled as a quantum well as showed in Figure 4.2(a) and a quantum barrier potential as showed in Figure 4.2(b).

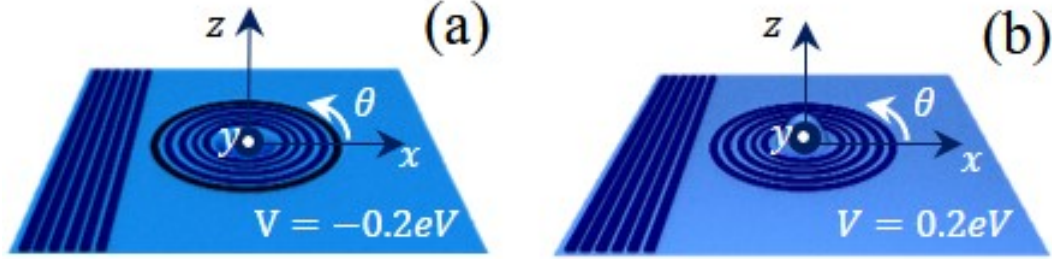


**Figure 4.2:** An incident plane wave front will strike a target that produces scattered waves expanding in all directions. The target could be a well (a) or a barrier (b).

Furthermore, we consider a single scattering center in the system, placed at the origin of coordinates and described by a short range potential. In this way, if  $V(\mathbf{r})$  vanishes at some point, let say  $L$ , the eigenfunctions in the region  $V(\mathbf{r}) = 0$  are plane wave states. The time-independent Schrödinger equation is

$$H\psi = \left( -\frac{\hbar^2 \nabla^2}{2m_e} + V(\mathbf{r}) \right) \psi = E\psi \quad (4.1)$$

or

$$[\nabla^2 + \tilde{k}^2] \psi = \frac{2m_e}{\hbar^2} V(\mathbf{r}) \psi \quad (4.2)$$

where

$$\tilde{k}^2 = \frac{2m_e E}{\hbar^2}. \quad (4.3)$$

The equation (4.2) is similar to the Helmholtz equation when it has a delta function source, and its solution is given by the Green function  $G(\mathbf{r})$  [95]

$$[\nabla^2 + \tilde{k}^2] G(\mathbf{r} - \mathbf{r}') = \frac{2m_e}{\hbar^2} \delta(\mathbf{r} - \mathbf{r}'). \quad (4.4)$$

Taking advantage of this, we will express  $\psi$  as

$$\psi(\mathbf{r}) = e^{i\tilde{\mathbf{k}} \cdot \mathbf{r}} + \int d^2 \mathbf{r}' G(\mathbf{r} - \mathbf{r}') V(\mathbf{r}') \psi(\mathbf{r}'), \quad (4.5)$$

and it is easy to verify that this satisfies the Schrödinger equation (4.2). Now the  $G(\mathbf{r} - \mathbf{r}')$  has to be determined for a two dimensional case. At  $\mathbf{r} - \mathbf{r}' \neq 0$  we have a free

particle equation and their solutions are a linear combination of first  $J_m$  and second kind  $Y_m$  Bessel functions,

$$H_m^{(1,2)} = J_m(\tilde{k}r) \pm iY_m(\tilde{k}r). \quad (4.6)$$

This formulation is known as Hankel function of the first and second kind and are used to express outgoing and incoming waves depending on the sign convention for the frequency.

From here, we assume that  $V(\mathbf{r})$  is cylindrically symmetric and hence depends only on the magnitude of  $\mathbf{r}$  and, for short,  $\mathbf{r} - \mathbf{r}' \equiv \mathbf{R}$ . The symmetrical solution, assumed to have the form  $G(R) = CH_0^1$ , can be put into (4.2) and integrating over  $d\theta$  we get

$$2\pi \left( \frac{1}{R} \frac{d}{dR} \left( R \frac{d}{dR} \right) + \tilde{k}^2 \right) CH_0^1(\tilde{k}R) = \frac{2\pi}{\pi} \frac{2m_e}{\hbar^2} \frac{\delta(R)}{R} \quad (4.7)$$

$$\left( \frac{d}{dR} R \frac{d}{dR} + R\tilde{k}^2 \right) CH_0^1(\tilde{k}R) = \frac{2m_e}{\pi\hbar^2} \delta(R). \quad (4.8)$$

Then, integrating this equation from 0 to  $\epsilon$  and taking the limit  $\epsilon \rightarrow 0$

$$\lim_{\epsilon \rightarrow 0} \int_0^\epsilon dR \left( \frac{d}{dR} R \frac{d}{dR} + R\tilde{k}^2 \right) CH_0^1(\tilde{k}R) = \lim_{\epsilon \rightarrow 0} \int_0^\epsilon dR \frac{2m_e}{\pi\hbar^2} \delta(R) \quad (4.9)$$

$$\lim_{\epsilon \rightarrow 0} \left( \epsilon \frac{d}{d\epsilon} CH_0^1(\tilde{k}\epsilon) \right) = \frac{2m_e}{\pi\hbar^2} \quad (4.10)$$

$$\lim_{\epsilon \rightarrow 0} C \epsilon \frac{d}{d\epsilon} \left( J_0(\tilde{k}\epsilon) + iY_0(\tilde{k}\epsilon) \right) = \frac{2m_e}{\pi\hbar^2} \quad (4.11)$$

$$\lim_{\epsilon \rightarrow 0} C \epsilon \frac{d}{d\epsilon} i \frac{2}{\pi} \left( \log \left( \frac{\tilde{k}\epsilon}{2} \right) - \gamma \right) = \frac{2m_e}{\pi\hbar^2} \quad (4.12)$$

$$\lim_{\epsilon \rightarrow 0} C \epsilon i \frac{2}{\pi} \left( \frac{\tilde{k}}{\tilde{k}\epsilon} \right) = \frac{2m_e}{\pi\hbar^2} \quad (4.13)$$

$$C = -i \frac{m_e}{\hbar^2} \quad (4.14)$$

and

$$G(R) = -i \frac{m_e}{\hbar^2} H_0^1(\tilde{k}R). \quad (4.15)$$

The integral in (4.5) extends over the range of  $V(\mathbf{r})$  which decays to zero outside some finite region. In a typical scattering problem, measurements are realized at points far

away from the scattering center. For large arguments  $H_0^1(z) \rightarrow \sqrt{\frac{2}{\pi z}} e^{iz}$  and (4.5) takes the form

$$\psi(\tilde{\mathbf{k}}, \mathbf{r}) = e^{i\tilde{\mathbf{k}} \cdot \mathbf{r}} + f(\tilde{k}) \frac{e^{i\tilde{k}r}}{\sqrt{r}}, \quad (4.16)$$

with

$$f(\tilde{k}) = -\frac{m_e}{\hbar^2} \sqrt{\frac{i}{2\pi\tilde{k}}} \int d^2r' e^{-i\tilde{\mathbf{k}} \cdot \mathbf{r}'} V(r') \psi(r'). \quad (4.17)$$

Both terms on the right of (4.16) have the exponent of outgoing waves. The first one is a plane wave without any information about the potential, while the second term represents one leaving the target with a scattering amplitude  $f(\tilde{k})$ . A schematic representation of this phenomenon is shown in Figure 4.2.

## 4.2 Scattering Phase Shift

Here we will describe one method to find the scattering amplitude  $f(\theta)$  in order to get the differential scattering cross section. For this, firstly we need to solve the equation of motion for a particle in the presence of a central potential  $V(r)$ , and after that the phase shift method would be applied to calculate the scattering amplitude.

### 4.2.1 Dirac Case

Following the idea of the scattering problem of massive particles, a construction of the scattered wave function (4.16) using the mathematical equation that governs the electronic structure in TMDs is presented here.

The Hamiltonian for transition metal dichalcogenides monolayers is [89]

$$H_D = at(\tau q_x \sigma_x + q_y \sigma_y) + \frac{\Delta}{2} \sigma_z - \tau \lambda \frac{\sigma_z - 1}{2} s_z, \quad (4.18)$$

where  $a$  is the lattice constant,  $t$  is the effective hopping integral,  $\tau = \pm 1$  is the valley index,  $\sigma_i$  the Pauli matrices that act in the spinor space corresponding to the two orbitals of atoms in a hexagonal lattice,  $\Delta$  the energy gap,  $2\lambda$  the spin-orbit splitting at the valence band, and  $s_z$  is the Pauli matrix. The spinors are wave functions of two components referring to the two orbitals in the hexagonal structure.

The valleys  $K$  and  $K'$  of the Brillouin zone are uncoupled and it is possible to consider the scattering problem at each valley independently [96]. Thus we are going to focus on the  $K$  valley and consider spin up, i. e.  $\tau = 1$  and  $s_z = 1$

$$H_D = \begin{pmatrix} \Delta/2 & atq_- \\ atq_+ & -\Delta/2 + \lambda \end{pmatrix}, \quad (4.19)$$

where  $q_{\pm} = q_x \pm iq_y$  and add a scattering center  $V$  as follows

$$V(\mathbf{r}) = \begin{cases} V, & \text{for } r \leq L, \\ 0 & \text{for } r > L. \end{cases} \quad (4.20)$$

This system has axial symmetry and, as it is well known, such central potential problem conserves angular momentum. Therefore we may choose simultaneously eigenfunctions to the Dirac-like Hamiltonian  $H = H_D + V$  and the  $z$  component of the total angular momentum operator  $\mathbf{J} = \mathbf{l}_z + \frac{1}{2}\boldsymbol{\sigma}_z + \frac{1}{2}\mathbf{s}_z$  where  $\mathbf{l}_z = -i\frac{\partial}{\partial\phi}$  is the  $z$  component of the orbital angular momentum. We assume that

$$H\psi = \begin{pmatrix} \Delta/2 + V & atq_- \\ atq_+ & -\Delta/2 + \lambda + V \end{pmatrix} \begin{pmatrix} \psi_a e^{im\theta} \\ \psi_b e^{i(m+1)\theta} \end{pmatrix} \quad (4.21)$$

where  $m \in \text{integer}$  (for details see appendix C for state  $\psi_{j=m+1}$ ). Thereby, to get the radial part of  $\psi$  we use a cylindrical coordinate system, in which  $q_{\pm} = -ie^{\pm i\theta}(\partial_r \pm i/r\partial_{\theta})$  [97] and solve the following set of differential equations

$$\left(\frac{\Delta}{2} + V\right)\psi_a - iat\left(\partial_r + \frac{m+1}{r}\right)\gamma\psi_b = E\psi_a \quad (4.22)$$

$$\left(\frac{-\Delta}{2} + \lambda + V\right)\gamma\psi_b - iat\left(\partial_r - \frac{m}{r}\right)\psi_a = E\gamma\psi_b. \quad (4.23)$$

After some manipulation, we uncouple the  $\psi_a$  and  $\psi_b$  components. For  $\psi_a$  we have

$$\left(\rho^2 \frac{d^2}{d\rho^2} + \rho \frac{d}{d\rho} + (\rho^2 - m^2)\right)\psi_a = 0 \quad (4.24)$$

where  $\rho = qr$  and

$$q = \frac{1}{at} \sqrt{(E - V)^2 - \lambda(E - V) - \frac{\Delta}{2} \left(\frac{\Delta}{2} - \lambda\right)}, \quad (4.25)$$

is the wave vector inside.

The solutions for equation (4.24) are the cylindrical Bessel functions of the first kind,  $J_m$ , and second kind  $Y_m$  [57]. The asymptotic behavior of these two Bessel functions is given by [57],

$$J_m(z) = \begin{cases} \frac{1}{m!} \left(\frac{z}{2}\right)^m, & \text{for } z \rightarrow 0 \\ \sqrt{\frac{2}{\pi z}} \cos\left(z - \frac{1}{2}\pi\left(m + \frac{1}{2}\right)\right), & \text{for } z \rightarrow \infty \end{cases} \quad (4.26)$$

$$Y_m(z) = \begin{cases} \frac{2}{\pi} \left(\ln \frac{z}{2} + \gamma\right), & \text{for } m = 0 \text{ and } z \rightarrow 0 \\ -\frac{(m-1)!}{\pi} \left(\frac{2}{z}\right)^m, & \text{for } m \neq 0 \text{ and } z \rightarrow 0 \\ \sqrt{\frac{2}{\pi z}} \sin\left(z - \frac{1}{2}\pi\left(m + \frac{1}{2}\right)\right), & \text{for } z \rightarrow \infty \end{cases} \quad (4.27)$$

but some requirements should be satisfied. In the potential region, the wave function must be a normalizable solution, while outside this region, a linear combination of incoming and outgoing waves is expected.

For this reason, at  $0 \leq r \leq L$ , our solution  $\psi_m^i$  is

$$\psi_m^i = N_m \begin{pmatrix} J_m(qr)e^{im\theta} \\ \frac{-iatq}{-\Delta/2+\lambda-(E-V)} J_{m+1}(qr)e^{i(m+1)\theta} \end{pmatrix}, \quad (4.28)$$

where  $N_m$  is a normalization constant.

On the other hand, at  $r \geq L$ ,  $\psi_m^o$  is a combination of the first,  $H_m^1(\tilde{q}r)$ , and second kind,  $H_m^2(\tilde{q}r)$ , of Hankel functions, equation (4.6), and the solution  $\psi_o$  is

$$\psi_m^o = \begin{pmatrix} N_1 H_m^2(\tilde{q}r) + N_2 e^{2i\delta_m} H_m^1(\tilde{q}r) \\ \frac{-iat\tilde{q}}{-\Delta/2+\lambda-E} \left(N_1 H_{m+1}^2(\tilde{q}r) + N_2 e^{2i\delta_m} H_{m+1}^1(\tilde{q}r)\right) e^{i\theta} \end{pmatrix} e^{im\theta} \quad (4.29)$$

with

$$\tilde{q} = \frac{1}{at} \sqrt{E^2 - \lambda E - \frac{\Delta}{2} \left(\frac{\Delta}{2} - \lambda\right)}, \quad (4.30)$$

the wave vector outside and  $N_{1,2}$  are normalization constants. The phase shift  $e^{2i\delta_m}$  depends on the parameters of the potential  $V(r)$ . Because of this, the phase of the outgoing wave function is shifted with respect to the incoming wave, determining the elastic scattering problem.

We are looking for solutions,  $\psi$ , satisfying simultaneously the following equations

$$(H_D + V(\mathbf{r}))\psi = E\psi, \quad (4.31)$$

$$\psi_{r \rightarrow \infty}^{\rightarrow} = \begin{pmatrix} 1 \\ \frac{-i\alpha t \tilde{q}}{-\Delta/2 + \lambda - E} \end{pmatrix} e^{i\tilde{\mathbf{q}} \cdot \mathbf{r}} + f(\tilde{q}, \theta) \begin{pmatrix} 1 \\ \frac{-i\alpha t \tilde{q}}{-\Delta/2 + \lambda - E} e^{i\theta} \end{pmatrix} \frac{e^{i\tilde{q}r}}{\sqrt{r}}, \quad (4.32)$$

such that an eventual wave decomposition allows us to characterize the asymptotic behavior of each partial wave. This method is used to compute the scattering amplitude and cross section, since the influence of the scalar potential is manifested by deflections of the incident wave when it reaches the potential.

After some manipulation (see appendix C for details), the function outside the potential region takes the form

$$\psi_m^o = \begin{pmatrix} \left( J_m(\tilde{q}r) + \frac{e^{2i\delta_m} - 1}{2} H_m^1(\tilde{q}r) \right) \\ \frac{-i\alpha t \tilde{q}}{-\Delta/2 + \lambda - E} \left( J_{m+1}(\tilde{q}r) + \frac{e^{2i\delta_m} - 1}{2} H_{m+1}^1(\tilde{q}r) \right) e^{i\theta} \end{pmatrix} e^{im(\theta + \frac{\pi}{2})}, \quad (4.33)$$

where the normalization constant  $N_m$  and the phase shift  $\delta_m$  are determined from the boundary condition  $\psi_m^i|_L = \psi_m^o|_L$ . We found

$$N_m = e^{i\frac{\pi}{2}m} \left( \frac{J_m(\tilde{q}L)}{J_m(qL)} - \frac{e^{2i\delta_m} - 1}{2} \frac{H_m^1(\tilde{q}L)}{J_m(qL)} \right), \quad (4.34)$$

$$e^{2i\delta_m} = \frac{H_{m+1}^{(2)}(\tilde{q}L)J_m(qL) - DH_m^{(2)}(\tilde{q}L)J_{m+1}(qL)}{DH_m^{(1)}(\tilde{q}L)J_{m+1}(qL) - H_{m+1}^{(1)}(\tilde{q}L)J_m(qL)}, \quad (4.35)$$

with  $D = \frac{-\Delta/2 + \lambda - E}{-\Delta/2 + \lambda - (E - V)} \frac{q}{\tilde{q}}$ .

In order to recognize the scattering amplitude generated by the potential,  $V$ , we will use the Jacobi-Anger identity [57],

$$e^{i\tilde{\mathbf{q}} \cdot \mathbf{r}} = \sum_{m=-\infty}^{\infty} C_m i^m J_m(\tilde{k}r) e^{im\theta}, \quad (4.36)$$

and the asymptotic form of Hankel functions [57]

$$H_m^{(1,2)}(z) = J_m(z) \pm iY_m(z) \Big|_{z \rightarrow \infty} = \sqrt{\frac{2}{\pi z}} e^{\pm i(z - \pi/2(m+1/2))}, \quad (4.37)$$

$$\psi = \sum_{m=-\infty}^{\infty} \psi_m^o = \sum_{m=-\infty}^{\infty} \begin{pmatrix} J_m(\tilde{q}r) + \frac{e^{2i\delta_m} - 1}{2} H_m^1(\tilde{q}r) \\ \frac{-i\alpha t \tilde{q}}{-\Delta/2 + \lambda - E} \left( J_{m+1}(\tilde{q}r) + \frac{e^{2i\delta_m} - 1}{2} H_{m+1}^1(\tilde{q}r) \right) e^{i\theta} \end{pmatrix} e^{im(\theta + \frac{\pi}{2})} \quad (4.38)$$

where in  $r \rightarrow \infty$  limit, we have

$$\psi_{(r \rightarrow \infty)}^{\rightarrow} = e^{i\tilde{\mathbf{q}} \cdot \mathbf{r}} \begin{pmatrix} 1 \\ \frac{-\alpha t \tilde{q}}{-\Delta/2 + \lambda - E} \end{pmatrix} + \sum_{m=-\infty}^{\infty} \frac{e^{2i\delta_m} - 1}{2} \sqrt{\frac{2}{i\pi \tilde{q}}} e^{im\theta} \begin{pmatrix} 1 \\ \frac{-\alpha t \tilde{q}}{-\Delta/2 + \lambda - E} e^{i\theta} \end{pmatrix} \frac{e^{\tilde{q}r}}{\sqrt{r}}, \quad (4.39)$$

and comparing with the state  $\psi$  in the equation (4.16)

$$\psi = e^{i\tilde{q}\cdot\mathbf{r}} \begin{pmatrix} 1 \\ \frac{-at\tilde{q}}{-\Delta/2+\lambda-E} \end{pmatrix} + f(\tilde{q}, \theta) \begin{pmatrix} 1 \\ \frac{-at\tilde{q}}{-\Delta/2+\lambda-E} e^{i\theta} \end{pmatrix} \frac{e^{i\tilde{q}r}}{\sqrt{r}} \quad (4.40)$$

where the scattering amplitude  $f(\tilde{q}, \theta)$  of the wave function, which describes the scattering problem, is

$$f(\tilde{q}, \theta) = \sum_{m=-\infty}^{\infty} \frac{e^{2i\delta_m} - 1}{2} \sqrt{\frac{2}{i\pi\tilde{q}}} e^{im\theta}. \quad (4.41)$$

The quantity  $f(\tilde{q}, \theta)$  measures the scattered part of the outgoing wave. By obtaining the phase shift,  $\delta_m$ , gained after the scattering process, it is possible to find the scattering amplitude.

Thus, since the phase shift describes completely the collision process in a theoretical way, we will summarize the procedure to obtain this information: 1) solve the eigenproblem  $H\psi = E\psi$  (equation (4.21)), allowing both free and scattered solutions for the outside region; 2) calculate the asymptotic limit of the solution and compare it with the solution of the scattering problem (equation (4.32)); 3) identify the scattering amplitude  $f$  and use the boundary conditions to calculate the phase shifts  $\delta_m$ .

Our task now consists in obtaining the scattering amplitude by varying different parameters such as depth or width of the potential in order to describe the transport response in these TMDs systems. Additionally, we will investigate in which limit the parabolic approximation for the Hamiltonian is still valid for obtaining a reasonable description of the locally perturbed TMDs monolayers. The last point is interesting since the Schrödinger equation remains as the natural theoretical way to describe the quantum effects in the semiconductor field.

### 4.2.2 Parabolic Approximation: Schrödinger Case

For very low wave vectors, one reasonable approximation for the electronic structure of TMDs should be to assume a parabolic dispersion [98]. Such an assumption could be obtained from equation (4.30), where we have

$$E(\tilde{q}) = \frac{\lambda}{2} \pm \sqrt{\left(\frac{\lambda - \Delta}{2}\right)^2 + (at\tilde{q})^2}, \quad (4.42)$$



assuming  $\Delta > \lambda$

$$E(\tilde{q} \rightarrow 0) \approx \begin{cases} \frac{\Delta}{2} + \frac{(at)^2 \tilde{q}^2}{\Delta - \lambda}, \\ -\frac{\Delta}{2} + \lambda - \frac{(at)^2 \tilde{q}^2}{\Delta - \lambda}, \end{cases} \quad (4.43)$$

or, defining  $at = \hbar v_f$

$$E \approx \frac{\hbar^2 \tilde{q}^2}{2m_e}, \quad (4.44)$$

where  $m_e^{-1} = \pm \frac{2v_f^2}{\Delta - \lambda}$  is the effective mass for electrons (+) or holes (-).

In the limit of small  $\tilde{q}$ , the carriers are describe as Schrödinger fermions and the scattering problem will be solve using a parabolic Hamiltonian with a given effective mass. Essentially, for carriers ruled by dispersion relation (4.2.2), the system remains the same, with a scattering potential as described before

$$V(\mathbf{r}) = \begin{cases} V, & \text{for } r \leq L, \\ 0 & \text{for } r > L. \end{cases} \quad (4.45)$$

we recover the discussion about axial symmetry, and hence polar coordinates  $(r, \theta)$  are still more convenient. The equation for a stationary state  $\psi$  reads,

$$\left( \frac{-\hbar^2}{2m_e} \left( \frac{\partial^2}{\partial r^2} + \frac{1}{r} \frac{\partial}{\partial r} + \frac{1}{r^2} \frac{\partial^2}{\partial \theta^2} \right) + V(\mathbf{r}) \right) \psi = E\psi, \quad (4.46)$$

such that the solution can be written as the product of a radial and an angular parts  $\psi(r, \theta) = R(r)\Theta(\theta)$ . Putting this into the equation (4.46), dividing by  $R(r)\Theta(\theta)$  and multiplying by  $-2m_e/\hbar^2$ , we obtain the expression

$$r^2 \left( \frac{1}{R} \frac{\partial^2}{\partial r^2} + \frac{1}{R} \frac{1}{r} \frac{\partial}{\partial r} \right) R - \frac{1}{\Theta} \frac{\partial^2 \Theta}{\partial \theta^2} = -r^2(E - V(\mathbf{r})) \frac{2m_e}{\hbar^2}, \quad (4.47)$$

The term in brackets in the left only depends on  $r$ , whereas the remainder depends only on  $\theta$ .

The solution for the angular equation satisfying the imposed boundary condition  $\Theta(\theta) = \Theta(\theta + 2\pi)$  is

$$\Theta(\theta) = \frac{1}{\sqrt{2\pi}} e^{im\theta} \quad (4.48)$$

with  $m = 0, \pm 1, \pm 2 \dots$ , whereas the solution for radial part,  $R(r)$ , is determined by

$$\left( \frac{d^2}{dr^2} + \frac{1}{r} \frac{d}{dr} + \frac{m^2}{r^2} \right) R(r) = -(E - V(\mathbf{r})) \frac{2m_e}{\hbar^2} R(r). \quad (4.49)$$

As our potential is finite, the carriers could get into both classically forbidden or allowed regions, then for  $r < L$  the wave functions are expected to decay or oscillate with a wavelength that depends on the momentum of the particle, let say  $k = \sqrt{(E - V)\frac{2m_e}{\hbar^2}}$ . Outside, the traveling wave function oscillates with  $\tilde{k} = \sqrt{E\frac{2m_e}{\hbar^2}}$ . Using  $L$  as a length scale, the next dimensionless radial equation inside the potential is obtained with  $\rho = kr$ , such that

$$\left( \frac{\partial^2}{\partial \rho^2} + \frac{1}{\rho} \frac{\partial}{\partial \rho} + \frac{m^2}{\rho^2} \right) R = -R. \quad (4.50)$$

As seen before, equation (4.50) is the Bessel's differential equation. The general solution for this case are the cylindrical Bessel functions of first kind,  $J_m$ , and second kind  $Y_m$ . As usual, we have two requirements for the wave function. Inside and outside of the potential region,  $\psi$  must be normalizable and needs to coincide at the boundary. Necessarily, at  $0 \leq r \leq L$  the wave function is

$$\psi_m^i = \sqrt{\frac{1}{2\pi}} N_i e^{im\phi} J_m(kr), \quad (4.51)$$

where  $N_i$  is a normalization constant. On the other hand, at  $r \geq L$  the state must be a combination of  $J_m(\tilde{k}r)$  and  $Y_m(\tilde{k}r)$  and the wave function for the outside region is,

$$\psi_m^o = \sqrt{\frac{1}{2\pi}} N_o e^{im\phi} \left( J_m(\tilde{k}r) \pm iY_m(\tilde{k}r) \right), \quad (4.52)$$

where  $N_o$  is a normalization constant. The boundary condition for  $\psi$  requires that the wave function and its first derivative must be continuous at  $r = L$ , thus the relation between  $N_i$  and  $N_o$  can be obtained,

$$N_o = N_i \frac{J_m(kL)}{J_m(\tilde{k}L) \pm iY_m(\tilde{k}L)}, \quad \text{with} \quad (4.53)$$

$$N_i^2 = \frac{2}{|J_m(kL)|^2 - J_{m-1}(kL)J_{m+1}(kL)}, \quad (4.54)$$

the allowed energies are found numerically using the transcendental equation for  $k$ ,

$$\frac{kJ'_m(kL)}{J_m(kL)} = \frac{\tilde{k}(J'_m(\tilde{k}L) \pm iY'_m(\tilde{k}L))}{J_m(\tilde{k}L) \pm iY_m(\tilde{k}L)}. \quad (4.55)$$

In order to satisfy simultaneously

$$\left( \frac{-\hbar^2}{2m_e} \nabla^2 + V(\mathbf{r}) \right) \psi = E\psi, \quad (4.56)$$

$$\psi_{r \rightarrow \infty} \vec{\rightarrow} = e^{i\tilde{\mathbf{k}} \cdot \mathbf{r}} + f(\tilde{k}, \theta) \frac{e^{i\tilde{k}r}}{\sqrt{r}}, \quad (4.57)$$

we follow a process similar to the one described in the previous section,

$$\psi_m^o = \frac{1}{2} \left[ H_m^{(2)}(\tilde{k}r) + e^{2i\delta_m} H_m^{(1)}(\tilde{k}r) \right] \cos(m\theta) \quad (4.58)$$

$$= J_m(\tilde{k}r) \cos(m\theta) + \frac{e^{2i\delta_m} - 1}{2} \cos(m\theta) H_m^{(1)}(\tilde{k}r) \quad (4.59)$$

where the term  $e^{2i\delta_m}$  is expected to arise from the interaction with the potential, modifying the initial wave phase by an amount  $\delta_m$ .

$$\psi = \sum_{m=0}^{\infty} C_m \iota^m \psi_m^o \quad (4.60)$$

$$= e^{i\tilde{\mathbf{k}} \cdot \mathbf{r}} + \sum_{m=0}^{\infty} C_m \iota^m \frac{e^{2i\delta_m} - 1}{2} \cos(m\theta) H_m^{(1)}(\tilde{k}r), \quad (4.61)$$

where the Jacobi-Anger identity in equation (4.36) was used,  $C_0 = 1$ , and all the other  $C_m = 2$ . From the asymptotic form of  $\psi$ , it is possible to identify the scattering amplitude in equation (4.16)

$$f(\tilde{k}, \theta) = \sum_{m=0}^{\infty} C_m \sqrt{\frac{2}{i\pi\tilde{k}}} \frac{e^{2i\delta_m} - 1}{2} \cos(m\theta), \quad (4.62)$$

and

$$\psi = e^{i\tilde{\mathbf{k}} \cdot \mathbf{r}} + \sum_{m=0}^{\infty} C_m \sqrt{\frac{2}{i\pi\tilde{k}}} \frac{e^{2i\delta_m} - 1}{2} \cos(m\theta) \frac{e^{i\tilde{k}r}}{\sqrt{r}}. \quad (4.63)$$

The appropriate form of each separated solution  $m$  comes from boundary conditions

$$N_i k J'_m(kL) = \frac{1}{2} \tilde{k} \left[ H_m^{(2)}(\tilde{k}L) + e^{2i\delta} H_m^{(1)}(\tilde{k}L) \right], \quad (4.64)$$

where the incident and scattered waves are written in the left and right hand of the above equations, respectively. The phase shift factor can be calculated using these two expressions:

$$e^{2i\delta_m} = \frac{H_m^{(2)}(\tilde{k}L) - B H_m^{(2)}(\tilde{k}L)}{B H_m^{(1)}(\tilde{k}L) - H_m^{(1)}(\tilde{k}L)}, \quad (4.65)$$

where  $B = \frac{k J'_m(kL)}{\tilde{k} J_m(kL)}$ .

Here, it should be noticed that the scattering amplitude in the Schrödinger model differs from the Dirac model through the phase shifts  $\delta_m$  (see equations (4.65) and (4.35)). This would be reflected in the differential cross section

$$\frac{d\sigma}{d\theta} = |f(\theta, \tilde{q})|^2, \quad (4.66)$$

which contains information on the angular distribution of the scattering [99].

### 4.3 Probability Density and Differential Cross Section

As mentioned in the beginning of this chapter, we aim to investigate the effects of a perturbation  $V(r)$  on the TMDs surface. With this characterization we can modify the electronic transport response. In table 4.1, the parameters for different TMDs monolayers are reported and these values were extracted from [89].

**Table 4.1:** Band structure parameters of some transition metal dichalcogenide monolayers from reference [89].

	a [Å]	t [eV]	$\Delta$ [eV]	$2\lambda$ [eV]
<i>MoS<sub>2</sub></i>	3.193	1.10	1.66	0.15
<i>WS<sub>2</sub></i>	3.197	1.37	1.79	0.43
<i>MoSe<sub>2</sub></i>	3.313	0.94	1.47	0.18
<i>WSe<sub>2</sub></i>	3.310	1.19	1.60	0.46

In order to associate the transport response of a carrier moving in a *MoS<sub>2</sub>* monolayer with the photoswitchable states, AZO-trans and AZO-cis, we first plot the probability density of a scattering wave function, given by equation (4.40), in Figure 4.3(a) for well potential and (b), for barrier one. We note a bright area behind the center in contrast to the shadow appearing in the same place for the barrier case. In other words, it is

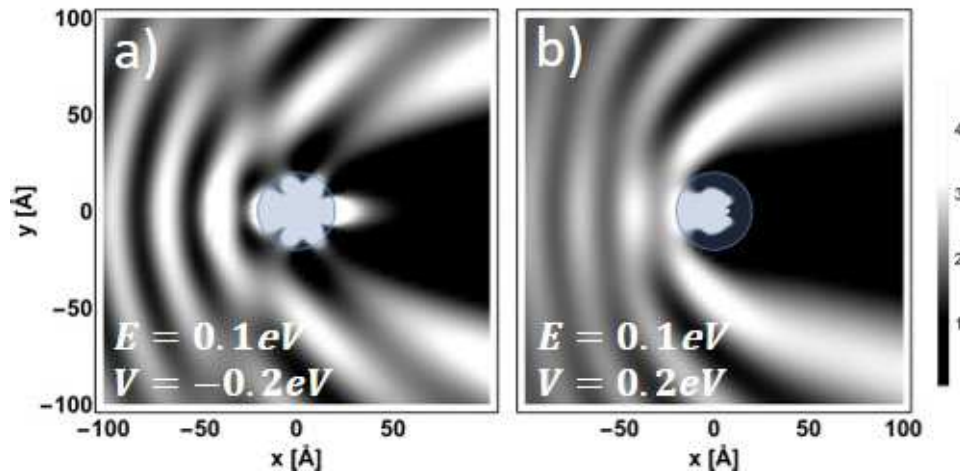


**Figure 4.3:** Probability density of a scattered function found in the case of a (a) well potential, and a (b) barrier potential. Incident flux comes from the left. Potential centered at origin with range  $L = 20\text{\AA}$ . Scattered particles are expected to accumulate in the forward direction of an attractive potential, while a smaller probability to find particles is anticipated in a repulsive interaction case.

more probable to find scattered carriers in forward direction of an attractive potential than for a repulsive one, a relevant feature for possible technological applications.

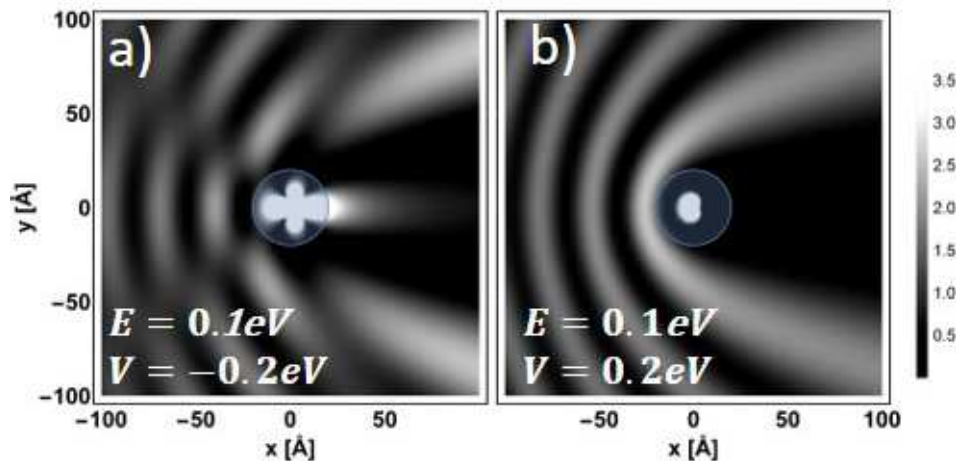


**Figure 4.4:** The same as in Figure 4.3 but using the parabolic mass approximation for carriers.  $L = 20\text{\AA}$ .

Similarly, the probability density for scatter carriers ruled by a parabolic dispersion relation, equation (4.63), is plotted in Figure 4.4(a) for well potential and (b) for barrier.

It is possible to see that both graphics show the same qualitative behavior and, as seen before, the potential size determines different conditions for electronic transport. This is evident from Figure 4.5(a) where, through variations on the potential depth, we see an on-off mechanics in the differential cross section, defined in (4.66). This feature is achieved for distinct incident plane waves fronts, even when we describe carriers as Schrödinger fermions, Figure 4.5(b).

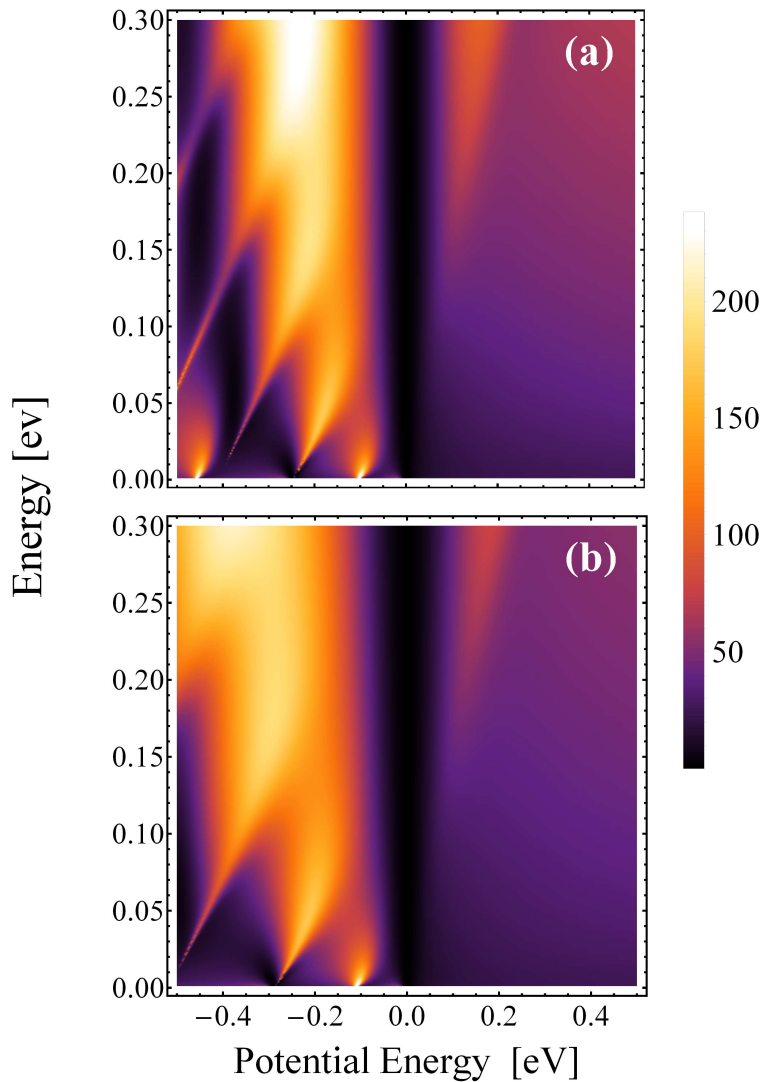


**Figure 4.5:** Differential scattering cross section as a function of the potential range,  $V$ , and the incident wave front energy found using a (a) Dirac-like Hamiltonian, and a (b) parabolic relation dispersion.  $L = 20\text{\AA}$ .

When a potential  $V$  is attractive, one can think of a wave being pulled in by the potential, whereas for a repulsive potential the waves are expected to be pushed out.

In both  $V > 0$  or  $V < 0$  cases, the  $m = 0$  channel is the one which most contributes to the differential cross section.

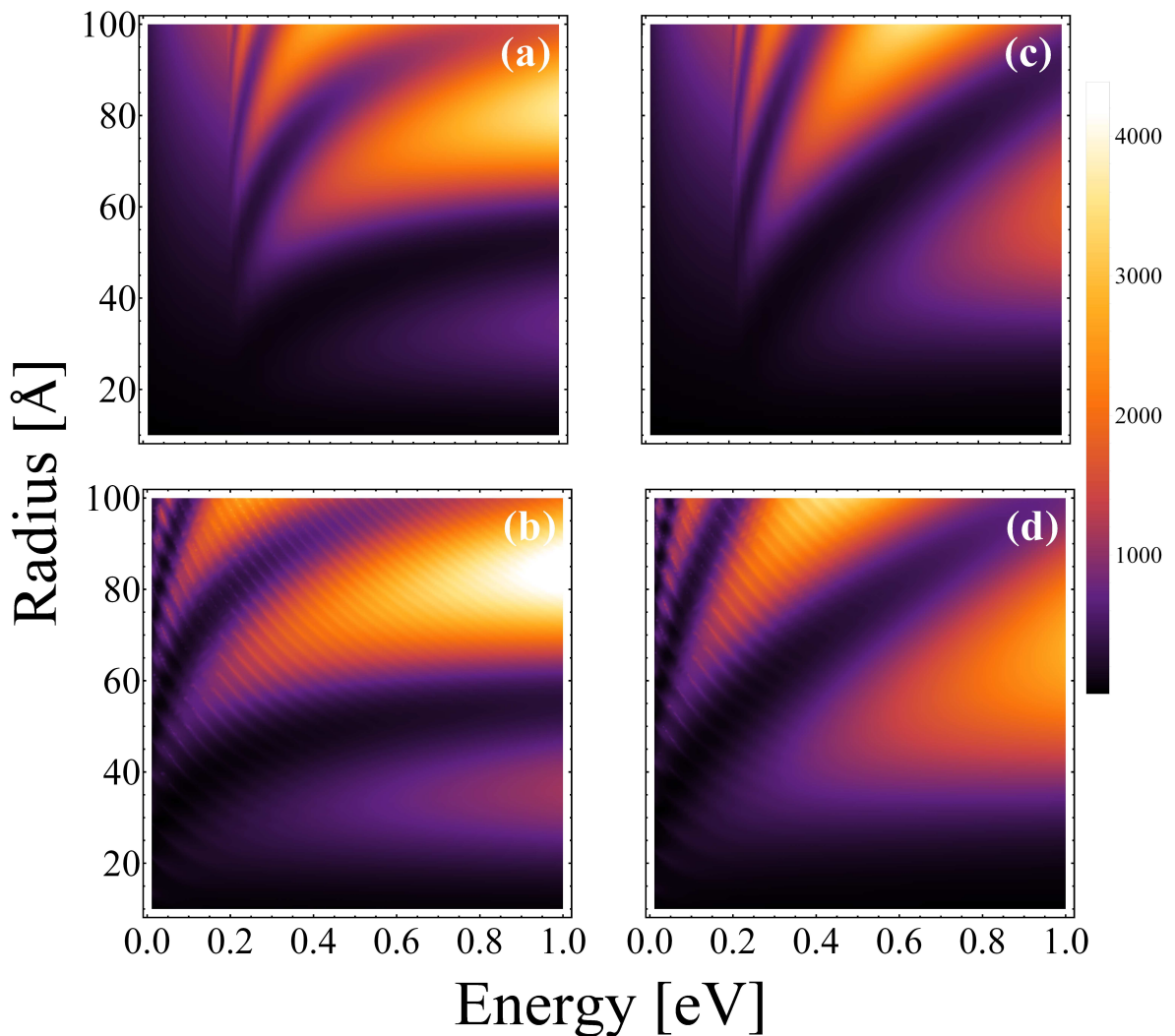


**Figure 4.6:** Differential scattering cross section, calculated from equation (4.41) as a function of the incident energy for four different radius  $L$ .

Until here, we examined the differential cross section for a fixed well width, however, if the local perturbation is expanding (or contracted) the effects will be reflected in the set of partial wave phase shifts, this is shown in Figure 4.6(a) and (b) for carriers ruled by a Dirac-like Hamiltonian. In Figure 4.6(c) and (d), the differential cross section is plotted for the scattering amplitude in equation (4.66) which corresponds to carriers with a parabolic relation dispersion. We complement our understanding about the modifications on the radius,  $L$ , and the modulation of the differential cross section with Figure 4.7 where different radius and its effects over transmissions probability for

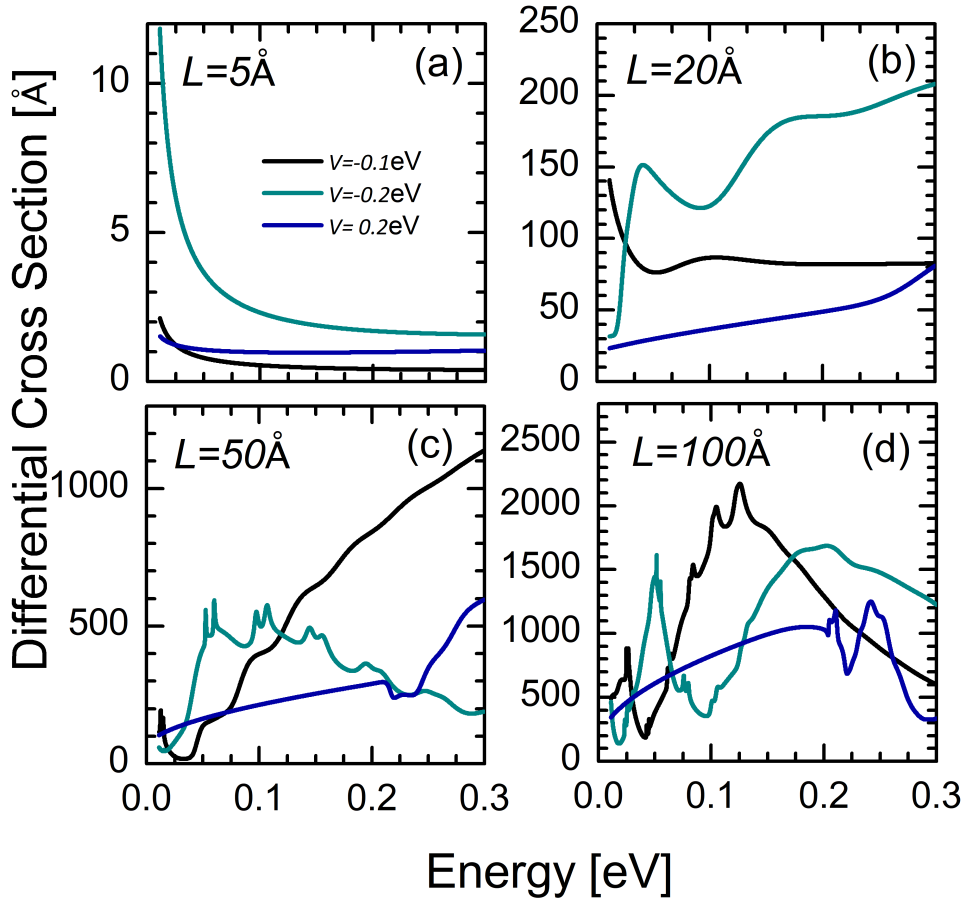


**Figure 4.7:** Differential scattering cross section calculated from equation (4.66) (Results for Dirac-massive formulation) as a function of the incident energy for four different widths  $L =$  (a)  $5\text{\AA}$ , (b)  $20\text{\AA}$ , (c)  $50\text{\AA}$ , (d)  $100\text{\AA}$ . formulation.

wells and barriers are plotted. Figure 4.8 is analogous to Figure 4.7 but considering a parabolic relation dispersion. As the radius increases, the differential cross section from Dirac the case starts to differ more and more from the Schrödinger case.

In Figure 4.9 we plot the difference  $\frac{d\sigma^D}{d\theta} - \frac{d\sigma^S}{d\theta}$  as a function of the detection angle in order to estimate quantitatively the difference on the scattering amplitude between *Dirac scattering amplitude* and a *Schrödinger* one for different momenta of incident carriers. As we see in the upper and lower panel of Figure 4.9, the main difference appears in the forward direction of the scattering center for both positive or negative potentials. For a barrier case, a Dirac-like and Schrödinger-like back scattering is comparable, and the quantity  $\frac{d\sigma^D}{d\theta} - \frac{d\sigma^S}{d\theta}$  is close to zero, this behavior is relevant even within  $(\pi/2, 3\pi/2)$  interval. The negative differential cross section is indicating that the probability of



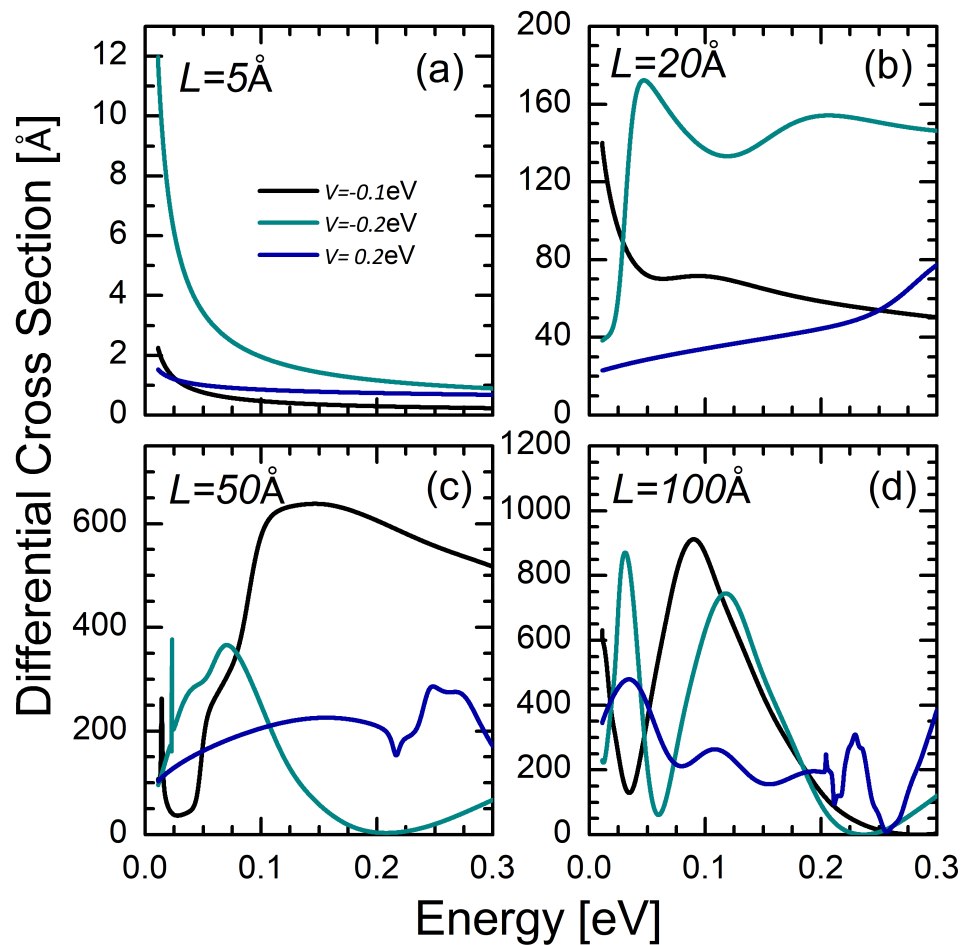


**Figure 4.8:** The same as in Figure 4.7, but using the parabolic mass approximation for carriers, i. e., Schrödinger formulation.

having scattering behind the scattering center is larger if we have Schrödinger-like carriers.

In the lower panel of Figure 4.9 the positive quantity indicates that the scattering of Dirac-like carriers is greater than the scattering of Schrödinger-like carriers. This could be interpreted as carriers hitting TMD's structures would be scattered in more angular directions than those hitting traditional semiconductor systems. Such dissimilar behavior raises the important discussion about the limits and conditions in which a Dirac-like picture of TMD's monolayers is relevant in scattering theory, and allows us to contrast the results for carriers ruled by a parabolic dispersion relation.

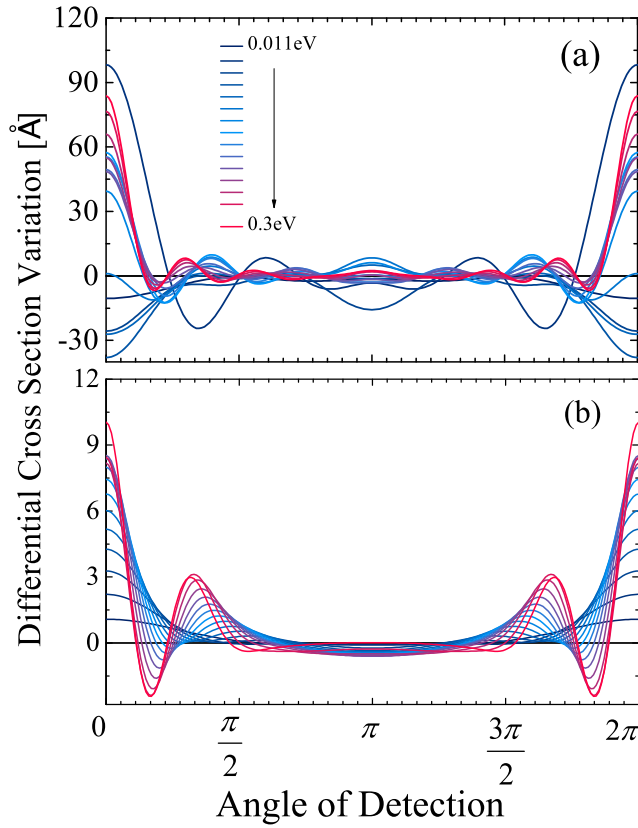


**Figure 4.9:** The difference  $\frac{d\sigma^D}{d\theta} - \frac{d\sigma^S}{d\theta}$  is plotted as a function of the detection angle  $\theta$  for a well with radius  $L = 20\text{\AA}$ .

## 4.4 Asymptotic Analysis

Based on the analytical results for the electronic structure of TMD's films, we proceed to compare asymptotic behaviors of the scattering problem when carriers are described using Dirac formulation and Schrödinger formulation. We make use of the phase shift because this parameter contains the information about the scattering processes and gives us details about the effect of the potential center. In table 4.2 we summarize some results and conventions used for wave vectors and phase shift.

### 4.4.1 Dirac Formulation

First, we study the asymptotic behavior of  $\delta_m$  for large wave vectors, and subsequently, the short wave vectors limit will be investigated as well. A detailed calculation of the results presented here can be found in the Appendix C.

After mathematical manipulation, we transform the phase shift expression, obtained

**Table 4.2:** Notation used for incident and outgoing wave vector as well as the phase shift for each case studied. Inside for  $r < L$ ; outside  $r > L$ .

	Dirac-like fermions	Schrödinger fermions
Wave Vector Inside	$q = \frac{1}{at} \sqrt{(E - V)^2 - \lambda(E - V) - \frac{\Delta}{2} \left( \frac{\Delta}{2} - \lambda \right)}$	$k = \sqrt{(E - V) \frac{2m_e}{\hbar^2}}$
Wave Vector Outside	$\tilde{q} = \frac{1}{at} \sqrt{E^2 - \lambda E - \frac{\Delta}{2} \left( \frac{\Delta}{2} - \lambda \right)}$	$\tilde{k} = \sqrt{E \frac{2m_e}{\hbar^2}}$
Phase Shift	$e^{2i\delta_m} = \frac{H_{m+1}^{(2)}(\tilde{q}L)J_m(qL) - DH_m^{(2)}(\tilde{q}L)J_{m+1}(qL)}{DH_m^{(1)}(\tilde{q}L)J_{m+1}(qL) - H_{m+1}^{(1)}(\tilde{q}L)J_m(qL)}$	$e^{2i\delta_m} = \frac{H_m^{(2)' }(\tilde{k}L) - BH_m^{(2)}(\tilde{k}L)}{BH_m^{(1)}(\tilde{k}L) - H_m^{(1)' }(\tilde{k}L)}$
	$D = \frac{\lambda - \Delta - E}{\lambda - \Delta - (E - V)} \frac{q}{\tilde{q}}$	$B = \frac{k}{\tilde{k}} \frac{J'_m(kL)}{J_m(kL)}$

using the Dirac-like Hamiltonian, from its exponential form (Table 4.2) into a tangent function

$$\tan(\delta_m) = \frac{J_{m+1}(\tilde{q}L)J_m(qL) - DJ_{m+1}(qL)J_m(\tilde{q}L)}{Y_{m+1}(\tilde{q}L)J_m(qL) - DJ_{m+1}(qL)Y_m(\tilde{q}L)} \quad (4.67)$$

where,  $D = \frac{\lambda - \Delta - E}{\lambda - \Delta - (E - V)} \frac{q}{\tilde{q}}$ .

For high energy in the  $\tilde{q}L \rightarrow \infty$  limit,  $D \approx 1$ , and using (4.26) and (4.27) we can rewrite the numerator and denominator of the equation (4.67) as follows

$$J_{m+1}(\tilde{q}L)J_m(qL) - DJ_{m+1}(qL)J_m(\tilde{q}L) \approx \frac{2}{L\pi} \sqrt{\frac{1}{q\tilde{q}}} \sin(\tilde{q} - q)L \quad (4.68)$$

$$Y_{m+1}(\tilde{q}L)J_m(qL) - DJ_{m+1}(qL)Y_m(\tilde{q}L) \approx -\frac{2}{L\pi} \sqrt{\frac{1}{q\tilde{q}}} \cos(\tilde{q} - q)L \quad (4.69)$$

which leads to

$$\tan(\delta_m) \approx -\frac{\sin(\tilde{q} - q)L}{\cos(\tilde{q} - q)L} = -\tan(\tilde{q} - q)L \quad (4.70)$$

$$\delta_m \approx -(\tilde{q} - q)L. \quad (4.71)$$

Note that it is independent of  $m$ . Intuitively, at very high energy limits or very wide potentials,  $q$  and  $\tilde{q}$  are almost the same, therefore the shift with respect to the free

wave should be zero, however the relation dispersion is hyperbolic, and at high energies the wave vector is almost linear in energy. From table 4.2

$$E_{\tilde{q} \rightarrow \infty} \approx \frac{\lambda - \Delta}{2} + at\tilde{q} \left( 1 + \frac{1}{2} \left( \frac{\lambda - \Delta}{2} \right)^2 \frac{1}{a^2 t^2 \tilde{q}^2} \right) \approx at\tilde{q} \quad (4.72)$$

Substituting  $E = at\tilde{q}$  into  $q = \frac{1}{at} \sqrt{(at\tilde{q} - V)^2 - \lambda(at\tilde{q} - V) - \frac{\Delta}{2} \left( \frac{\Delta}{2} - \lambda \right)}$  we have the expression of  $\delta_m$  as

$$\delta_m \approx -\tilde{q}L + \frac{L}{at} at\tilde{q} \left( 1 + \frac{1}{2} \frac{V^2 - 2Vat\tilde{q}}{a^2 t^2 \tilde{q}^2} \right) \quad (4.73)$$

$$\delta_m \approx -\frac{LV}{at} \quad (4.74)$$

$$\lim_{\tilde{q} \rightarrow \infty} \delta_m = -\frac{LV}{at}. \quad (4.75)$$

This result shows an interesting insight since, despite the intuition, incoming electrons will *see* the potential even when moving with very high energies. This means that in a material with an electronic structure ruled by the Dirac Hamiltonian the carriers mobility is affected by the perturbations created over the surface. We will see below this is different in the Schrödinger perturbation.

Now, to analyze the limit of short wave vectors, one should consider that  $J_m(qr)$ , and consequently  $D$ , belong to  $\mathbb{C}$  since, with  $E < V$ , the wave vector inside the barrier is an imaginary number. In this case, the two solutions for Bessel equation are the modified Bessel functions of the first,  $I_s$ , and second,  $K_s$ , kind.  $I_s(x)$  is finite at the origin, while  $K_s(x)$  has a singularity at  $x = 0$ . The modified Bessel functions of the first kind is defined by

$$I_s(x) = i^{-s} J_s(ix). \quad (4.76)$$

Then

$$\tan(\delta_m) = \frac{J_{m+1}(\tilde{q}L)I_m(qL) - D_r I_{m+1}(qL)J_m(\tilde{q}L)}{Y_{m+1}(\tilde{q}L)I_m(qL) - D_r I_{m+1}(qL)Y_m(\tilde{q}L)}, \quad (4.77)$$

where  $D = iD_r$  and  $D_r \in \mathbb{R}$ . Using the corresponding small arguments behavior of  $J_m$ , equation (4.26), and  $Y_m$ , equation (4.27), we have

$$\lim_{\tilde{q} \rightarrow 0} \tan(\delta_m) = \begin{cases} -\frac{\pi m}{m!^2} \left( \frac{\tilde{q}L}{2} \right)^{2m}, & \text{for } m \neq 0, \\ \frac{1}{\frac{2}{\pi} \left( \ln \frac{\tilde{q}L}{2} + \gamma \right)} & \text{for } m = 0. \end{cases} \quad (4.78)$$

The limit in (4.78) shows that the most contributing channel to the scattering process is  $m = 0$ . Hence, just electrons with low angular momentum have to be considered.

#### 4.4.2 Schrödinger Formulation

For parabolic mass carriers with high energies, i. e., high momentum  $\tilde{k}$ , we have the following expression

$$\tan \delta_m = \frac{J'_m(\tilde{k}L) - BJ_m(\tilde{k}L)}{Y'_m(\tilde{k}L) - BY_m(\tilde{k}L)}, \quad (4.79)$$

with  $B = \frac{k J'_m(kL)}{\tilde{k} J_m(kL)}$ .

At  $\lim_{\tilde{k} \rightarrow \infty} \frac{k}{\tilde{k}} = 1$ , and

$$\begin{aligned} \lim_{\tilde{k} \rightarrow \infty} \frac{J'_m(kL)}{J_m(kL)} &= \lim_{\tilde{k} \rightarrow \infty} \frac{J_{m-1}(kL) - J_{m+1}(kL)}{2J_m(kL)} \\ &= -\frac{\sin(kL - \frac{\pi}{2}(m + \frac{1}{2}))}{\cos(kL - \frac{\pi}{2}(m + \frac{1}{2}))} \end{aligned} \quad (4.80)$$

$$\therefore \frac{k J'_m(kL)}{\tilde{k} J_m(kL)} \approx -\frac{\sin(kL - \frac{\pi}{2}(m + \frac{1}{2}))}{\cos(kL - \frac{\pi}{2}(m + \frac{1}{2}))} \quad (4.81)$$

With this, the complete expressions in the numerator and denominator are

$$\begin{aligned} J'_m(\tilde{k}L) - BJ_m(\tilde{k}L) &= \sqrt{\frac{2}{\pi \tilde{k}L}} \left( -\sin \left( \tilde{k}L - \frac{\pi}{2} \left( m + \frac{1}{2} \right) \right) + \right. \\ &\quad \left. \tan \left( kL - \frac{\pi}{2} \left( m + \frac{1}{2} \right) \right) \cos \left( \tilde{k}L - \frac{\pi}{2} \left( m + \frac{1}{2} \right) \right) \right), \end{aligned} \quad (4.82)$$

$$\begin{aligned} Y'_m(\tilde{k}L) - BY_m(\tilde{k}L) &= \sqrt{\frac{2}{\pi \tilde{k}L}} \left( \cos \left( \tilde{k}L - \frac{\pi}{2} \left( m + \frac{1}{2} \right) \right) + \right. \\ &\quad \left. \tan \left( kL - \frac{\pi}{2} \left( m + \frac{1}{2} \right) \right) \sin \left( \tilde{k}L - \frac{\pi}{2} \left( m + \frac{1}{2} \right) \right) \right). \end{aligned} \quad (4.83)$$

Using both expressions into (4.79) we can write explicitly the carrier phase shift for high energy scattering

$$\lim_{\tilde{k} \rightarrow \infty} \tan(\delta_m) \simeq \tan(k - \tilde{k})L \approx -\tan \left( \frac{m_e VL}{\hbar^2 \tilde{k}} \right), \quad (4.84)$$

Which is fairly different from the expression (4.75). We can see that, as the wave vector or energy increases, the carriers will not be scattered by the perturbation.

Now, for the low energy regime, we have  $k = \sqrt{\frac{(E-V) 2m_e}{\hbar^2}} = \iota \sqrt{\frac{(V-E) 2m_e}{\hbar^2}} = \iota k_r$ , then

$$B = \frac{\iota k_r J'_m(\iota k_r L)}{\tilde{k} J_m(\iota k_r L)} \quad (4.85)$$

$$= \frac{k_r I'_m(k_r L)}{\tilde{k} I_m(k_r L)}. \quad (4.86)$$

For short wave vectors

$$\begin{aligned} \lim_{\tilde{k} \rightarrow 0} B &= \frac{k_r I_{m-1}(k_r L) + I_{m+1}(k_r L)}{2\tilde{k} I_m(k_r L)} \\ &\approx \frac{k_r}{2\tilde{k}} \approx \frac{\sqrt{\tilde{V} - \tilde{k}^2}}{2\tilde{k}} \\ &\approx \frac{1}{\tilde{k}} \sqrt{\tilde{V}} \left(1 - \frac{\tilde{k}^2}{2\tilde{V}}\right) \\ &= \frac{\sqrt{\tilde{V}}}{\tilde{k}} - \frac{\tilde{k}}{2\tilde{V}}, \end{aligned} \quad (4.87)$$

where  $\tilde{V} = V \frac{2m_e}{\hbar^2}$ . Using the corresponding small arguments behavior for  $J_m$  and  $Y_m$ , we have

$$\lim_{\tilde{k} \rightarrow 0} \tan(\delta_m) = \begin{cases} -\frac{\pi m}{m!^2} \left(\frac{\tilde{k}L}{2}\right)^{2m}, & \text{for } m \neq 0, \\ \frac{\pi}{2} \frac{1}{\ln \frac{\tilde{k}L}{2} + \gamma} & \text{for } m = 0, \end{cases} \quad (4.88)$$

which fully agree with the expressions for Dirac-like carriers in (4.78). The phase shift of incoming electrons moving with very low momentum goes to zero, and there is no more scattering processes that could take place at this regime. It is also intuitively expected that both approaches will coincide whenever the kinetic energy is much smaller than the Dirac gap.

The differences and similarities between Dirac and Schrödinger formulations found above become more noticeable in a graphic. In Figure 4.10(a) and Figure 4.10(b), we plot the phase shift  $\delta_m$  gained in a scattering process due to a well and a barrier potential respectively. The asymptotic limit for long wave vectors correspond to the expressions (4.75) and (4.84) for Dirac and Schrödinger cases, both are confirmed in Figure 4.10 (a) and (b). It is also possible to see in Figure 4.10 that the expressions (4.78) and (4.88) for low wave number are checked. Solid (Dirac-massive model) and

dashed lines (parabolic-mass Schrödinger model) in Figure 4.10 clearly match in the short wave vectors regime, Figure 4.10(a) for an attractive potential and Figure 4.10(b) for a repulsive one.

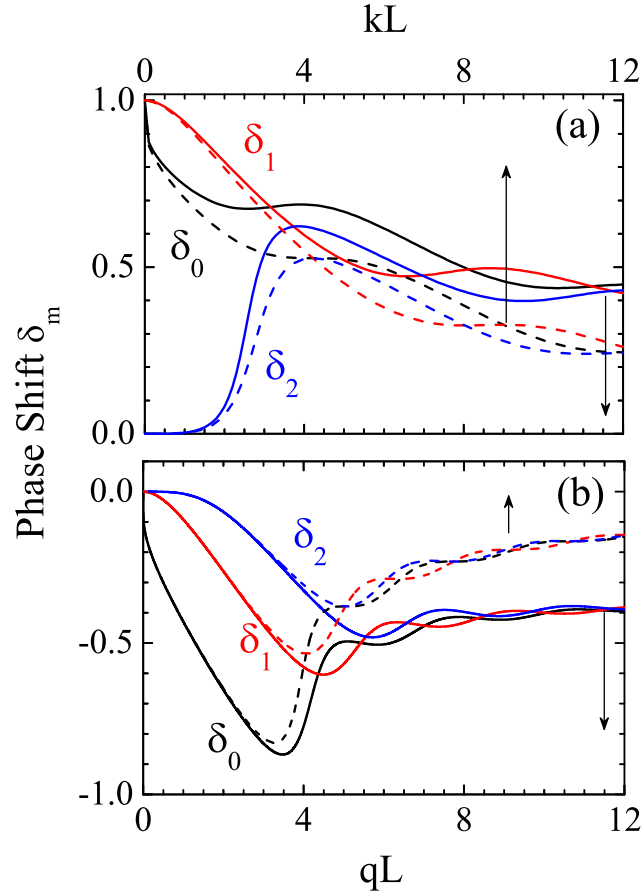


**Figure 4.10:** Phase shift gained during a scattering process due to a: (a) attractive and (b) repulsive potential. The solid lines correspond to Dirac-massive model, whereas dashed lines show the parabolic-mass Schrödinger model. The height and width of the potential are  $|0.2|eV$  and  $20\text{\AA}$  respectively.

We conclude that, at high energies, Dirac-like carriers are subjected to a long range interaction between the carriers and the potential, such that the carriers dynamic will be always affected by it, and all channels are equally scattered by  $V$ . This situation is not observed in the case of Schrödinger-like carriers with high wave vectors. In that limit, they do not see the barrier and they will not be scattered.





# Chapter 5

## Conclusions and Final Considerations

The central concepts that motivated and guided the presented study were the quantum phenomena related to the electronic and optical response of nanoscale 2D systems when they are submitted to local perturbations. An extensive theoretical effort has been made to develop simple models that capture the essential physics behind the operation of the semiconducting nanoelectronic devices and thus allowed us to understand the underlying quantum effects. The main achievements in this Thesis are summarized below:

### **Electronic Structure and Phonons Effects in Quantum Wells**

In quantum wells based in polar semiconductor alloys, both electron-phonon and hole-phonon interactions were considered as perturbations acting on the system. These terms were added into the Luttinger Hamiltonian matrix and then were diagonalized in order to find the renormalized energy. In this study, we use parameters to describe the GaAs-quantum well grown in the (001) plane and in the non-conventional (113). However, the method could be easily extended to other polar semiconductor alloys and for generic [11N] growth directions. It was confirmed from these calculations (chapter 2) that a strong hybridization assisted by Frölich phonons is achieved not only for conduction band states but also for valence band ones. Resonant conditions can be accessed by varying the magnetic field or the length of the well. This tuning turns to be quite important

for optical applications due to the reorganization of the states in both conduction and valence band as revealed in recombination processes. We also prove that the choice of the growth direction is an alternative way to tune the relaxation process in these semiconductor systems.

### **Spin-Resolved Photo-Generation Filtering Induced by Phonon Emission**

The role of two dimensional states in the carrier resonant relaxation process collected in quantum dots embedded in a coupled Bulk/wetting layer/quantum dot system has been unveiled. From a population model for carriers with spin up and down, we emulated the dynamics of two dimensional layer and quantum dot populations successfully. This study provides a tool to describe photo-absorption and magneto-absorption process in order to take advantage of phonon states present in the wetting layer and allow us to access the resonance conditions between the bulk and quantum dot states. These resonant transitions yield to photoluminescence emissions in both structures that can be measured. Other goal of this study was to understand the situations with an imbalance of spin up and down population evidenced by the quantum dot emission, a fact already proved experimentally. A linearly polarized excitation enabled the detection of both populations in bulk. However in the quantum dot we have a spin filtering mechanism in place since the resonant emissions for each spin states occurs at different values of magnetic field, and hence the detection depends on the circular polarization. When the polarization is circular, the collection in bulk or quantum dot reaches a maximum for both spin up and down populations at the same values of  $B$ . An important role is played by impurities levels, which act as spin-flip blocking for transitions into the quantum dot.

### **Scattering Process and Electron Dynamics in 2D Semiconductors Layers**

The characterization of scattering processes at low energies in transition metal dichalcogenides monolayers locally perturbed was obtained. We use the scattering theory in two dimensions to determine the differential cross section generated by two types of perturbation potentials: well and barrier. These potential conditions could be achieved by the deposition of photosensitive molecules as, for instance, the azobenzene derivatives. Peculiar features were found such as an

---

on-off mechanism in the carrier transport for well-barrier perturbation and furthermore, the modulation of scattering has been investigated for deep and large well/barrier cases as well as the incident electron momentum. We found the best conditions for allowed and blocked scattering in the forward direction of the perturbation potential. A comparison between Dirac-like and parabolic-like carriers in terms of phase shift gained by the interaction with  $V$  has also been performed; at low energy regimes of incident electrons both electronic structures are comparable, whereas for high energies we can predict that carriers ruled by Schrödinger equation have more probability to be found in forward direction, in contrast with those ruled by Dirac-like equation since they are scattered even when moving with high momenta.

It is well-known that the state hybridization engineering represents a crucial step towards achieving the band structure modulation of any material and consequently in its successfully application on nanoscale devices. In this thesis, some optical and electronic phenomena were studied in two dimensional systems based on GaAs and  $MoS_2$ . Nonetheless, our analysis is not restricted to these materials, and could be easily extended over many other heterostructures and/or add more perturbational effects in order to gain further control in the response of 2D systems.

We were able to emulate theoretically the processes influencing the dynamics of the carrier transport during the operation of semiconducting devices. In this way, we could propose modifications in the external parameter that may lead to improvements in the device performance, since the kind of perturbations studied here are expected to be controlled in semiconductor nanostructures. All the theoretical models developed in this study are general enough to be extended for other structures such as quantum dots or quantum wires.

In particular, the results presented in chapter 2 pave the way for future investigations aiming to relate them with some experimental facts. An analysis identical to the one presented in chapter 3 can be developed, but with an Hamiltonian that includes modifications of lattice parameter due to local perturbations. Concomitantly, all of these results are currently being condensed in scientific papers. We highlight that the joining efforts from the experimental and theoretical teams in a fruitful collaboration

paved the way for achieving a clear and broad understanding of the fundamental physics in modern semiconducting devices, starting from the background of electronic structure and quantum transport phenomena towards the laborious tasks of fabrication and modeling quasi two dimensional structures and devices.

# Appendices



# Appendix A

## Matrix Representation of the Luttinger Hamiltonian

The Luttinger Hamiltonian that considers the coupling between heavy and light hole and their respective spin components under an applied magnetic field,  $B$ , is shown next [38].

$$\begin{pmatrix}
 |HH^1 \uparrow\rangle & |LH^1 \uparrow\rangle & |LH^1 \downarrow\rangle & |HH^1 \downarrow\rangle & |HH^2 \uparrow\rangle & |LH^2 \uparrow\rangle & |LH^2 \downarrow\rangle & |HH^2 \downarrow\rangle & \\
 a_{11} & a_{12} & a_{13} & a_{14} & a_{15} & a_{16} & a_{17} & a_{18} & |N_L - 2\rangle_1 \\
 & a_{22} & a_{23} & a_{24} & a_{25} & a_{26} & a_{27} & a_{28} & |N_L - 1\rangle_1 \\
 & & a_{33} & a_{34} & a_{35} & a_{36} & a_{37} & a_{38} & |N_L\rangle_1 \\
 & & & a_{44} & a_{45} & a_{46} & a_{47} & a_{48} & |N_L + 1\rangle_1 \\
 & & & & a_{55} & a_{56} & a_{57} & a_{58} & |N_L - 2\rangle_2 \\
 & & & & & a_{66} & a_{67} & a_{68} & |N_L - 1\rangle_2 \\
 & & & & & & a_{77} & a_{78} & |N_L\rangle_2 \\
 & & & & & & & a_{88} & |N_L + 1\rangle_2
 \end{pmatrix} \quad (\text{A.1})$$

Where the super index in the first row and the sub index in the last column label the quantum well subband and the matrix elements different from zero are

$$a_{11} = \frac{-\hbar^2}{2m_0} \left( \frac{eB}{\hbar} \left( (\gamma_1 + \gamma_2) (2(N_L - 2) + 1) + 3 \left( \kappa + \frac{9}{4}q \right) \right) + (\gamma_1 - 2\gamma_2) \left( \frac{\pi}{L} \right)^2 \right)$$

$$a_{22} = \frac{-\hbar^2}{2m_0} \left( \frac{eB}{\hbar} \left( (\gamma_1 - \gamma_2) (2(N_L - 1) + 1) + \left( \kappa + \frac{1}{4}q \right) \right) + (\gamma_1 + 2\gamma_2) \left( \frac{\pi}{L} \right)^2 \right)$$

$$a_{33} = \frac{-\hbar^2}{2m_0} \left( \frac{eB}{\hbar} \left( (\gamma_1 - \gamma_2) (2(N_L) + 1) - \left( \kappa + \frac{1}{4}q \right) \right) + (\gamma_1 + 2\gamma_2) \left( \frac{\pi}{L} \right)^2 \right)$$

$$a_{44} = \frac{-\hbar^2}{2m_0} \left( \frac{eB}{\hbar} \left( (\gamma_1 + \gamma_2) (2(N_L + 1) + 1) - 3 \left( \kappa + \frac{9}{4}q \right) \right) + (\gamma_1 - 2\gamma_2) \left( \frac{\pi}{L} \right)^2 \right)$$

$$a_{55} = \frac{-\hbar^2}{2m_0} \left( \frac{eB}{\hbar} \left( (\gamma_1 + \gamma_2) (2(N_L - 2) + 1) + 3 \left( \kappa + \frac{9}{4}q \right) \right) + (\gamma_1 - 2\gamma_2) \left( \frac{2\pi}{L} \right)^2 \right)$$

$$a_{66} = \frac{-\hbar^2}{2m_0} \left( \frac{eB}{\hbar} \left( (\gamma_1 - \gamma_2) (2(N_L - 1) + 1) + \left( \kappa + \frac{1}{4}q \right) \right) + (\gamma_1 + 2\gamma_2) \left( \frac{2\pi}{L} \right)^2 \right)$$

$$a_{77} = \frac{-\hbar^2}{2m_0} \left( \frac{eB}{\hbar} \left( (\gamma_1 - \gamma_2) (2(N_L) + 1) - \left( \kappa + \frac{1}{4}q \right) \right) + (\gamma_1 + 2\gamma_2) \left( \frac{2\pi}{L} \right)^2 \right)$$

$$a_{88} = \frac{-\hbar^2}{2m_0} \left( \frac{eB}{\hbar} \left( (\gamma_1 + \gamma_2) (2(N_L + 1) + 1) - 3 \left( \kappa + \frac{9}{4}q \right) \right) + (\gamma_1 - 2\gamma_2) \left( \frac{2\pi}{L} \right)^2 \right)$$

$$a_{13} = \frac{e\hbar}{m_0} B \frac{\sqrt{3}}{2} \left( (\gamma_2 + \gamma_3) \sqrt{N_L(N_L - 1)} \right)$$

$$a_{24} = \frac{e\hbar}{m_0} B \frac{\sqrt{3}}{2} \left( (\gamma_2 + \gamma_3) \sqrt{N_L(N_L + 1)} \right)$$

$$a_{57} = \frac{e\hbar}{m_0} B \frac{\sqrt{3}}{2} \left( (\gamma_2 + \gamma_3) \sqrt{N_L(N_L - 1)} \right)$$

$$a_{68} = \frac{e\hbar}{m_0} B \frac{\sqrt{3}}{2} \left( (\gamma_2 + \gamma_3) \sqrt{N_L(N_L + 1)} \right)$$

$$a_{16} = \frac{-\hbar^2}{m_0} \sqrt{\frac{eB}{\hbar}} i \gamma_3 \sqrt{6(N_L - 1)} \frac{8}{3L}$$

$$a_{25} = \frac{\hbar^2}{m_0} \sqrt{\frac{eB}{\hbar}} i \gamma_3 \sqrt{6(N_L - 1)} \frac{8}{3L}$$



---

$$a_{38} = \frac{\hbar^2}{m_0} \sqrt{\frac{eB}{\hbar}} i \gamma_3 \sqrt{6(N_L + 1)} \frac{8}{3L}$$

$$a_{47} = \frac{-\hbar^2}{m_0} \sqrt{\frac{eB}{\hbar}} i \gamma_3 \sqrt{6(N_L + 1)} \frac{8}{3L}$$



# Appendix B

## Rotation of Luttinger Hamiltonian for Zincblende Crystal

In order to specify directions and planes in a crystal we use Miller indices [100]. They are defined with respect to any choice of unit cell, in general this choosing is with respect to primitive basis vectors and are determined as the inverse intercepts along the lattice vectors. If the index value is 0 it means that the plane is parallel to its crystallographic axis, a negative index is represented by a horizontal bar on the top of the number. The usual notation is  $h, k, l$ . The writing  $(h, k, l)$  denotes a crystallographic plane and  $[h, k, l]$  denotes a direction.

The new coordinate system used to rotate the Luttinger Hamiltonian is as follow: the axis 3 along the growth direction, the 1 and 3 axes in the  $(\bar{1}10)$  plane, and the 2 axis in the  $[\bar{1}10]$  direction, see Figure B.1. The angle between axis 3 and the x-y plane of the original coordinate system is denoted by  $\theta$ ; thus when  $\theta$  varies from 0 to  $\frac{\pi}{2}$ , the growth surface which is perpendicular to the 3 axis changes from (110) to (111), (112), (113), until  $(11\infty)$ , i.e. (001) as shown on Figure B.2

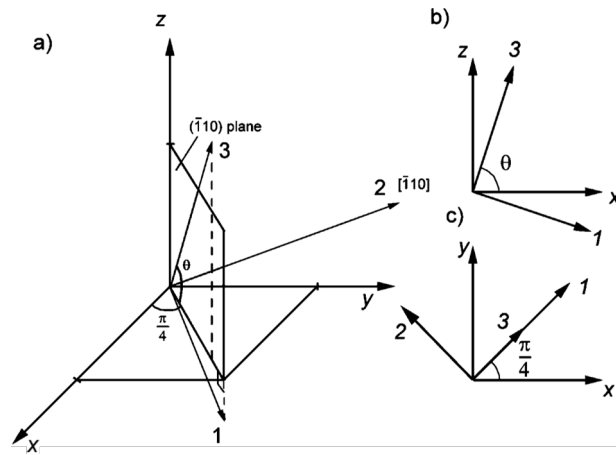


**Figure B.1:** Rotation of coordinate system  $(x, y, z)$  where  $z$  axis is perpendicular to  $(001)$  plane. a) The 1, 2 and 3 axes of the rotated coordinate system. Axis 2 is perpendicular to 1-3 plane which is parallel to  $(\bar{1}10)$  plane; the crystal is growing along axis 3; the system is rotated about axis 2 for angle  $\theta$ . b) Side view of  $x$ - $z$  and 1-3 planes. c) Upside down view of  $x$ - $y$  and 1-2 planes, coordinate system rotated to  $\frac{\pi}{4}$  angle

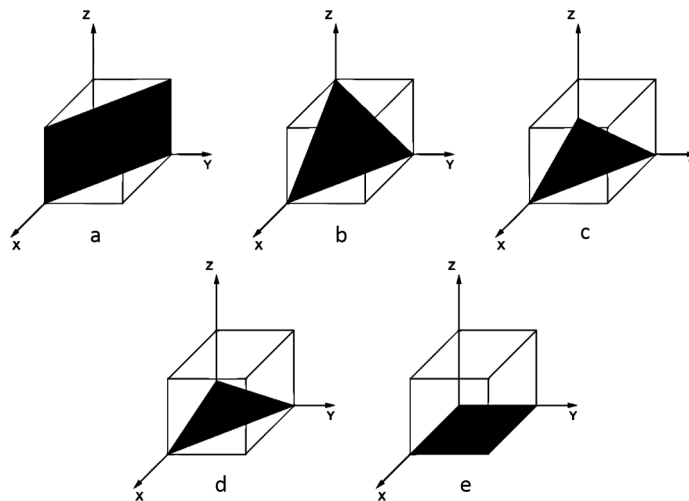


**Figure B.2:** Growth surfaces in Miller indexes notation: a -  $(110)$ , b -  $(111)$ , c -  $(112)$ , d -  $(113)$ , e -  $(11\infty)$ . Growth direction is perpendicular to plane which is colored in black

# Appendix C

## Scattering Systems

### C.1 Dirac Dynamic

The Hamiltonian for massive Dirac fermions is presented below (In this work, we will use the  $MoS_2$  monolayer parameters found in Ref. 101)

$$H_D = at(\tau q_x \sigma_x + q_y \sigma_y) + \frac{\Delta}{2} \sigma_z - \tau \lambda \frac{\sigma_z - 1}{2} s_z, \quad (C.1)$$

where the energy gap  $\Delta$  is 1.66meV, the spin-orbit coupling at the valence band,  $2\lambda$  is 150meV,  $a = 3.193\text{\AA}$  is the lattice constant and  $t = 1.10\text{eV}$  is the effective hopping integral. These parameters describe  $MoS_2$  as seen in table 4.1. The valleys are uncoupled and it is possible to consider the scattering problem at each valley and spin independently. The equation for  $\psi$  is

$$H_D \psi = \begin{pmatrix} \Delta/2 + V & atq_- \\ atq_+ & -\Delta/2 + \lambda + V \end{pmatrix} \begin{pmatrix} \psi_a \\ \psi_b \end{pmatrix} = E\psi. \quad (C.2)$$

We are interested in building a set of eigenfunctions for both  $H$  and  $J_z = l_z + \frac{1}{2}\sigma_z + \frac{1}{2}s_z$ , then we should know the relation between the phases of the components  $\psi_a$  and  $\psi_b$ . Towards this end, first we will build a generic form of the eigenfunction, from (C.2)

$$(\Delta/2 + V)\psi_a + atq_- \psi_b = E\psi_a \quad (C.3)$$

and

$$(-\Delta/2 + \lambda + V)\psi_b + atq_+ \psi_a = E\psi_b. \quad (C.4)$$

Manipulating (C.3)

$$\psi_b = \psi_a \frac{-\Delta/2 + (E - V)}{atq_-} \quad (\text{C.5})$$

$$= \psi_a \frac{-\Delta/2 + (E - V)}{atq} e^{i\theta} \quad (\text{C.6})$$

$$\psi = \psi_a \begin{pmatrix} 1 \\ \frac{-\Delta/2 + (E - V)}{atq} e^{i\theta} \end{pmatrix} = a \begin{pmatrix} 1 \\ \gamma e^{i\theta} \end{pmatrix} \quad (\text{C.7})$$

taking  $a = Ae^{im\theta}$  we obtain a set of eigenfunctions for both  $H$  and  $J_z$ :

$$J_z \psi = J_z A \begin{pmatrix} 1 \\ \gamma e^{i\theta} \end{pmatrix} e^{im\theta} = \left( L_z + \frac{\hbar}{2} \sigma_z \right) A \begin{pmatrix} 1 \\ \gamma e^{i\theta} \end{pmatrix} e^{im\theta} \quad (\text{C.8})$$

$$= A\hbar \begin{pmatrix} m \\ \gamma(m+1)e^{i\theta} \end{pmatrix} e^{im\theta} + A \begin{pmatrix} \hbar/2 \\ -\hbar/2\gamma e^{i\theta} \end{pmatrix} e^{im\theta} \quad (\text{C.9})$$

$$= \hbar(m + 1/2) A \begin{pmatrix} 1 \\ \gamma e^{i\theta} \end{pmatrix} e^{im\theta} \quad (\text{C.10})$$

$$J_z \psi = \hbar(m + 1/2) \psi. \quad (\text{C.11})$$

Now, with the angular part on hand, we will compute the radial part of  $\psi$ , that should satisfy

$$\begin{pmatrix} \Delta/2 + V & atq_- \\ atq_+ & -\Delta/2 + \lambda + V \end{pmatrix} A \begin{pmatrix} \psi_a \\ \psi_b \gamma e^{i\theta} \end{pmatrix} e^{im\theta} = EA \begin{pmatrix} \psi_a \\ \psi_b \gamma e^{i\theta} \end{pmatrix} e^{im\theta}. \quad (\text{C.12})$$

Using  $q_{\pm} = -ie^{\pm i\theta}(\partial_r \pm i/r\partial_{\theta})$  we write the equation system as

$$\left( \frac{\Delta}{2} + V \right) \psi_a - iat \left( \partial_r + \frac{m+1}{r} \right) \gamma \psi_b = E\psi_a \quad (\text{C.13})$$

and

$$\left( \frac{-\Delta}{2} + \lambda + V \right) \gamma \psi_b - iat \left( \partial_r - \frac{m}{r} \right) \psi_a = E\gamma \psi_b. \quad (\text{C.14})$$

We obtain the relation between  $\psi_a$  and  $\psi_b$  from the last equation:  $\gamma \psi_b = \frac{-iat(\partial_r - m/r)\psi_a}{-\Delta/2 + \lambda - (E - V)}$ .

Putting this into (C.13) we have

$$\left( \frac{\Delta}{2} - (E - V) \right) \psi_a + \frac{a^2 t^2}{-\Delta/2 + \lambda - (E - V)} \left( \frac{d}{dr} + \frac{m+1}{r} \right) \left( \frac{d}{dr} - \frac{m}{r} \right) \psi_a = 0 \quad (\text{C.15})$$

$$\left(\frac{\Delta}{2} - (E - V)\right) \psi_a + \frac{a^2 t^2}{-\Delta/2 + \lambda - (E - V)} \left(d_r^2 + \frac{1}{r} d_r - \frac{m^2}{r^2}\right) \psi_a = 0 \quad (\text{C.16})$$

$$\left(d_r^2 + \frac{1}{r} d_r - \frac{m^2}{r^2} + \frac{-\Delta/2 + \lambda - (E - V)}{a^2 t^2} (\Delta/2 - (E - V))\right) \psi_a = 0 \quad (\text{C.17})$$

$$\left(d_r^2 + \frac{1}{r} d_r - \frac{m^2}{r^2} + q^2\right) \psi_a = 0 \quad (\text{C.18})$$

or

$$\left(\rho^2 \frac{d^2}{d\rho^2} + \rho \frac{d}{d\rho} + (\rho^2 - m^2)\right) \psi_a = 0 \quad (\text{C.19})$$

where  $\rho = qr$  and  $q = \frac{1}{at} \sqrt{(E - V)^2 - \lambda(E - V) - \frac{\Delta}{2} \left(\frac{\Delta}{2} - \lambda\right)}$ . The solutions to (C.19) are the Bessel functions [57].

The relation between  $\psi_a$  and  $\psi_b$  is derived from

$$\gamma \psi_b = \frac{-iat}{-\Delta/2 + \lambda - (E - V)} (\partial_r - m/r) \psi_a. \quad (\text{C.20})$$

For example, the second component of  $\psi_m^i$  is

$$\gamma \psi_b = \frac{-iat}{-\Delta/2 + \lambda - (E - V)} (\partial_r - m/r) N_m J_m(qr) \quad (\text{C.21})$$

$$= \frac{-iat}{-\Delta/2 + \lambda - (E - V)} N_m q \left( J'_m(qr) - \frac{m}{qr} J_m(qr) \right) \quad (\text{C.22})$$

$$= \frac{-iat}{-\Delta/2 + \lambda - (E - V)} N_m q J_{m+1}(qr), \quad (\text{C.23})$$

where  $J'_m(x) = J_{m-1}(x) - \frac{m}{x} J_m(x)$  was used and the recurrence relation  $J_{m-1}(x) + J_{m+1}(x) = \frac{2m}{x} J_m(x)$ . For  $0 \leq r \leq L$

$$\psi_m^i = N_m \left( \begin{array}{c} J_m(qr) e^{im\theta} \\ \frac{-iatq}{-\Delta/2 + \lambda - (E - V)} J_{m+1}(qr) e^{i(m+1)\theta} \end{array} \right). \quad (\text{C.24})$$

The process for  $\gamma \psi_b$  of  $\psi_m^o$  is analogous,

$$\psi_m^o = \left( \begin{array}{c} N_1 H_m^2(\tilde{q}r) + N_2 e^{2i\delta_m} H_m^1(\tilde{q}r) \\ \frac{-iat\tilde{q}}{-\Delta/2 + \lambda - E} \left( N_1 H_{m+1}^2(\tilde{q}r) + N_2 e^{2i\delta_m} H_{m+1}^1(\tilde{q}r) \right) e^{i\theta} \end{array} \right) e^{im\theta}. \quad (\text{C.25})$$

For convenience, we manipulate the last expression to write

$$\psi_m^o = \left( \begin{array}{c} N_1 H_m^2(\tilde{q}r) + N_2 e^{2i\delta_m} H_m^1(\tilde{q}r) + N_1 H_m^1(\tilde{q}r) - N_1 H_m^1(\tilde{q}r) \\ \frac{-iat\tilde{q}}{-\Delta/2 + \lambda - E} \left( N_1 H_{m+1}^2(\tilde{q}r) + N_2 e^{2i\delta_m} H_{m+1}^1(\tilde{q}r) + N_1 H_{m+1}^1(\tilde{q}r) - N_1 H_{m+1}^1(\tilde{q}r) \right) e^{i\theta} \end{array} \right) e^{im\theta} \quad (\text{C.26})$$

$$= \left( \begin{array}{c} 2N_1 J_m(\tilde{q}r) + (N_2 e^{2i\delta_m} - N_1) H_m^1(\tilde{q}r) \\ \frac{-iat\tilde{q}}{-\Delta/2+\lambda-E} (2N_1 J_{m+1}(\tilde{q}r) + (N_2 e^{2i\delta_m} - N_1) H_{m+1}^1(\tilde{q}r)) e^{i\theta} \end{array} \right) e^{im\theta}. \quad (\text{C.27})$$

taking  $N_1 = \frac{i^m}{2} = \frac{e^{im\pi/2}}{2}$  we have

$$\psi_m^o = \left( \begin{array}{c} e^{im\pi/2} (J_m(\tilde{q}r) + \frac{e^{2i\delta_m}-1}{2} H_m^1(\tilde{q}r)) \\ \frac{-iat\tilde{q}e^{im\pi/2}}{-\Delta/2+\lambda-E} (J_{m+1}(\tilde{q}r) + \frac{e^{2i\delta_m}-1}{2} H_{m+1}^1(\tilde{q}r)) e^{i\theta} \end{array} \right) e^{im\theta}. \quad (\text{C.28})$$

The normalization constant  $N_m$  and the phase shift  $\delta_m$  are determined from the boundary condition, where  $\psi_m^i|_L = \psi_m^o|_L$  which leads to

$$N_m \left( \begin{array}{c} J_m(qL) \\ \frac{-iatq}{-\Delta/2+\lambda-(E-V)} J_{m+1}(qL) e^{i\theta} \end{array} \right) = \left( \begin{array}{c} e^{im\pi/2} (J_m(\tilde{q}L) + \frac{e^{2i\delta_m}-1}{2} H_m^1(\tilde{q}L)) \\ \frac{e^{im\pi/2}-iat\tilde{q}}{-\Delta/2+\lambda-(E-V)} (J_{m+1}(\tilde{q}L) + \frac{e^{2i\delta_m}-1}{2} H_{m+1}^1(\tilde{q}L)) e^{i\theta} \end{array} \right). \quad (\text{C.29})$$

By adding all  $m$  channels and using the asymptotic form  $H_m$  we have

$$\psi(r \rightarrow \infty) = e^{i\tilde{q}\cdot\mathbf{r}} \left( \begin{array}{c} 1 \\ \frac{-at\tilde{q}}{-\Delta/2+\lambda-E} \end{array} \right) + \sum_{m=-\infty}^{\infty} \frac{e^{2i\delta_m}-1}{2} \sqrt{\frac{2}{i\pi\tilde{q}}} e^{im\theta} \left( \begin{array}{c} 1 \\ \frac{-at\tilde{q}}{-\Delta/2+\lambda-E} e^{i\theta} \end{array} \right) \frac{e^{i\tilde{q}r}}{\sqrt{r}} \quad (\text{C.30})$$

or

$$\psi = e^{i\tilde{q}\cdot\mathbf{r}} \left( \begin{array}{c} 1 \\ \frac{-at\tilde{q}}{-\Delta/2+\lambda-E} \end{array} \right) + f(\tilde{q}, \theta) \left( \begin{array}{c} 1 \\ \frac{-at\tilde{q}}{-\Delta/2+\lambda-E} e^{i\theta} \end{array} \right) \frac{e^{i\tilde{q}r}}{\sqrt{r}} \quad (\text{C.31})$$

with

$$f(\tilde{q}, \theta) = \sum_{m=-\infty}^{\infty} \frac{e^{2i\delta_m}-1}{2} \sqrt{\frac{2}{i\pi\tilde{q}}} e^{im\theta} \quad (\text{C.32})$$

### C.1.1 Schrödinger Dynamics

The function outside the scattering region takes the form

$$\psi_m^o = \sqrt{\frac{1}{2\pi}} N_o e^{im\theta} [H_m^{(1)}(\tilde{k}r) + H_m^{(2)}(\tilde{k}r)]. \quad (\text{C.33})$$

That is a combination of outgoing and incoming waves.



As a result of scattering, the outgoing wave gets an additional phase  $2\delta_m$ , so

$$\psi_m^o = \sqrt{\frac{1}{2\pi}} N_o e^{im\theta} \left[ H_m^{(2)}(\tilde{k}r) + e^{2i\delta_m} H_m^{(1)}(\tilde{k}r) \right] \quad (\text{C.34})$$

$$= \sqrt{\frac{1}{2\pi}} N_o e^{im\theta} \left[ H_m^{(2)}(\tilde{k}r) + H_m^{(1)}(\tilde{k}r) - H_m^{(1)}(\tilde{k}r) + e^{2i\delta_m} H_m^{(1)}(\tilde{k}r) \right] \quad (\text{C.35})$$

$$= \sqrt{\frac{1}{2\pi}} N_o e^{im\theta} 2 \left[ J_m(\tilde{k}r) + \frac{e^{2i\delta_m} - 1}{2} H_m^{(1)}(\tilde{k}r) \right] \quad (\text{C.36})$$

but

$$\psi = \sum_{m=0}^{\infty} C_m \psi_m^o \quad (\text{C.37})$$

$$= \sum_{m=-\infty}^{\infty} \sqrt{\frac{1}{2\pi}} N_o 2 \left[ J_m(\tilde{k}r) e^{im\theta} + \frac{e^{2i\delta_m} - 1}{2} H_m^{(1)}(\tilde{k}r) e^{im\theta} \right]. \quad (\text{C.38})$$

Setting  $N_o = \frac{i^m}{2}$  we have

$$\psi = \sum_{m=-\infty}^{\infty} \sqrt{\frac{1}{2\pi}} \left[ i^m J_m(\tilde{k}r) e^{im\theta} + i^m \frac{e^{2i\delta_m} - 1}{2} H_m^{(1)}(\tilde{k}r) e^{im\theta} \right]. \quad (\text{C.39})$$

Furthermore, using the Jacobi-Anger identity, we have

$$\psi = \sqrt{\frac{1}{2\pi}} e^{i\tilde{k}\cdot\mathbf{r}} + \sum_{m=-\infty}^{\infty} \sqrt{\frac{1}{2\pi}} i^m \frac{e^{2i\delta_m} - 1}{2} H_m^{(1)}(\tilde{k}r) e^{im\theta} \quad (\text{C.40})$$

$$= \sqrt{\frac{1}{2\pi}} e^{i\tilde{k}\cdot\mathbf{r}} + \sum_{m=1}^{\infty} \sqrt{\frac{1}{2\pi}} i^{-m} \frac{e^{2i\delta_{-m}} - 1}{2} H_{-m}^{(1)}(\tilde{k}r) e^{-im\theta} +$$

$$\sum_{m=1}^{\infty} \sqrt{\frac{1}{2\pi}} i^m \frac{e^{2i\delta_m} - 1}{2} H_m^{(1)}(\tilde{k}r) e^{im\theta} + \sqrt{\frac{1}{2\pi}} \frac{e^{2i\delta_0} - 1}{2} H_0^{(1)}(\tilde{k}r) \quad (\text{C.41})$$

$$e^{2i\delta_{-m}} = \frac{H_{-m}^{(2)}(\tilde{k}L)' - B_{-m} H_{-m}^{(2)}(\tilde{k}L)}{B_{-m} H_{-m}^{(1)}(\tilde{k}L) - H_{-m}^{(1)}(\tilde{k}L)'} \quad (\text{C.42})$$

$$B_{-m} = \frac{k J_{-m}'(kL)}{\tilde{k} J_{-m}(kL)} \quad (\text{C.43})$$

$$= \frac{k J_{-m-1}(kL) - J_{-m+1}(kL)}{\tilde{k} J_{-m}(kL)} \quad (\text{C.44})$$

$$= \frac{k J_{-(m+1)}(kL) - J_{-(m-1)}(kL)}{\tilde{k} J_{-m}(kL)} \quad (\text{C.45})$$

$$= \frac{k}{\tilde{k}} \frac{(-1)^{m+1} J_{m+1}(kL) - (-1)^{m-1} J_{m-1}(kL)}{(-1)^m J_m(kL)} \quad (\text{C.46})$$

$$= \frac{k}{\tilde{k}} \frac{J_{m-1}(kL) - J_{m+1}(kL)}{J_m(kL)} \quad (\text{C.47})$$

$$= B_m \quad (\text{C.48})$$

$$e^{2i\delta-m} = \frac{(-1)^{-m} H_m^{(2)}(\tilde{k}L)' - B_m (-1)^{-m} H_m^{(2)}(\tilde{k}L)}{B_m (-1)^m H_m^{(1)}(\tilde{k}L) - (-1)^m H_m^{(1)}(\tilde{k}L)'} \quad (\text{C.49})$$

$$= \frac{H_m^{(2)}(\tilde{k}L)' - B_m H_m^{(2)}(\tilde{k}L)}{B_m H_m^{(1)}(\tilde{k}L) - H_m^{(1)}(\tilde{k}L)'} \quad (\text{C.50})$$

$$= e^{2i\delta m}. \quad (\text{C.51})$$

Thus,

$$\begin{aligned} \psi &= \sqrt{\frac{1}{2\pi}} e^{i\tilde{\mathbf{k}}\cdot\mathbf{r}} + \sum_{m=1}^{\infty} \sqrt{\frac{1}{2\pi}} i^{-m} \frac{e^{2i\delta m} - 1}{2} e^{i\pi m} H_m^{(1)}(\tilde{k}r) e^{-im\theta} + \\ &\quad \sum_{m=1}^{\infty} \sqrt{\frac{1}{2\pi}} i^m \frac{e^{2i\delta m} - 1}{2} H_m^{(1)}(\tilde{k}r) e^{im\theta} + \sqrt{\frac{1}{2\pi}} \frac{e^{2i\delta_0} - 1}{2} H_0^{(1)}(\tilde{k}r) \end{aligned} \quad (\text{C.52})$$

$$\begin{aligned} &= \sqrt{\frac{1}{2\pi}} e^{i\tilde{\mathbf{k}}\cdot\mathbf{r}} + \sum_{m=1}^{\infty} \sqrt{\frac{1}{2\pi}} \frac{e^{2i\delta m} - 1}{2} H_m^{(1)}(\tilde{k}r) \left( i^{-m} e^{-im\theta} e^{i\pi m} + i^m e^{im\theta} \right) + \\ &\quad \sqrt{\frac{1}{2\pi}} \frac{e^{2i\delta_0} - 1}{2} H_0^{(1)}(\tilde{k}r) \end{aligned} \quad (\text{C.53})$$

$$i^{-m} e^{i\pi m} = i^m$$

$$\psi = \sqrt{\frac{1}{2\pi}} e^{i\tilde{\mathbf{k}}\cdot\mathbf{r}} + \sum_{m=1}^{\infty} \sqrt{\frac{1}{2\pi}} i^m \frac{e^{2i\delta m} - 1}{2} H_m^{(1)}(\tilde{k}r) (e^{im\theta} + e^{-im\theta}) + \sqrt{\frac{1}{2\pi}} \frac{e^{2i\delta_0} - 1}{2} H_0^{(1)}(\tilde{k}r) \quad (\text{C.54})$$

$$\psi = \sqrt{\frac{1}{2\pi}} e^{i\tilde{\mathbf{k}}\cdot\mathbf{r}} + \sum_{m=0}^{\infty} C_m \sqrt{\frac{1}{2\pi}} i^m \frac{e^{2i\delta m} - 1}{2} H_m^{(1)}(\tilde{k}r) \cos(m\theta) \quad (\text{C.55})$$

$$\psi = e^{i\tilde{\mathbf{k}}\cdot\mathbf{r}} + \sum_{m=0}^{\infty} C_m i^m \sqrt{\frac{2}{\pi \tilde{k}}} \frac{e^{2i\delta m} - 1}{2} \cos(m\theta) e^{-i\frac{\pi}{2}(m+1/2)} \frac{e^{i\tilde{k}r}}{\sqrt{r}} \quad (\text{C.56})$$

$$\psi = e^{i\tilde{\mathbf{k}}\cdot\mathbf{r}} + \sum_{m=0}^{\infty} C_m \sqrt{\frac{2}{\pi \tilde{k}}} \frac{e^{2i\delta m} - 1}{2} \cos(m\theta) e^{-i\frac{\pi}{4}} \frac{e^{i\tilde{k}r}}{\sqrt{r}} \quad (\text{C.57})$$

with  $C_0 = 1$  and all other  $C_m = 2$ . from the asymptotic form of  $\psi$

$$\psi = e^{i\vec{k}\cdot\mathbf{r}} + f(\theta) \frac{e^{i\tilde{k}r}}{\sqrt{r}} \quad (\text{C.58})$$

is possible to identify the scattering amplitude  $f(\theta)$ ,

$$f(\theta) = \sum_{m=0}^{\infty} C_m \sqrt{\frac{2}{i\pi\tilde{k}}} \frac{e^{2i\delta_m} - 1}{2} \cos(m\theta). \quad (\text{C.59})$$

## C.2 Asymptotic Analysis

### C.2.1 Dirac Formulation

From

$$e^{2i\delta_m} = \frac{H_{m+1}^{(2)}(\tilde{q}L)J_m(qL) - DH_m^{(2)}(\tilde{q}L)J_{m+1}(qL)}{DH_m^{(1)}(\tilde{q}L)J_{m+1}(qL) - H_{m+1}^{(1)}(\tilde{q}L)J_m(qL)}, \quad (\text{C.60})$$

where

$$q = \frac{1}{at} \sqrt{(E - V)^2 - \lambda(E - V) - \frac{\Delta}{2} \left( \frac{\Delta}{2} - \lambda \right)}, \quad (\text{C.61})$$

$$\tilde{q} = \frac{1}{at} \sqrt{E^2 - \lambda E - \frac{\Delta}{2} \left( \frac{\Delta}{2} - \lambda \right)}, \quad (\text{C.62})$$

$$D = \frac{-\Delta/2 + \lambda - E}{-\Delta/2 + \lambda - (E - V)} \frac{q}{\tilde{q}}, \quad (\text{C.63})$$

we obtain an expression for  $\delta_m$  in terms of tan, after that, a detailed calculation is presented until the final expressions for both limits are derived. For simplicity we change notation from here, all arguments will disappear and functions using tilde are indicating dependence on tilde arguments, thus,

$$e^{2i\delta_m} = \frac{\tilde{H}_{m+1}^{(2)} J_m - D \tilde{H}_m^{(2)} J_{m+1}}{D \tilde{H}_m^{(1)} J_{m+1} - \tilde{H}_{m+1}^{(1)} J_m} \quad (\text{C.64})$$

$$e^{2i\delta_m} = \frac{(\tilde{J}_{m+1} - i\tilde{Y}_{m+1})J_m - DJ_{m+1}(\tilde{J}_m - i\tilde{Y}_m)}{DJ_{m+1}(\tilde{J}_m + i\tilde{Y}_m) - (\tilde{J}_{m+1} + i\tilde{Y}_{m+1})J_m} \quad (\text{C.65})$$

$$= \frac{\tilde{J}_{m+1}J_m - DJ_{m+1}\tilde{J}_m - i(\tilde{Y}_{m+1}J_m - DJ_{m+1}\tilde{Y}_m)}{-\tilde{J}_{m+1}J_m + DJ_{m+1}\tilde{J}_m - i(\tilde{Y}_{m+1}J_m - DJ_{m+1}\tilde{Y}_m)} \quad (\text{C.66})$$

$$= -\frac{\tilde{J}_{m+1}J_m - DJ_{m+1}\tilde{J}_m - i(\tilde{Y}_{m+1}J_m - DJ_{m+1}\tilde{Y}_m)}{\tilde{J}_{m+1}J_m - DJ_{m+1}\tilde{J}_m - i(\tilde{Y}_{m+1}J_m - DJ_{m+1}\tilde{Y}_m)} \quad (\text{C.67})$$

$$= -1 \frac{(\tilde{J}_{m+1}J_m - DJ_{m+1}\tilde{J}_m)^2 - (\tilde{Y}_{m+1}J_m - DJ_{m+1}\tilde{Y}_m)^2}{(\tilde{J}_{m+1}J_m - DJ_{m+1}\tilde{J}_m)^2 + (\tilde{Y}_{m+1}J_m - DJ_{m+1}\tilde{Y}_m)^2} + \frac{2i(\tilde{J}_{m+1}J_m - DJ_{m+1}\tilde{J}_m)(\tilde{Y}_{m+1}J_m - DJ_{m+1}\tilde{Y}_m)}{(\tilde{J}_{m+1}J_m - DJ_{m+1}\tilde{J}_m)^2 + (\tilde{Y}_{m+1}J_m - DJ_{m+1}\tilde{Y}_m)^2} \quad (\text{C.68})$$

$$\tan(2\delta_m) = 2 \frac{(\tilde{J}_{m+1}J_m - DJ_{m+1}\tilde{J}_m)(\tilde{Y}_{m+1}J_m - DJ_{m+1}\tilde{Y}_m)}{(\tilde{Y}_{m+1}J_m - DJ_{m+1}\tilde{Y}_m)^2 - (\tilde{J}_{m+1}J_m - DJ_{m+1}\tilde{J}_m)^2} \quad (\text{C.69})$$

$$\tan(\delta_m) = \frac{\tilde{J}_{m+1}J_m - DJ_{m+1}\tilde{J}_m}{\tilde{Y}_{m+1}J_m - DJ_{m+1}\tilde{Y}_m} \quad (\text{C.70})$$

In the  $\tilde{q} \rightarrow \infty$  limit  $D \approx 1$ , and after some mathematical manipulation, we have

$$\tilde{J}_{m+1}J_m \approx \sqrt{\frac{2}{\pi L^2}} \sqrt{\frac{1}{q\tilde{q}}} \cos\left(\tilde{q}L - \frac{\pi}{2}\left(m + \frac{1}{2}\right) - \frac{\pi}{2}\right) \cos\left(qL - \frac{\pi}{2}\left(m + \frac{1}{2}\right)\right) \quad (\text{C.71})$$

$$= \sqrt{\frac{2}{\pi L^2}} \sqrt{\frac{1}{q\tilde{q}}} \sin\left(\tilde{q}L - \frac{\pi}{2}\left(m + \frac{1}{2}\right)\right) \cos\left(qL - \frac{\pi}{2}\left(m + \frac{1}{2}\right)\right) \quad (\text{C.72})$$

$$J_{m+1}\tilde{J}_m \approx \sqrt{\frac{2}{\pi L^2}} \sqrt{\frac{1}{q\tilde{q}}} \cos\left(qL - \frac{\pi}{2}\left(m + \frac{1}{2}\right) - \frac{\pi}{2}\right) \cos\left(\tilde{q}L - \frac{\pi}{2}\left(m + \frac{1}{2}\right)\right) \quad (\text{C.73})$$

$$= \sqrt{\frac{2}{\pi L^2}} \sqrt{\frac{1}{q\tilde{q}}} \sin\left(qL - \frac{\pi}{2}\left(m + \frac{1}{2}\right)\right) \cos\left(\tilde{q}L - \frac{\pi}{2}\left(m + \frac{1}{2}\right)\right) \quad (\text{C.74})$$

the numerator has the form

$$\tilde{J}_{m+1}J_m - DJ_{m+1}\tilde{J}_m = \sqrt{\frac{2}{\pi L^2}} \sqrt{\frac{1}{q\tilde{q}}} \sin(\tilde{q} - q) \quad (\text{C.75})$$

on the other hand,

$$\tilde{Y}_{m+1}J_m \approx \sqrt{\frac{2}{\pi L^2}} \sqrt{\frac{1}{q\tilde{q}}} \sin\left(\tilde{q}L - \frac{\pi}{2}\left(m + \frac{1}{2}\right) - \frac{\pi}{2}\right) \cos\left(qL - \frac{\pi}{2}\left(m + \frac{1}{2}\right)\right) \quad (\text{C.76})$$

$$= \sqrt{\frac{2}{\pi L^2}} \sqrt{\frac{1}{q\tilde{q}}} (-1) \cos\left(\tilde{q}L - \frac{\pi}{2}\left(m + \frac{1}{2}\right)\right) \cos\left(qL - \frac{\pi}{2}\left(m + \frac{1}{2}\right)\right) \quad (\text{C.77})$$

$$J_{m+1}\tilde{Y}_m \approx \sqrt{\frac{2}{\pi L^2}} \sqrt{\frac{1}{q\tilde{q}}} \cos\left(qL - \frac{\pi}{2}\left(m + \frac{1}{2}\right) - \frac{\pi}{2}\right) \sin\left(\tilde{q}L - \frac{\pi}{2}\left(m + \frac{1}{2}\right)\right) \quad (\text{C.78})$$

$$= \sqrt{\frac{2}{\pi L^2}} \sqrt{\frac{1}{q\tilde{q}}} \sin\left(qL - \frac{\pi}{2}\left(m + \frac{1}{2}\right)\right) \sin\left(\tilde{q}L - \frac{\pi}{2}\left(m + \frac{1}{2}\right)\right) \quad (\text{C.79})$$

and the denominator has the form,

$$\tilde{Y}_{m+1}J_m - DJ_{m+1}\tilde{Y}_m = -\sqrt{\frac{2}{\pi L^2}}\sqrt{\frac{1}{q\tilde{q}}}\cos(\tilde{q} - q)L. \quad (\text{C.80})$$

Finally,

$$\tan(\delta_m) \approx -\frac{\sin(\tilde{q} - q)L}{\cos(\tilde{q} - q)L} \quad (\text{C.81})$$

$$\approx -(\tilde{q} - q)L \quad (\text{C.82})$$

$$= -\tilde{q}L + \frac{L}{at}\sqrt{a^2t^2\tilde{q}^2 + V^2 - 2VE + \lambda V}. \quad (\text{C.83})$$

But, remembering that

$$E = \frac{\lambda}{2} + \sqrt{\left(\frac{\lambda - \Delta}{2}\right)^2 + a^2t^2\tilde{q}^2} \quad (\text{C.84})$$

$$\underset{\tilde{q} \rightarrow \infty}{\approx} \frac{\lambda}{2} + at\tilde{q} \left(1 + \frac{1}{2} \left(\frac{\lambda - \Delta}{2}\right)^2 \frac{1}{a^2t^2\tilde{q}^2}\right) \quad (\text{C.85})$$

$$\approx at\tilde{q} \quad (\text{C.86})$$

the expression for  $\tan(\delta_m)$  is

$$\tan(\delta_m) = -\tilde{q}L + \frac{L}{at}\sqrt{a^2t^2\tilde{q}^2 + V^2 - 2Vat\tilde{q} + \lambda V} \quad (\text{C.87})$$

$$\approx -\tilde{q}L + \frac{L}{at}at\tilde{q} \left(1 + \frac{1}{2} \frac{V^2 + \lambda V - 2Vat\tilde{q}}{a^2t^2\tilde{q}^2}\right) \quad (\text{C.88})$$

$$\approx -\frac{LV}{at} \quad (\text{C.89})$$

$$\lim_{\tilde{q} \rightarrow \infty} \tan(\delta_m) = -\frac{LV}{at}. \quad (\text{C.90})$$

In order to study the limit of short wave vectors, we shift the coordinate system energy such that the zero is at the bottom of the conduction band, and we rewrite the wave vectors:

$$q = \frac{1}{at}\sqrt{a^2t^2\tilde{q}^2 + V^2 - 2VE + V(\lambda - \Delta)} \quad (\text{C.91})$$

and

$$E = \frac{\lambda - \Delta}{2} + \sqrt{\left(\frac{\lambda - \Delta}{2}\right)^2 + a^2 t^2 \tilde{q}^2} \quad (\text{C.92})$$

$$\approx \frac{\lambda - \Delta}{2} - \frac{\lambda - \Delta}{2} \left(1 + \frac{a^2 t^2}{2} \frac{1}{\left(\frac{\Delta - \lambda}{2}\right)^2 \tilde{q}^2}\right) \quad (\text{C.93})$$

$$= \frac{a^2 t^2}{\lambda - \Delta} \tilde{q}^2, \quad (\text{C.94})$$

then,

$$\frac{q}{\tilde{q}} = \frac{\sqrt{a^2 t^2 \tilde{q}^2 + V^2 - 2VE + V(\lambda - \Delta)}}{at\tilde{q}} \approx \frac{\sqrt{V^2 + V(\lambda - \Delta)}}{at\tilde{q}}, \quad (\text{C.95})$$

and

$$D = \frac{\lambda - \Delta - E}{\lambda - \Delta - (E - V)} \frac{q}{\tilde{q}} \approx \frac{\lambda - \Delta}{\lambda - \Delta + V} \frac{\sqrt{V^2 + V(\lambda - \Delta)}}{at\tilde{q}} \quad (\text{C.96})$$

$$= i \frac{\lambda - \Delta}{\lambda - \Delta + V} \frac{\sqrt{V(\Delta - \lambda) - V^2}}{at\tilde{q}} = i \frac{D_r}{at\tilde{q}}, \quad (\text{C.97})$$

$$e^{2i\delta_m} = \frac{(\tilde{J}_{m+1} - i\tilde{Y}_{m+1})i^m I_m - iD_r i^{m+1} I_{m+1} (\tilde{J}_m - i\tilde{Y}_m)}{iD_r i^{m+1} I_{m+1} (\tilde{J}_m + i\tilde{Y}_m) - (\tilde{J}_{m+1} + i\tilde{Y}_{m+1})i^m I_m} \quad (\text{C.98})$$

$$= \frac{-(\tilde{J}_{m+1} I_m + D_r I_{m+1} \tilde{J}_m) + i(\tilde{Y}_{m+1} I_m + D_r I_{m+1} \tilde{Y}_m)}{\tilde{J}_{m+1} I_m + D_r I_{m+1} \tilde{J}_m + i(\tilde{Y}_{m+1} I_m + D_r I_{m+1} \tilde{Y}_m)} \quad (\text{C.99})$$

$$\tan(\delta_m) = \frac{\tilde{J}_{m+1} I_m + D_r I_{m+1} \tilde{J}_m}{\tilde{Y}_{m+1} I_m + D_r I_{m+1} \tilde{Y}_m} \quad (\text{C.100})$$

$$\tan(\delta_m) \approx \frac{\frac{1}{m!} \left(\frac{\tilde{q}L}{2}\right)^m \frac{D_r}{at\tilde{q}} I_{m+1}}{-\frac{m!}{\pi} \left(\frac{2}{\tilde{q}L}\right)^{m+1} I_m - \frac{D_r}{at\tilde{q}} I_{m+1} \frac{(m-1)!}{\pi} \left(\frac{2}{\tilde{q}L}\right)^m} \quad (\text{C.101})$$

$$= -\frac{\frac{1}{m!} \left(\frac{\tilde{q}L}{2}\right)^{m-1} \frac{D_r}{at} I_{m+1} \frac{L}{2}}{\frac{m!}{\pi} \left(\frac{2}{\tilde{q}L}\right)^{m+1} \left(I_m + \frac{D_r}{at} I_{m+1} \frac{L}{2m}\right)} \quad (\text{C.102})$$

$$\tan(\delta_m) \approx -\frac{\pi m}{m!^2} \left(\frac{\tilde{q}L}{2}\right)^{2m} \quad (\text{C.103})$$

If  $m = 0$  the function  $Y_0$  diverges at small arguments, therefore another analysis should be performed

$$\tan(\delta_0) = \frac{\tilde{J}_1 I_0 + D_r I_1 \tilde{J}_0}{\tilde{Y}_1 I_0 + D_r I_1 \tilde{Y}_0} \quad (\text{C.104})$$

$$\approx \frac{\frac{\tilde{q}L}{2} I_0 + \frac{D_r}{at} I_1 \frac{L}{2} \frac{2}{\tilde{q}L}}{-\frac{1}{\pi} \left(\frac{2}{\tilde{q}L}\right) I_0 + \frac{D_r}{at} I_1 \frac{L}{2} \frac{2}{\tilde{q}L} \frac{2}{\pi} \left(\ln \frac{\tilde{q}L}{2} + \gamma\right)} \quad (\text{C.105})$$

$$\tan(\delta_0) \approx \frac{1}{\frac{2}{\pi} \left(\ln \frac{\tilde{q}L}{2} + \gamma\right)}, \quad (\text{C.106})$$

where  $\gamma = 0.5772$  is the Euler–Mascheroni constant.

### C.2.2 Schrödinger Formulation

At high energies, i. e., high momentum  $\tilde{k}$ , both  $\tilde{k}$  and  $k$  are real numbers, and the functions have real arguments, hence

$$e^{2i\delta_m} = \frac{\tilde{J}'_m - i\tilde{Y}'_m - B\tilde{J}_m + iB\tilde{Y}_m}{B\tilde{J}_m + iB\tilde{Y}_m - \tilde{J}'_m - i\tilde{Y}'_m} \quad (\text{C.107})$$

$$= \frac{\tilde{J}'_m - B\tilde{J}_m - i(\tilde{Y}'_m - B\tilde{Y}_m)}{-(\tilde{J}'_m - B\tilde{J}_m) - i(\tilde{Y}'_m - B\tilde{Y}_m)} \quad (\text{C.108})$$

$$= -1 \frac{(\tilde{J}'_m - B\tilde{J}_m)^2 - (\tilde{Y}'_m - B\tilde{Y}_m)^2 - 2i(\tilde{J}'_m - B\tilde{J}_m)(\tilde{Y}'_m - B\tilde{Y}_m)}{(\tilde{J}'_m - B\tilde{J}_m)^2 + (\tilde{Y}'_m - B\tilde{Y}_m)^2} \quad (\text{C.109})$$

$$\tan 2\delta_m = \frac{2(\tilde{J}'_m - B\tilde{J}_m)(\tilde{Y}'_m - B\tilde{Y}_m)}{(\tilde{J}'_m - B\tilde{J}_m)^2 - (\tilde{Y}'_m - B\tilde{Y}_m)^2} \quad (\text{C.110})$$

$$\tan \delta_m = \frac{\tilde{J}'_m - B\tilde{J}_m}{\tilde{Y}'_m - B\tilde{Y}_m} \quad (\text{C.111})$$

$$\tan \delta_m = \frac{\tilde{J}'_m - \frac{k}{\tilde{k}} \frac{J'_m(kL)}{J_m(kL)} \tilde{J}_m}{\tilde{Y}'_m - \frac{k}{\tilde{k}} \frac{J'_m(kL)}{J_m(kL)} \tilde{Y}_m} \quad (\text{C.112})$$

The  $\lim_{\tilde{k} \rightarrow \infty} \frac{k}{\tilde{k}} = 1$ , and

$$\lim_{\tilde{k} \rightarrow \infty} \frac{J'_m(kL)}{J_m(kL)} = \lim_{\tilde{k} \rightarrow \infty} \frac{J_{m-1}(kL) - J_{m+1}(kL)}{2J_m(kL)} \quad (\text{C.113})$$

$$\lim_{\tilde{k} \rightarrow \infty} \frac{J'_m(kL)}{J_m(kL)} = \frac{\sqrt{\frac{2}{\pi kL}} \cos(kL - \frac{\pi}{2}(m + \frac{1}{2}) + \frac{\pi}{2}) - \sqrt{\frac{2}{\pi kL}} \cos(kL - \frac{\pi}{2}(m + \frac{1}{2}) - \frac{\pi}{2})}{2\sqrt{\frac{2}{\pi kL}} \cos(kL - \frac{\pi}{2}(m + \frac{1}{2}))} \quad (\text{C.114})$$

$$= -\frac{\sin(kL - \frac{\pi}{2}(m + \frac{1}{2})) + \sin(kL - \frac{\pi}{2}(m + \frac{1}{2}))}{2 \cos(kL - \frac{\pi}{2}(m + \frac{1}{2}))} \quad (\text{C.115})$$

$$= -\frac{\sin(kL - \frac{\pi}{2}(m + \frac{1}{2}))}{\cos(kL - \frac{\pi}{2}(m + \frac{1}{2}))} \quad (\text{C.116})$$

$$= -\tan\left(kL - \frac{\pi}{2}\left(m + \frac{1}{2}\right)\right) \quad (\text{C.117})$$

$$\therefore \frac{k J'_m(kL)}{\tilde{k} J_m(kL)} \approx -\frac{\sin(kL - \frac{\pi}{2}(m + \frac{1}{2}))}{\cos(kL - \frac{\pi}{2}(m + \frac{1}{2}))} \quad (\text{C.118})$$

and

$$B\tilde{J}_m = -\frac{\sin(kL - \frac{\pi}{2}(m + \frac{1}{2}))}{\cos(kL - \frac{\pi}{2}(m + \frac{1}{2}))} \sqrt{\frac{2}{\pi\tilde{k}L}} \cos\left(\tilde{k}L - \frac{\pi}{2}\left(m + \frac{1}{2}\right)\right). \quad (\text{C.119})$$

With this, the complete expression in the numerator is

$$\begin{aligned} \tilde{J}'_m - B\tilde{J}_m &\approx \sqrt{\frac{2}{\pi\tilde{k}L}} \frac{1}{2} \left( \cos\left(\tilde{k}L - \frac{\pi}{2}\left(m + \frac{1}{2}\right) + \frac{\pi}{2}\right) - \cos\left(\tilde{k}L - \frac{\pi}{2}\left(m + \frac{1}{2}\right) - \frac{\pi}{2}\right) + \right. \\ &\quad \left. \tan\left(kL - \frac{\pi}{2}\left(m + \frac{1}{2}\right)\right) \cos\left(\tilde{k}L - \frac{\pi}{2}\left(m + \frac{1}{2}\right)\right) \right) \quad (\text{C.120}) \end{aligned}$$

$$\begin{aligned} &= \sqrt{\frac{2}{\pi\tilde{k}}} \left( -\sin\left(\tilde{k}L - \frac{\pi}{2}\left(m + \frac{1}{2}\right)\right) + \right. \\ &\quad \left. \tan\left(kL - \frac{\pi}{2}\left(m + \frac{1}{2}\right)\right) \cos\left(\tilde{k}L - \frac{\pi}{2}\left(m + \frac{1}{2}\right)\right) \right), \quad (\text{C.121}) \end{aligned}$$

using the asymptotic behavior for  $B$  and  $\tilde{Y}_m$ , we have

$$B\tilde{Y}_m = -\frac{\sin(kL - \frac{\pi}{2}(m + \frac{1}{2}))}{\cos(kL - \frac{\pi}{2}(m + \frac{1}{2}))} \sqrt{\frac{2}{\pi\tilde{k}L}} \sin\left(\tilde{k}L - \frac{\pi}{2}\left(m + \frac{1}{2}\right)\right) \quad (\text{C.122})$$

and the complete expression for the denominator can be rewrite as

$$\begin{aligned} \tilde{Y}'_m - B\tilde{Y}_m &\approx \sqrt{\frac{2}{\pi\tilde{k}L}} \frac{1}{2} \left( \sin\left(\tilde{k}L - \frac{\pi}{2}\left(m + \frac{1}{2}\right) + \frac{\pi}{2}\right) - \sin\left(\tilde{k}L - \frac{\pi}{2}\left(m + \frac{1}{2}\right) - \frac{\pi}{2}\right) + \right. \\ &\quad \left. \tan\left(kL - \frac{\pi}{2}\left(m + \frac{1}{2}\right)\right) \sin\left(\tilde{k}L - \frac{\pi}{2}\left(m + \frac{1}{2}\right)\right) \right) \quad (\text{C.123}) \end{aligned}$$

$$= \sqrt{\frac{2}{\pi\tilde{k}L}} \left( \cos\left(\tilde{k}L - \frac{\pi}{2}\left(m + \frac{1}{2}\right)\right) + \right.$$



$$\tan\left(kL - \frac{\pi}{2}\left(m + \frac{1}{2}\right)\right) \sin\left(\tilde{k}L - \frac{\pi}{2}\left(m + \frac{1}{2}\right)\right). \quad (\text{C.124})$$

Using both expressions into (4.79) we can write explicitly the carrier phase shift at high energy scattering

$$\tan \delta_m = \frac{-\sin\left(\tilde{k}L - \frac{\pi}{2}\left(m + \frac{1}{2}\right)\right) + \tan\left(kL - \frac{\pi}{2}\left(m + \frac{1}{2}\right)\right) \cos\left(\tilde{k}L - \frac{\pi}{2}\left(m + \frac{1}{2}\right)\right)}{\cos\left(\tilde{k}L - \frac{\pi}{2}\left(m + \frac{1}{2}\right)\right) + \tan\left(kL - \frac{\pi}{2}\left(m + \frac{1}{2}\right)\right) \sin\left(\tilde{k}L - \frac{\pi}{2}\left(m + \frac{1}{2}\right)\right)} \quad (\text{C.125})$$

and letting  $\beta = \frac{\pi}{2}\left(m + \frac{1}{2}\right)$

$$\tan \delta_m = \frac{-\sin(\tilde{k}L - \beta) + \frac{\sin(kL - \beta)}{\cos(kL - \beta)} \cos(\tilde{k}L - \beta)}{\cos(\tilde{k}L - \beta) \frac{\sin(kL - \beta)}{\cos(kL - \beta)} \sin(\tilde{k}L - \beta)} \quad (\text{C.126})$$

$$\tan \delta_m = \frac{-\sin(\tilde{k}L - \beta) \cos(kL - \beta) + \sin(kL - \beta) \cos(\tilde{k}L - \beta)}{\cos(\tilde{k}L - \beta) \cos(kL - \beta) + \sin(\tilde{k}L - \beta) \sin(kL - \beta)} \quad (\text{C.127})$$

$$= \frac{\sin(k - \tilde{k})L}{\cos(k - \tilde{k})L} \quad (\text{C.128})$$

$$\tan(\delta_m) \approx -(\tilde{k} - k)L \quad (\text{C.129})$$

$$= -\left(\tilde{k} - \sqrt{\tilde{k}^2 - \frac{2m^*}{\hbar^2}V}\right)L \quad (\text{C.130})$$

$$\approx -\left(\tilde{k} - \tilde{k}\left(1 - \frac{2m^*}{\hbar^2} \frac{V}{2\tilde{k}^2}\right)\right)L \quad (\text{C.131})$$

$$\lim_{\tilde{k} \rightarrow \infty} \tan(\delta_m) = -\frac{2m^*}{\hbar^2} \frac{VL}{2\tilde{k}L} \quad (\text{C.132})$$

At low energies regime, when  $E < V$ , the wave vector inside the barrier is an imaginary number,  $k = \sqrt{\frac{(E-V)2m_e}{\hbar^2}} = \imath\sqrt{\frac{(V-E)2m_e}{\hbar^2}} = \imath k_r$ ,

$$B = \frac{\imath k_r L}{\tilde{k}} \frac{J'_m(\imath k_r L)}{J_m(\imath k_r L)} \quad (\text{C.133})$$

$$= \frac{\imath k_r L}{\tilde{k}} \frac{\imath^{m-1} I'_m(k_r L)}{\imath^m I_m(k_r L)} \quad (\text{C.134})$$

$$= \frac{k_r}{\tilde{k}} \frac{I'_m(k_r L)}{I_m(k_r L)} \quad (\text{C.135})$$

then,  $B \in \text{Reals}$  even at  $E < V$  regime and the phase shift has the same form of equation (4.79), given by

$$\tan(\delta_m) = \frac{B\tilde{J}_m - \tilde{J}'_m}{B\tilde{Y}_m - \tilde{Y}'_m} \quad (\text{C.136})$$

with, for short wave vectors we have

$$\begin{aligned} \lim_{\tilde{k} \rightarrow 0} B &= \frac{k_r I_{m-1}(k_r L) + I_{m+1}(k_r L)}{2\tilde{k} I_m(k_r L)} \\ &\rightarrow \frac{k_r \sqrt{2/\pi k_r L} 2e^{k_r L}}{2\tilde{k} \sqrt{2/\pi k_r L} e^{k_r L}} \\ &= \frac{k_r}{2\tilde{k}} \\ &= \frac{\sqrt{V - \tilde{k}^2}}{2\tilde{k}} \\ &\approx \frac{1}{\tilde{k}} \sqrt{V} \left(1 - \frac{\tilde{k}^2}{2V}\right) \\ &= \frac{\sqrt{V}}{\tilde{k}} - \frac{\tilde{k}}{2\sqrt{V}} \end{aligned} \quad (\text{C.137})$$

On the numerator,  $B\tilde{J}_m$  and  $\tilde{J}'_m$  takes the form

$$\begin{aligned} B\tilde{J}_m &\rightarrow \left(\frac{\sqrt{V}}{\tilde{k}} - \frac{\tilde{k}}{2V}\right) \frac{1}{m!} \left(\frac{\tilde{k}L}{2}\right)^m \\ &= \frac{L\sqrt{V}}{2m!} \left(\frac{\tilde{k}L}{2}\right)^{m-1} - \frac{1}{L\sqrt{V}} \frac{1}{m!} \left(\frac{\tilde{k}L}{2}\right)^{m+1} \end{aligned} \quad (\text{C.138})$$

and

$$\begin{aligned} \tilde{J}'_m &= \frac{1}{2} (\tilde{J}_{m-1} - \tilde{J}_{m+1}) \\ &\rightarrow \frac{1}{2} \left( \frac{1}{(m-1)!} \left(\frac{\tilde{k}L}{2}\right)^{m-1} - \frac{1}{(m+1)!} \left(\frac{\tilde{k}L}{2}\right)^{m+1} \right) \\ &\approx \frac{1}{2} \frac{1}{(m-1)!} \left(\frac{\tilde{k}L}{2}\right)^{m-1}. \end{aligned} \quad (\text{C.139})$$

Putting it together, we have

$$B\tilde{J}_m - \tilde{J}'_m \approx \frac{L\sqrt{V}}{2m!} \left(\frac{\tilde{k}L}{2}\right)^{m-1} - \frac{1}{L\sqrt{V}} \frac{1}{m!} \left(\frac{\tilde{k}L}{2}\right)^{m+1} - \frac{1}{2} \frac{1}{(m-1)!} \left(\frac{\tilde{k}L}{2}\right)^{m-1} \quad (\text{C.140})$$

$$= \left(\frac{\tilde{k}L}{2}\right)^{m-1} \left(\frac{L\sqrt{V}}{2m!} - \frac{m}{2m!}\right) - \left(\frac{\tilde{k}L}{2}\right)^{m+1} \frac{1}{m!L\sqrt{V}}. \quad (\text{C.141})$$

On the other hand,

$$\begin{aligned} B\tilde{Y}_m &\rightarrow \left(\frac{\sqrt{V}}{\tilde{k}} - \frac{\tilde{k}}{2V}\right) \frac{-(m-1)!}{\pi} \left(\frac{2}{\tilde{k}L}\right)^{m+1} \\ &\approx -\frac{(m-1)!}{\pi} \frac{\sqrt{V}}{2} L \left(\frac{2}{\tilde{k}L}\right)^{m+1} - \frac{(m-1)!}{\pi} \frac{1}{L\sqrt{V}} \left(\frac{2}{\tilde{k}L}\right)^{m-1} \end{aligned} \quad (\text{C.142})$$

$$\begin{aligned} \tilde{Y}'_m &= \frac{1}{2}(\tilde{Y}_{m-1} - \tilde{Y}_m + 1) \\ &\rightarrow \frac{1}{2} \left( \frac{-(m-2)!}{\pi} \left(\frac{2}{\tilde{k}L}\right)^{m-1} - \frac{-m!}{\pi} \left(\frac{2}{\tilde{k}L}\right)^{m+1} \right) \\ &\approx \frac{1}{2} \frac{m!}{\pi} \left(\frac{2}{\tilde{k}L}\right)^{m+1}. \end{aligned} \quad (\text{C.143})$$

Therefore

$$B\tilde{Y}_m - \tilde{Y}'_m \approx \left(\frac{2}{\tilde{k}L}\right)^{m+1} \frac{1}{\pi} \left( \frac{-(m-1)!L\sqrt{V}}{2} - \frac{m!}{2} \right) + \left(\frac{2}{\tilde{k}L}\right)^{m-1} \frac{(m-1)!}{\pi} \frac{1}{L\sqrt{V}}, \quad (\text{C.144})$$

then,

$$\tan \delta_m \rightarrow \frac{\left(\frac{\tilde{k}L}{2}\right)^{m-1} \frac{1}{2m!} (L\sqrt{V} - m) - \left(\frac{\tilde{k}L}{2}\right)^{m+1} \frac{1}{m!L\sqrt{V}}}{\left(\frac{2}{\tilde{k}L}\right)^{m+1} \frac{-(m-1)!}{2\pi} (L\sqrt{V} - m) + \left(\frac{2}{\tilde{k}L}\right)^{m-1} \frac{(m-1)!}{\pi L\sqrt{V}}} \quad (\text{C.145})$$

$$= \frac{\left(\frac{\tilde{k}L}{2}\right)^{m-1} \frac{1}{2m!} \left( L\sqrt{V} - m - \left(\frac{\tilde{k}L}{2}\right)^2 \frac{2}{L\sqrt{V}} \right)}{\left(\frac{2}{\tilde{k}L}\right)^{m+1} \frac{-(m-1)!}{2\pi} \left( L\sqrt{V} - m - \left(\frac{\tilde{k}L}{2}\right)^2 \frac{2}{L\sqrt{V}} \right)} \quad (\text{C.146})$$

$$\lim_{\tilde{k} \rightarrow 0} \tan(\delta_m) = -\frac{\pi m}{m^2} \left(\frac{\tilde{k}L}{2}\right)^{2m}. \quad (\text{C.147})$$

If  $m = 0$ , the function  $Y_0$  diverges at small arguments, therefore another analysis should be performed, which gives

$$B\tilde{Y}_0 \rightarrow \left(\frac{\sqrt{V}}{\tilde{k}} - \frac{\tilde{k}}{2\sqrt{V}}\right) \frac{2}{\pi} \left( \ln \frac{\tilde{k}L}{2} + \gamma \right) \quad (\text{C.148})$$

$$\tilde{Y}'_0 = -\tilde{Y}'_1 \rightarrow \frac{2}{\pi \tilde{k}L} \quad (\text{C.149})$$

$$B\tilde{Y}_0 - \tilde{Y}'_0 = \left( \frac{\sqrt{V}}{\tilde{k}} - \frac{\tilde{k}}{2\sqrt{V}} \right) \frac{2}{\pi} \left( \ln \frac{\tilde{k}L}{2} + \gamma \right) - \frac{2}{\pi\tilde{k}L} \quad (\text{C.150})$$

$$\tan(\delta_0) = \frac{\frac{\sqrt{V}}{\tilde{k}} - \frac{\tilde{k}}{2\sqrt{V}} + \frac{\tilde{k}L}{2}}{\left( \frac{\sqrt{V}}{\tilde{k}} - \frac{\tilde{k}}{2\sqrt{V}} \right) \frac{2}{\pi} \left( \ln \frac{\tilde{k}L}{2} + \gamma \right) - \frac{2}{\pi\tilde{k}L}} \quad (\text{C.151})$$

$$= \frac{1}{\frac{2}{\pi} \left( \ln \frac{\tilde{k}L}{2} + \gamma \right) - \frac{1}{\tilde{k}L\sqrt{V}}} \quad (\text{C.152})$$

$$\lim_{\tilde{k} \rightarrow 0} \tan(\delta_0) = \frac{\pi}{2} \frac{1}{\ln \frac{\tilde{k}L}{2} + \gamma} \quad (\text{C.153})$$

For  $V < 0$

$$\tan(\delta_m) \approx -(\tilde{k} - k)L \quad (\text{C.154})$$

$$= - \left( \tilde{k} - \sqrt{\tilde{k}^2 - \frac{2m^*}{\hbar^2}V} \right) L \quad (\text{C.155})$$

$$= - \left( \tilde{k} - \sqrt{\tilde{k}^2 + \frac{2m^*}{\hbar^2}|V|} \right) L \quad (\text{C.156})$$

$$\approx - \left( \tilde{k} - \tilde{k} \left( 1 + \frac{2m^*}{\hbar^2} \frac{|V|}{2\tilde{k}^2} \right) \right) L \quad (\text{C.157})$$

$$\lim_{\tilde{k} \rightarrow \infty} \tan(\delta_m) = \frac{2m^*}{\hbar^2} \frac{|V|L}{2\tilde{k}L}. \quad (\text{C.158})$$

# Bibliography

- [1] Ralph S. Tarr. Physical Foundations of Solid-State Devices. *Journal of the American Geographical Society of New York*, 31(1):1, 1899.
- [2] Tsuneya Ando, Alan B. Fowler, and Frank Stern. Electronic properties of two-dimensional systems. *Reviews of Modern Physics*, 54(2):437–672, apr 1982.
- [3] G. Bastard, J.A. Brum, and R. Ferreira. Electronic States in Semiconductor Heterostructures. In *Solid State Physics*, volume 44, pages 229–415. Elsevier, 1991.
- [4] E. E. Mendez and K. von Klitzing, editors. *Physics and Applications of Quantum Wells and Superlattices*, volume 170 of *NATO ASI Series*. Springer US, Boston, MA, 1987.
- [5] Horst Weller. Quantized Semiconductor Particles: A novel state of matter for materials science. *Advanced Materials*, 5(2):88–95, feb 1993.
- [6] M. Razeghi. Optoelectronic devices based on III-V compound semiconductors which have made a major scientific and technological impact in the past 20 years. *IEEE Journal of Selected Topics in Quantum Electronics*, 6(6):1344–1354, nov 2000.
- [7] Markus C. Amann, Federico Capasso, Anders Larsson, and Markus Pessa. Focus on advanced semiconductor heterostructures for optoelectronics. *New Journal of Physics*, 11, 2009.
- [8] Mohamed Henini. Quantum dot nanostructures. *Materials Today*, 5(6):48–53, jun 2002.

- [9] Yasuhiko Arakawa. Fabrication of Quantum Wires and Dots and Nanostructure Characterization. In *Low Dimensional Structures Prepared by Epitaxial Growth or Regrowth on Patterned Substrates*, pages 197–205. Springer Netherlands, Dordrecht, 1995.
- [10] Richard Nötzel and Klaus H. Ploog. Direct synthesis of semiconductor quantum-wire and quantum-dot structures. *Advanced Materials*, 5(1):22–29, jan 1993.
- [11] P K Bhattacharya and N K Dutta. Quantum Well Optical Devices and Materials. *Annual Review of Materials Science*, 23(1):79–123, aug 1993.
- [12] Zh.I. Alferov and A.F. Ioffe. Quantum wells and superlattices come of age. *III-Vs Review*, 10(7):26–31, nov 1997.
- [13] A. H. Castro Neto, F. Guinea, N. M R Peres, K. S. Novoselov, and A. K. Geim. The electronic properties of graphene. *Reviews of Modern Physics*, 81(1):109–162, jan 2009.
- [14] Gerald D. Mahan. *Many-Particle Physics*. Springer US, Boston, MA, 2000.
- [15] V López, F Comas, C Trallero-Giner, T Ruf, and M Cardona. Resonant electron-phonon coupling: Magnetopolarons in InP. *Physical Review B*, 54(15):502–507, 1996.
- [16] Alexandre S. Alexandrov and Jozef T. Devreese. *Advances in Polaron Physics*, volume 159 of *Springer Series in Solid-State Sciences*. Springer Berlin Heidelberg, Berlin, Heidelberg, 2010.
- [17] Jozef T Devreese and F Peeters. *Polarons and Excitons in Polar Semiconductors and Ionic Crystals*. Springer US, Boston, MA, 1984.
- [18] Arpun R. Nagaraja, Nicola H. Perry, Thomas O. Mason, Yang Tang, Matthew Grayson, Tula R. Paudel, Stephan Lany, and Alex Zunger. Band or polaron: The hole conduction mechanism in the p-Type spinel Rh<sub>2</sub>ZnO<sub>4</sub>. *Journal of the American Ceramic Society*, 95(1):269–274, 2012.

- [19] Ting Cao, Gang Wang, Wenpeng Han, Huiqi Ye, Chuanrui Zhu, Junren Shi, Qian Niu, Pingheng Tan, Enge Wang, Baoli Liu, and Ji Feng. Valley-selective circular dichroism of monolayer molybdenum disulphide. *Nature Communications*, 3(May):887, 2012.
- [20] Hannu Pekka Komsa and Arkady V. Krasheninnikov. Electronic structures and optical properties of realistic transition metal dichalcogenide heterostructures from first principles. *Physical Review B - Condensed Matter and Materials Physics*, 88(8):1–7, 2013.
- [21] J.A. Wilson and A.D. Yoffe. The transition metal dichalcogenides discussion and interpretation of the observed optical, electrical and structural properties. *Advances in Physics*, 18(73):193–335, 1969.
- [22] A. Castellanos-Gomez, N. Agrat, and G. Rubio-Bollinger. Optical identification of atomically thin dichalcogenide crystals. *Applied Physics Letters*, 96(21), 2010.
- [23] Emanuela Margapoti, Philipp Strobel, Mahmoud M. Asmar, Max Seifert, Juan Li, Matthias Sachsenhauser, Özlem Ceylan, Carlos-Andres Palma, Johannes V. Barth, Jose A. Garrido, Anna Cattani-Scholz, Sergio E. Ulloa, and Jonathan J. Finley. Emergence of Photoswitchable States in a Graphene–Azobenzene–Au Platform. *Nano Letters*, 14(12):6823–6827, dec 2014.
- [24] Chihiro Hamaguchi. *Basic Semiconductor Physics*, volume 18. Springer Berlin Heidelberg, Berlin, Heidelberg, 2010.
- [25] M.E. Mora-Ramos and D.A. Contreras-Solorio. The polaron in a GaAs/AlAs quantum well. *Physica B: Condensed Matter*, 253(3-4):325–334, oct 1998.
- [26] Guo-qiang Hai, F. M. Peeters, and J. T. Devreese. Polaron energy and effective mass in a quantum well. *Physical Review B*, 42(17):11063–11072, dec 1990.
- [27] Tianquan Lu and Yisong Zheng. Polaron properties in quantum wells. *Physical Review B*, 53(3):1438–1445, jan 1996.

- [28] Jun-jie Shi, Xiu-qin Zhu, Zi-xin Liu, Shao-hua Pan, and Xing-yi Li. Polaron effects in asymmetric semiconductor quantum-well structures. *Physical Review B*, 55(7):4670–4679, feb 1997.
- [29] A. Yu. Maslov and O. V. Proshina. Polaron mass of charge carriers in semiconductor quantum wells. *Semiconductors*, 49(10):1344–1347, oct 2015.
- [30] A. Cantarero, C. Trallero-Giner, and M. Cardona. Excitons in one-phonon resonant Raman scattering: Deformation-potential interaction. *Physical Review B*, 39(12):8388–8397, apr 1989.
- [31] K Greipel and U Rossler. Hole-acoustic phonon interaction in quantum wells. *Semiconductor Science and Technology*, 7(4):487–492, apr 1992.
- [32] Michael A. Stroschio and Mitra Dutta. *Phonons in Nanostructures*. Cambridge University Press, Cambridge, 2001.
- [33] James Patterson and Bernard Bailey. *Solid-State Physics*. Springer Berlin Heidelberg, Berlin, Heidelberg, 2010.
- [34] J. M. Luttinger and W. Kohn. Motion of Electrons and Holes in Perturbed Periodic Fields. *Physical Review*, 97(4):869–883, feb 1955.
- [35] A Saidane. The Physics of Low-dimensional Semiconductors: An Introduction. *Microelectronics Journal*, 31(4):292, apr 2000.
- [36] Mark Fox. Quantum Processes in Semiconductors (Fifth Edition), by Brian K. Ridley. *Contemporary Physics*, 55(4):338–339, oct 2014.
- [37] D.J.Griffiths. *Griffiths - Introduction to Quantum Mechanics*. Pearson Education Inc, United States of America, second edition, 1995.
- [38] Roland Winkler. *Spin–Orbit Coupling Effects in Two-Dimensional Electron and Hole Systems*, volume 191 of *Springer Tracts in Modern Physics*. Springer Berlin Heidelberg, Berlin, Heidelberg, 2003.
- [39] Xia Jian-Bai. Effective-mass theory for superlattices grown on (11)N-oriented substrates. *Physical Review B*, 43(12), 1991.



- [40] W. Kohn and J. M. Luttinger. Quantum Theory of Cyclotron Resonance in Semiconductors. *Physical Review*, 96(2):529–530, oct 1954.
- [41] J. M. Luttinger. Quantum Theory of Cyclotron Resonance in Semiconductors: General Theory. *Physical Review*, 102(4):1030–1041, may 1956.
- [42] Paul Harrison and Alex Valavanis. *Quantum Wells, Wires and Dots*. John Wiley & Sons, Ltd, Chichester, UK, may 2016.
- [43] I. Vurgaftman, J. R. Meyer, and L. R. Ram-Mohan. Band parameters for III-V compound semiconductors and their alloys. *Journal of Applied Physics*, 89(11 I):5815–5875, 2001.
- [44] N. Galbiati, E. Grilli, M. Guzzi, M. Henini, and L. Pavesi. Is the be incorporation the same in (311)A and (100) AlGaAs? *Microelectronics Journal*, 28(8-10):993–998, oct 1997.
- [45] Riaz H Mari, Muhammad Shafi, Mohsin Aziz, Almontaser Khatab, David Taylor, and Mohamed Henini. Electrical characterisation of deep level defects in Be-doped AlGaAs grown on (100) and (311)A GaAs substrates by MBE. *Nanoscale Research Letters*, 6(1):180, 2011.
- [46] D. F. Cesar, M. D. Teodoro, H. Tsuzuki, V. Lopez-Richard, G. E. Marques, J. P. Rino, S. A. Lourenço, E. Marega, I. F L Dias, J. L. Duarte, P. P. González-Borrero, and G. J. Salamo. Contrasting LH-HH subband splitting of strained quantum wells grown along [001] and [113] directions. *Physical Review B*, 81(23):233301, jun 2010.
- [47] J. A. Porto and J. Sánchez-Dehesa. Theoretical study of strained thin quantum wells grown on vicinal surfaces. *Physical Review B*, 51(20):14352–14360, may 1995.
- [48] L. D. Landau. Über die Bewegung der Elektronen in Kristallgitter. *Physik Z. Sowjetunion*, 3:644–645, 1933.
- [49] Solomon Isaakovic Pekar. *Issledovanija po elektronnoj teorii kristalov*. Akademie-Verlag, 1954.

- [50] J. Bonca, S. A. Trugman, and I. Batistic. Holstein Polaron. *Physical Review B*, 60(3):1633, 1998.
- [51] V. Preisler, R. Ferreira, S. Hameau, L. A. De Vaultier, Y. Guldner, M. L. Sadowski, and A. Lemaitre. Hole-LO phonon interaction in InAs/GaAs quantum dots. *Physical Review B - Condensed Matter and Materials Physics*, 72(11):1–6, 2005.
- [52] P. Pfeffer and W. Zawadzki. Conduction electrons in GaAs: Five-level kp theory and polaron effects. *Physical Review B*, 41(3):1561–1576, jan 1990.
- [53] F. M. Peeters and J. T. Devreese. Energy levels of two- and three-dimensional polarons in a magnetic field. *Physical Review B*, 31(6):3689–3695, 1985.
- [54] Conyers Herring and Erich Vogt. Transport and deformation-potential theory for many-valley semiconductors with anisotropic scattering. *Physical Review*, 101(3):944–961, 1956.
- [55] F Grusdt. All-coupling theory for the Fröhlich polaron. *Physical Review B*, 93(14):144302, apr 2016.
- [56] F. M. Peeters and J. T. Devreese. Energy levels of two- and three-dimensional polarons in a magnetic field. *Physical Review B*, 31(6):3689–3695, mar 1985.
- [57] I. S. Gradshteyn, I. M. Ryzhik, and Robert H. Romer. Tables of Integrals, Series, and Products. *American Journal of Physics*, 56(10):958–958, oct 1988.
- [58] V.G. Talalaev, B.V. Novikov, S.Yu. Verbin, A.B. Novikov, Dinh Son Thath, I.V. Shchur, G. Gobsch, R. Goldhahn, N. Stein, A. Golombek, G.E. Tsyrlin, V.N. Petrov, V.M. Ustinov, A.E. Zhukov, and A.Yu. Egorov. Recombination emission from InAs quantum dots grown on vicinal GaAs surfaces. *Semiconductors*, 34(4):453, 2000.
- [59] D.R. Matthews, H.D. Summers, P.M. Snowton, Peter Blood, Paul Rees, and Mark Hopkinson. Dynamics of the wetting-Layer-quantum-dot interaction in In-GaAs self-assembled systems. *IEEE Journal of Quantum Electronics*, 41(3):344–350, mar 2005.

- [60] A. Babiński, J Borysiuk, S Kret, M. Czyż, A Golnik, S Raymond, and Z R Wasilewski. Natural quantum dots in the InAs/GaAs wetting layer. *Applied Physics Letters*, 92(17):171104, apr 2008.
- [61] O. B. Shchekin and D. G. Deppe. The role of p-type doping and the density of states on the modulation response of quantum dot lasers. *Applied Physics Letters*, 80(15):2758–2760, 2002.
- [62] Troels Markussen, Philip Kristensen, Bjarne Tromborg, Tommy Winther Berg, and Jesper Mørk. Influence of wetting-layer wave functions on phonon-mediated carrier capture into self-assembled quantum dots. *Physical Review B - Condensed Matter and Materials Physics*, 74(19):1–6, 2006.
- [63] Fei Ding, Y. H. Chen, C. G. Tang, Bo Xu, and Z. G. Wang. Carrier channels of multimodal-sized quantum dots: A surface-mediated adatom migration picture. *Physical Review B - Condensed Matter and Materials Physics*, 76(12):1–7, 2007.
- [64] S. Fafard, D. Leonard, J. L. Merz, and P. M. Petroff. Selective excitation of the photoluminescence and the energy levels of ultrasmall InGaAs/GaAs quantum dots. *Applied Physics Letters*, 65(11):1388–1390, 1994.
- [65] E. C. Le Ru, J. Fack, and R. Murray. Temperature and excitation density dependence of the photoluminescence from annealed InAs/GaAs quantum dots. *Physical Review B*, 67(24):245318, 2003.
- [66] R. Leon, S. Fafard, P. G. Piva, S. Ruvimov, and Z. Liliental-Weber. Tunable intersublevel transitions in self-forming semiconductor quantum dots. *Physical Review B*, 58(8):R4262–R4265, 1998.
- [67] Gustavo A. Narvaez, Gabriel Bester, and Alex Zunger. Carrier relaxation mechanisms in self-assembled (In, Ga)As/GaAs quantum dots: Efficient P S Auger relaxation of electrons. *Physical Review B*, 74(7):075403, aug 2006.
- [68] R. I. Dzhioev, K. V. Kavokin, V. L. Korenev, M. V. Lazarev, B. Ya. Meltser, M. N. Stepanova, B. P. Zakharchenya, D. Gammon, and D. S. Katzer. Low-temperature spin relaxation in *n*-type GaAs. *Physical Review B*, 66(24):245204, 2002.

- [69] Igor Zutic, Jaroslav Fabian, and S. Das Sarma. Spintronics: Fundamentals and applications. *Reviews of Modern Physics*, 76(2):323–410, 2004.
- [70] S. Slovic and K. D. Moore. Editors' Note. *Interdisciplinary Studies in Literature and Environment*, 21(1):1–4, jun 2014.
- [71] Stefan Seidl, Martin Kroner, Brian D Gerardot, Daniel Brunner, Paul a Dalgarno, O Patrik, Khaled Karrai, Nick G Stoltz, Pierre M Petroff, Richard J Warburton, Patrik Ohberg, Stefan Seidl, Martin Kroner, Khaled Karrai, Nick G Stoltz, Pierre M Petroff, and Richard J Warburton. Optical pumping of a single hole spin in a quantum dot. *Nature*, 451(7177):441–444, 2008.
- [72] H. Hoffmann, G. V. Astakhov, T. Kiessling, W. Ossau, G. Karczewski, T. Wojtowicz, J. Kossut, and L. W. Molenkamp. Optical spin pumping of modulation-doped electrons probed by a two-color Kerr rotation technique. *Physical Review B - Condensed Matter and Materials Physics*, 74(7):2–5, 2006.
- [73] H. B. Chan, R. C. Ashoori, L. N. Pfeiffer, and K. W. West. Tunneling into Ferromagnetic Quantum Hall States: Observation of a Spin Bottleneck. *Physical Review Letters*, 83(16):3258–3261, 1999.
- [74] S. M. Huang, Y. Tokura, H. Akimoto, K. Kono, J. J. Lin, S. Tarucha, and K. Ono. Spin bottleneck in resonant tunneling through double quantum dots with different zeeman splittings. *Physical Review Letters*, 104(13):1–4, 2010.
- [75] G E Marques, V Lo, and J Drake. Magneto resonant Raman scattering in zinc-blende-type semiconductors: Electron-phonon interaction mediated by a deformation potential. *Physical Review B*, 56(24):691–700, 1997.
- [76] V. López-Richard, G. Marques, C. Trallero-Giner, and J Drake. Resonant Raman scattering in a magnetic field assisted by Fröhlich interaction in zinc-blende-type semiconductors. *Physical Review B*, 58(24):16136–16143, 1998.
- [77] V. López-Richard, G. E. Marques, and C. Trallero-Giner. Dielectric response in narrow-gap semiconductor quantum wells in a magnetic field. *Journal of Applied Physics*, 89(11):6400–6407, 2001.

- [78] B. Radisavljevic, A. Radenovic, J. Brivio, V. Giacometti, and A. Kis. Single-layer MoS<sub>2</sub> transistors. *Nature Nanotechnology*, 6(3):147–150, mar 2011.
- [79] Hui Fang, Steven Chuang, Ting Chia Chang, Kuniharu Takei, Toshitake Takahashi, and Ali Javey. High-Performance Single Layered WSe<sub>2</sub> p-FETs with Chemically Doped Contacts. *Nano Letters*, 12(7):3788–3792, jul 2012.
- [80] Kai Leng, Zhongxin Chen, Xiaoxu Zhao, Wei Tang, Bingbing Tian, Chang Tai Nai, Wu Zhou, and Kian Ping Loh. Phase Restructuring in Transition Metal Dichalcogenides for Highly Stable Energy Storage. *ACS Nano*, 10(10):9208–9215, oct 2016.
- [81] Andreas Pospischil, Marco M. Furchi, and Thomas Mueller. Solar-energy conversion and light emission in an atomic monolayer p–n diode. *Nature Nanotechnology*, 9(4):257–261, apr 2014.
- [82] R. S. Sundaram, M. Engel, A. Lombardo, R. Krupke, A. C. Ferrari, Ph. Avouris, and M. Steiner. Electroluminescence in Single Layer MoS<sub>2</sub>. *Nano Letters*, 13(4):1416–1421, apr 2013.
- [83] L M Xie. Two-dimensional transition metal dichalcogenide alloys: preparation, characterization and applications. *Nanoscale*, 7(44):18392–18401, 2015.
- [84] Emanuela Margapoti, Juan Li, Özlem Ceylan, Max Seifert, Filippo Nisic, Tuan Le Anh, Felix Meggendorfer, Claudia Dragonetti, Carlos-andres Palma, Johannes V Barth, and Jonathan J Finley. A 2D Semiconductor-Self-Assembled Monolayer Photoswitchable Diode. *Advanced Materials*, 27(8):1426–1431, feb 2015.
- [85] Chul-Ho Lee, Gwan-hyoung Lee, Arend M. van der Zande, Wenchao Chen, Yilei Li, Minyong Han, Xu Cui, Ghidewon Arefe, Colin Nuckolls, Tony F Heinz, Jing Guo, James Hone, and Philip Kim. Atomically thin pn junctions with van der Waals heterointerfaces. *Nature Nanotechnology*, 9(9):676–681, aug 2014.
- [86] D Sercombe, S Schwarz, O. Del Pozo-Zamudio, F Liu, B J Robinson, E a Chekhovich, I. I Tartakovskii, O Kolosov, and a I Tartakovskii. Optical investi-

- gation of the natural electron doping in thin MoS<sub>2</sub> films deposited on dielectric substrates. *Scientific Reports*, 3(1):3489, dec 2013.
- [87] Alexander V. Kolobov and Junji Tominaga. *Two-Dimensional Transition-Metal Dichalcogenides*, volume 239 of *Springer Series in Materials Science*. Springer International Publishing, Cham, 2016.
- [88] A.K.M. Newaz, D Prasai, J.I. Ziegler, D Caudel, S Robinson, R.F. Haglund Jr., and K.I. Bolotin. Electrical control of optical properties of monolayer MoS<sub>2</sub>. *Solid State Communications*, 155:49–52, feb 2013.
- [89] Di Xiao, Gui-bin Liu, Wanxiang Feng, Xiaodong Xu, and Wang Yao. Coupled Spin and Valley Physics in Monolayers of MoS<sub>2</sub> and Other Group-VI Dichalcogenides. *Physical Review Letters*, 108(19):196802, may 2012.
- [90] Intek Song, Chibeom Park, and Hee Cheul Choi. Synthesis and properties of molybdenum disulphide: from bulk to atomic layers. *RSC Adv.*, 5(10):7495–7514, 2015.
- [91] Michele Buscema, Gary A. Steele, Herre S J van der Zant, and Andres Castellanos-Gomez. The effect of the substrate on the Raman and photoluminescence emission of single-layer MoS<sub>2</sub>. *Nano Research*, 7(4):1–11, 2014.
- [92] Ji Feng, Xiaofeng Qian, Cheng-Wei Huang, and Ju Li. Strain-engineered artificial atom as a broad-spectrum solar energy funnel. *Nature Photonics*, 6(12):866–872, 2012.
- [93] Juan Li, Jakob Wierzbowski, Özlem Ceylan, Julian Klein, Filippo Nisic, Tuan Le Anh, Felix Meggendorfer, Carlos-Andres Palma, Claudia Dragonetti, Johannes V. Barth, Jonathan J. Finley, and Emanuela Margapoti. Tuning the optical emission of MoS<sub>2</sub> nanosheets using proximal photoswitchable azobenzene molecules. *Applied Physics Letters*, 105(24):241116, dec 2014.
- [94] H. Peelaers and C. G. Van de Walle. Effects of strain on band structure and effective masses in MoS<sub>2</sub>. *Physical Review B*, 86(24):241401, dec 2012.

- [95] W. Macke. L. D. Landau and E. M. Lifshitz, Quantum Mechanics, Non-Relativistic Theory. Volume 3 of a Course of Theoretical Physics. *ZAMM - Zeitschrift für Angewandte Mathematik und Mechanik*, 39(5-6):250–250, 1959.
- [96] Andor Kormányos, Viktor Zólyomi, Neil D. Drummond, Péter Rakyta, Guido Burkard, and Vladimir I. Fal'Ko. Monolayer MoS<sub>2</sub>: Trigonal warping, the  $\Gamma$  valley, and spin-orbit coupling effects. *Physical Review B - Condensed Matter and Materials Physics*, 88(4):1–8, 2013.
- [97] D S Novikov. Elastic scattering theory and transport in graphene. *Physical Review B*, 76(24):245435, dec 2007.
- [98] MO Goerbig, G Montambaux, and F Piéchon. Measure of Diracness in two-dimensional semiconductors. *arXiv preprint arXiv:1312.3879*, 105(March):1–6, 2013.
- [99] Mahmoud M. Asmar and Sergio E. Ulloa. Symmetry-breaking effects on spin and electronic transport in graphene. *Physical Review B*, 91(16):165407, apr 2015.
- [100] Charles Kittel. *Introduction to Solid State Physics*. Wile, 2004.
- [101] Di Xiao, Gui-Bin Liu, Wanxiang Feng, Xiaodong Xu, and Wang Yao. Coupled Spin and Valley Physics in Monolayers of MoS<sub>2</sub> and Other Group-VI Dichalcogenides. *Physical Review Letters*, 108(19):196802, may 2012.